UNIVERSITY OF SOUTHAMPTON

FACULTY OF PHYSICAL AND APPLIED SCIENCES

OPTOELECTRONICS RESEARCH CENTRE

NANOSTRUCTURED OPTICAL FIBRE TAPERS AND RELATED APPLICATIONS

by

Ming Ding

Thesis submitted for the degree of Doctor of Philosophy

June 2013

UNIVERSITY OF SOUTHAMPTON

ABSTRACT

FACULTY OF PHYSICAL AND APPLIED SCIENCES

Optoelectronics Research Centre

Doctor of Philosophy

NANOSTRUCTURED OPTICAL FIBRE TAPERS AND RELATED APPLICATIONS

by Ming Ding

In the last decade, optical fibre tapers have attracted considerable interest because they offer a variety of enabling properties, including large evanescent fields, flexibility, configurability, high confinement, robustness and compactness. These distinctive features have been exploited in a wealth of applications ranging from telecommunication devices to sensors, from optical manipulation to high-*Q* resonators. Nanostructures on the optical fibre tapers are very promising since the size of the device can be extremely small. With the development of nanostructuring methods, sub-wavelength feature sizes have been achieved. In this thesis, nanostructured optical fibre tapers and some related applications are discussed.

Light confinement is limited by diffraction and the minimum spot size is related to the light wavelength. In this thesis, light confinement in two and three dimensions is proposed and achieved with two typologies of nanostructured optical fibre tapers.

The first group of devices exploits plasmons excited at the optical fibre tips to obtain high transmissivity, and confine light to a sub-wavelength dimension. Optical fibre tips were designed according to numerical simulations and coated by a layer of gold; an extremely small aperture was then opened at the tip apex. The experimental characterization and simulation results showed their improved transmission efficiency (higher than 10^{-2}) and thermal expansion measurements showed no shape changes could be detected within the accuracy of the system (~2 nm) for 9 mW injected powers. Effective confinements to 10 nm or smaller can be envisaged by decreasing the aperture

size and slope angle. Application of this small spot size source can include scanning near-field optical microscope, optical recording, photolithography and bio-sensing.

The second group achieves three dimensional light confinement exploiting a Fabry-Perot microcavity formed by a microfibre grating similar to those used in distributed feedback lasers. Microfibres were patterned using a *Focused Ion Beam* (FIB) system. In this structure, the microcavity provides longitudinal light confinement, whereas air-dielectric guiding by the microfibre provides diffraction limited confinement in the other two dimensions. Due to the high refractive index contrast between silica and air, strong reflection can be obtained by only dozens of notches. This device can be used for a wide range of applications, e.g. sensing and triggered single-photon sources.

Light confinement in nanostructured optical fibre tapers was exploited in a micrometric thermometer. A compact thermometer based on a broadband microfibre coupler tip showed a dynamic range spanning from room temperature to 1511ºC with a response time of tens of microseconds. This is the highest temperature measured with a silica optical fibre device. An average sensitivity of 11.96 pm/ºC was achieved for a coupler tip with ~2.5 μm diameter. A resolution of 0.66ºC was achieved for a coupler tip diameter of ~12.6 μm. Better resolution can be achieved with smaller size microfibre coupler tips.

Optical fibre tapers are commonly used to couple light to selected resonator modes. Here FIB was used to inscribe microgrooves on optical *Bottleneck Microresonator* (BMR) surfaces to excite selected whispering gallery modes. By monitoring the transmission spectrum of the optical fibre taper, substantial spectral clean-up was obtained in appropriately scarred BMRs. Single high-*Q* mode operation can be achieved by either using two asymmetrical perpendicular scars or placing the grooves closer to the BMR centre, providing the potential for high performance sensors and other optical devices.

Finally, strong three dimensional localization has been achieved in *Plasmonic Slot Nano-Resonators* (PSNRs) embedded in a gold-coated optical fibre tapers. Different shapes PSNRs, embedded in thin gold metal film coated

plasmonic microfibre, were numerically investigated. The intensity enhancement (in excess of 10^6) and the resonance wavelength depend on both the PSNR and microfibre dimensions. Theoretically and experimentally, the transversal excitation of a rectangular PSNR embedded in a thin gold film coated plasmonic fibre tip was discussed for the first time, and showed high localization and strong enhancement (7.24×10^3). This device can find a wide range of applications such as surface-enhanced Raman scattering, optical filtering, spectroscopy and bio-sensing.

Table of Contents

List of Figures

List of Tables

Declaration of Authorship

I, Ming Ding

declare that the thesis entitled

Nanostructured Optical Fibre Tapers and Related Applications

and the work presented in the thesis are both my own, and have been generated by me as the result of my own original research. I confirm that:

- this work was done wholly or mainly while in candidature for a research degree at this University;
- where any part of this thesis has previously been submitted for a degree or any other qualification at this University or any other institution, this has been clearly stated;
- where I have consulted the published work of others, this is always clearly attributed;
- where I have quoted from the work of others, the source is always given. With the exception of such quotations, this thesis is entirely my own work;
- I have acknowledged all main sources of help;
- where the thesis is based on work done by myself jointly with others, I have made clear exactly what was done by others and what I have contributed myself;
- parts of this work have been published. (see *List of Publications*)

Signed: ……..

Date:……

Acknowledgements

This thesis would not have been possible without the kind assistance and support of the organizations and the people around me. I would like to acknowledge the Optoelectronic Research Centre (ORC) for providing financial support for my three and half years study in the UK.

I would like to express my sincere gratitude to my supervisor, Dr. Gilberto Brambilla, for his patient guidance and invaluable assistance throughout the course of this work. I am particularly thankful for his unwavering encouragement and timely comments throughout my studies. Big thanks to Prof. Michalis N. Zervas for all his help and advice on the whispering gallery mode selection and plasmonic slot nano-resonator work, Dr. Yongmin Yung for his help on experiment support when I firstly started my PhD, Dr. Pengfei Wang for the collaboration on microsphere and sensor work. I thank Dr. Ganapathy Senthil Murugan for his experiment support on mode selection in optical bottle resonator.

Many thanks to Mr. Timothy Lee for his help on numerical modelling. A very special thank to Mr. Jun-Yu (Bruce) Ou for his support on device nanofabrication. I acknowledge Dr. Peter Horak, Dr. Francesco Poletti, Dr. Harold M H Chong, Dr. Behrad Gholipour, Ms. Rand Ismaeel, Mr. George Chen. Mr. Ehab Saleh, Mr. Jianfa Zhang, Dr. Jindan Shi for all their assistance with the equipment and useful discussion throughout the studies.

I would like to thank Dr. Fei Xu in Nanjing University for providing me the optical fibre tips with very high quality, Prof. Franco Cacialli, Dr. Oliver Fenwick and Dr. Francesco Di Stasio from University College London for their support on the sub-wavelength light confinement source characterization, Prof. Frederique De Fornel, Dr. Benoit Cluzel and Mr. Dellinger Jean from the University of Bourgogne for their help on tips fabrication and testing.

I am most grateful to Mr. Neil Sessions, Mr. David Sager, Mr. Trevor Austin, Mr. Ed Weatherby, Mr. Mark Lessey, and Mr. Paul Allwood for their tireless technical support. I thank Mrs. Eveline Smith, Ms. Tanya Morrow, Mr. Kevin Sumner and Mr. David Oliver for all their assistance. I am grateful to my

housemates and my good friends for helping me get through the difficult times and for all the entertainment and care they have provided.

I would like to thank my family for their encouragement and support throughout my studies.

Principal Abbreviations

AD	Areal Density
AOMR	All-Optical Magnetic Recording
BD	Blu-ray Disc
BMR	Bottleneck Microresonator
BPM	Bit Patterned Media
CD	Compact Disc
CQED	Cavity Quantum Electrodynamics
DFB	Distributed Feedback
DVD	Digital Versatile Disc
FBG	Fibre Bragg Grating
FIB	Focused Ion Beam
fs	Femtosecond
FWHM	Full Width at Half Maximum
F-P	Fabry-Perot
HAMR	Heat-Assisted Magnetic Recording
HDD	Hard Disk Drive
HF	Hydrofluoric
IC	Integrated Circuit
LMR	Longitudinal Magnetic Recording
MFBG	Microfibre Bragg Grating
MFC	Microfibre Coupler
MFCT	Microfibre Coupler Tip
MPSBG	Microfibre Phase-Shifted Bragg Grating
OSA	Optical Spectrum Analyser
PCR	Phase Change Recording
PML	Perfect Matched Layer
PMR	Perpendicular Magnetic Recording

PNRs	Plasmonic Nano-Resonators
PSBGs	Phase-Shifted Bragg Gratings
PSNRs	Plasmonic Slot Nano-Resonators
ROM	Read Only Memory
SC	Supercontinuum
SEM	Scanning Electron Microscope
SERS	Surface-Enhanced Raman Scattering
SNOM	Scanning Near-field Optical Microscope
SPPs	Surface Plasmon Polaritons
SPR	Surface Plasmon Resonance
SPs	Surface Plasmons
WGMs	Whispering Gallery Modes
2D	Two Dimensional
3D	Three Dimensional

Symbols

a	Core radius if the core-cladding model is considered, the cladding radius if the cladding-air model is used
A	Surface area of the heated region
A_m	A normalization coefficient of wave function in bottleneck microresonator
Bi	Biot number
c	Heat capacity
C_x	Coupling coefficient of *x* polarization
$\overline{C_x}$	Averaged coupling coefficient of *x* polarization
C_y	Coupling coefficient of *y* polarization
$\overline{C_y}$	Averaged coupling coefficient of *y* polarization
d	Aperture diameter in nanostructured optical fibre tips
C_1, C_2	Constants related to the heat transfer density and wire diameter
d_R	Plasmonic slot nano-resonator waist width
D	Optical fibre taper diameter
D_b	Bottleneck microresonator diameter
D_R	Plasmonic slot nano-resonator width
D_s	Bottleneck microresonator stem diameter
E	Electric field
E_0	Electric field without the plasmonic slot nano-resonator
$\|E\|$	Total electric field modulus
E_f	Enhancement factor
E_x	*x* component of the electric field

E_y	y component of the electric field
E_z	z component of the electric field
ΔE_m	Energy levels difference
$\vec{E}(r,\varphi,z)$	Transverse electric field in bottleneck microresonator
h	Convective heat transfer coefficient
h_s	Surface convection coefficient
Δh_{tip}	Length variation of the nanostructured optical fibre tip
H_q	m^{th} order Hermite polynomial
I	Electric field intensity
I_0	Electric field intensity without the plasmonic slot nano-resonator
J_m	Bessel function of m^{th} order
J_ν	ν^{th} order Bessel function of the first kind
$\vec{k}$	Wave vector
$\vec{k}_0$	Wave vector in free space
k_b	Thermal conductivity of the body
k_s	Wave vector component along β_{sp}
$\vec{k}_i$	Wave vector of the incident light
$\vec{k}_r$	Wave vector of the reflected light
Δk	A constant defined by the bottleneck microresonator shape profile
$\vec{K}$	Grating wave vector
K_m	Modified Hankel function of m^{th} order
K_ν	ν^{th} order modified Bessel function of the second kind
L	Coupling length of microfibre coupler

L_b	Neck-to-neck distance of bottleneck microresonator
L_c	Characteristic length
L_R	Plasmonic slot nano-resonator length
$2m$	Number of field nodes around the circumference of bottleneck microresonator
n	Medium refractive index
n_1	Core refractive index
n_2	Cladding refractive index
n_3	Air refractive index
n_{eff}	Effective index of the mode
n_{Silica}	Silica refractive index
n_{Air}	Air refractive index
Δn	Refractive index contrast (modulation)
N	Grating harmonic order
p	Number of power maxima along the radius of bottleneck microresonator
q	Number of field nodes along the axis of the bottleneck microresonator
Q	Quality factor
R	Sensor responsivity (sensitivity)
R_b	Bottleneck microresonator radius
S	Sensor resolution
t	Coating thickness
T	Temperature
T_f	Surrounding fluid temperature
T_{PSBG}	Transfer matrix of the phase-shifted Bragg grating
T^1, T^2	Transfer matrix of grating region 1, 2

T^{ps}	Transfer matrix of the region inducing a phase shift
ν	First subscript of the mode HE_{vm} and EH_{vm}
V_h	Volume of the heated region
Δx	Minimum spatial detail
z_c	Axial spreading of bottleneck microresonator mode
α	Slope angle of the nanostructured optical fibre tip
α_{sp}	Surface plasmon resonance angle
α_p	p^{th} root of the Airy function
β	Propagation constant
β_1, β_2	Propagation constant of the modes
β_{sp}	Surface plasmon propagation constant
ε_{air}	Dielectric constants of air
ε_{gold}	Dielectric constants of gold
θ	Angular resolution
λ	Wavelength
λ_0	Wavelength in free space
λ_B	Bragg wavelength
λ_{mpq}	Resonant wavelength for each (m,p,q) mode
$\Delta\lambda$	Resonance width
Λ	Pitch of grating
ρ	Density
ρ^{PSBG}	Reflectivity of the phase-shifted Bragg grating
τ	Response time
τ^{PSBG}	Tranmissivity of the phase-shifted Bragg grating
Φ	Shifted-phase factor

$\Phi(r,z)$	Radial distribution of the field in bottleneck microresonators
$\Psi(z)$	Axial distribution of the field in bottleneck microresonators
Ω	Taper angle
$\overline{\Omega}$	Adiabatic angle

To my Parents with love

Chapter 1 Introduction

You were not born to live like brutes,
but to follow virtue and knowledge.

Dante Alighieri

1.1 Overview

In the past decade, optical fibre tapers with micron or sub-micron diameters have attracted much attention and found a wide range of applications because of their unique properties, including:

(1) Large evanescent fields: In optical fibre, beyond the interface within a step-profile fibre and beyond the turning point within a graded-profile fibre, the fields associated with local plane waves decreases exponentially with increasing distance from the axis and is called evanescent. This decrease is very rapid for virtually all rays, and varies exponentially with the inverse of the free-space wavelength of the light in the core [1]. A considerable fraction of the power can propagate in the evanescent field outside the fibre taper physical boundary [2], and this can be exploited for atom guides [3-6], particle manipulation [7-9], sensors [10-17], and high-*Q* resonators [18-26].

(2) Strong confinement: light can be confined to an area as small as 1 μm^2 in devices over 5 mm long, allowing the ready observation of nonlinear interactions, such as supercontinuum generation [27-31].

(3) Great configurability: optical fibre tapers can be easily manipulated and bent because of their relatively high mechanical strength. Bend radii of the order of a few micrometres can be easily achieved with low induced bend loss

[32], allowing for highly compact devices with complex geometries, e.g., *Two Dimensional* (2D) [19] and *Three Dimensional* (3D) [18] resonators.

(4) Low-loss connection: since optical fibre tapers are made by adiabatically stretching optical fibres, they preserve the original fibre size at their input and output, allowing ready splicing to standard fiberized components. Insertion losses smaller than 0.1 dB are commonly observed.

(5) Robustness: optical fibre tapers usually exhibit a negligible surface roughness, resulting in an extraordinarily high mechanical strength [33].

(6) Biocompatibility: since optical fibre tapers are generally fabricated from telecom optical fibres, their main constituent is silica, which is one of the best biocompatible inorganic material [34].

Optical fibre tapers have been manufactured using a wide range of techniques: electron beam lithography, laser ablation, template-based methods, bottom-up methods (such as vapour–liquid–solid techniques, chemical and physical vapour deposition), sol-gel methods, and top-down techniques (such as fibre pulling or direct draw from bulk materials) [35].

With the development of nanofabrication, fabricating nanoscale structures on optical fibre tapers opens new possibilities for bio-sensing, sub-wavelength confinement, optical trapping, and so on.

In this chapter, the theory of optical fibre tapers will be reviewed. Nanostructuring techniques will also be illustrated.

1.1.1 Optical fibre tapers

1.1.1.1 Light propagation in optical fibre tapers

Optical fibre tapers are pulled from optical fibres and comprise a taper waist and two conical shape transitions, which are linked to the untapered fibre. When this structure (Figure 1-1) has a sub-wavelength uniform waist region, it is often called an optical micro/nanofibre.

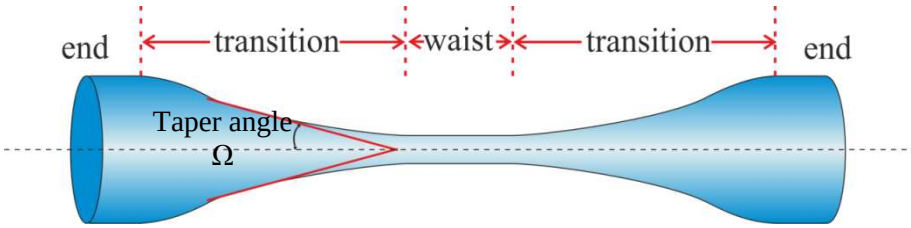

Figure 1-1 Schematic of an optical micro/nanofibre.

Some applications (like *Scanning Near-field Optical Microscopy* (SNOM) and optical memory), use optical fibre tips (Figure 1-2), which correspond to half of the taper shown in Figure 1-1.

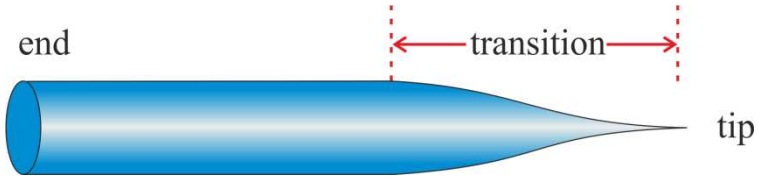

Figure 1-2 Schematic of an optical fibre tip.

Optical fibre tapers can be described as a three layer waveguide. The cross sectional profile anywhere along the taper consists of a core embedded in a finite cladding, which is normally surrounded by air (Figure 1-3). The refractive index of core, cladding and air is n_1, n_2 and n_3 respectively.

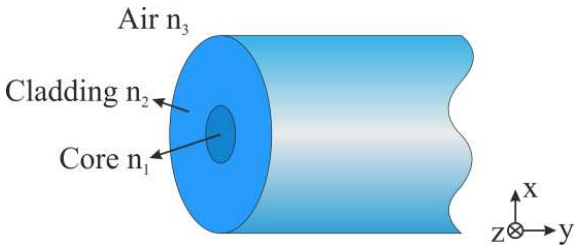

Figure 1-3 Waveguide structure of optical fibre tapers. n_1, n_2 and n_3 are the refractive indices of core, cladding and air, respectively.

The propagation constant and the effective index are critical for describing light propagation and the intensity profile in optical fibre tapers. In order to get propagation constants or effective indices, Maxwell's equations need to be solved for the geometry described in Figure 1-3. When the core size is considerably smaller than the wavelength propagating into the fibre taper, its effect can be neglected and propagation is reduced to the solution of Maxwell's equations for a cylindrical waveguide in a surrounding infinite medium. Because of the large refractive index difference between the

waveguide and the surrounding medium (usually air), the weak guidance approximation ($n_1 \approx n_2$) does not apply and propagation equations yield to the solution of eigenvalue equations for the hybrid modes HE_{vm} and EH_{vm} [36] in cylindrical symmetry:

$$[\frac{J_v'(U)}{UJ_v(U)} + \frac{K_v'(U)}{WK_v(U)}][\frac{J_v'(U)}{UJ_v(U)} + (\frac{n_2}{n_1})^2 \frac{K_v'(U)}{WK_v(U)}] = v^2(\frac{1}{U^2} + \frac{1}{W^2})(\frac{1}{U^2} + (\frac{n_2}{n_1})^2 \frac{1}{W^2}) \quad (1\text{-}1)$$

where $U = a\sqrt{k_0^2 n_1^2 - \beta^2}$, $W = a\sqrt{\beta^2 - k_0^2 n_2^2}$, J_v is the v^{th} order Bessel function of the first kind, K_v is the v^{th} order modified Bessel function of the second kind, v is the first subscript of the considered mode HE_{vm} and EH_{vm}, a is the core radius if the core-cladding model is considered, the cladding radius if the cladding-air model is used, and k_0 is the wave vector in free space. The propagation constant β of hybrid modes can be calculated by solving Equation (1-1).

If light is launched into a fibre taper, modes propagate as core modes which are defined to be the state when their effective index lies between the cladding and core indices at the beginning of the taper. As the fibre tapers down, its effective index decreases monotonically, the mode becomes guided by the cladding/air interface and the effective index can reach values smaller than the cladding index.

It is important that light propagates along the taper with no power loss from the fundamental mode [9]: this taper is called 'adiabatic taper'.

In 1991, J. D. Love proposed a 'length scale criterion' which provides guidelines to the design of relatively short, low-loss fibre tapers [37]. The criterion is based on the physical argument that the local taper length-scale must be much larger than the coupling length between the fundamental mode and the dominant coupling mode for the power loss to be small. If β_1 and β_2 are the propagation constants of two modes, this adiabatic taper angle can be described as:

$$\overline{\Omega} = \frac{a(\beta_1 - \beta_2)}{2\pi} \quad (1\text{-}2)$$

If the taper angle $\Omega < \overline{\Omega}$, tapers are adiabatic, while for $\Omega \geq \overline{\Omega}$, tapers are non-adiabatic. At a local cladding diameter, β_1 and β_2 were calculated and the

adiabatic taper angle was obtained according to equation (1-2). Adiabatic profiles for different wavelengths were obtained and plotted in Figure 1-4.

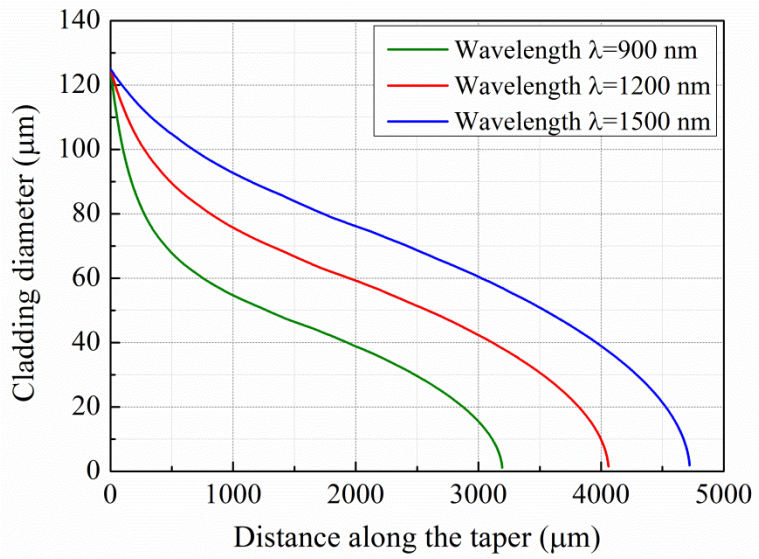

Figure 1-4 Adiabatic profile of the fibre taper (cladding diameter versus the distance along the taper) for three wavelengths λ=900 nm, 1200 nm, and 1500 nm.

From Figure 1-4, the longest wavelength should be considered to choose the mostly adiabatic taper because the longer wavelength represents the worst case scenario for the adiabatic profile.

1.1.1.2 Optical fibre taper manufacture

Although many technologies have been utilized in manufacturing tapers, there are four methodologies used to manufacture most of optical fibre tapers with sub-micron diameters: tapering the fibre by pulling it around a sapphire rod heated by a flame [26], the flame-brushing technique [38], the modified flame-brushing technique [2] and *Hydrofluoric* (HF) etching [39, 40].

The first method was reported by L. Tong et al. [26] in 2003, and it is based on a two-stage process involving a heated sapphire tip. Firstly, a micrometric taper manufactured by the flame brushing technique is broken and then it is wrapped around a hot sapphire tip which is used to draw the optical fibre taper in the second step. Although this technique has shown the capability to manufacture optical fibre tapers with radii of ~10 nm, it also provides high losses and only one fibre pigtail because of the intrinsic nature of the process.

In the flame brushing technique, a small flame moves under an optical fibre which is being stretched [41]. The flame brushing process provides the longest

and most uniform optical fibre tapers with the lowest measured loss which is close to the theoretical minimum and highest strength. Moreover, this technique can maintain the optical fibre tapers intact and fibre pigtails at both optical fibre tapers ends allowing a convenient connection to fibre components. Figure 1-5 shows a simplified diagram of this method [42]. The extremely high accuracy of taper shape can be obtained by controlling the flame movement and the stretching rate.

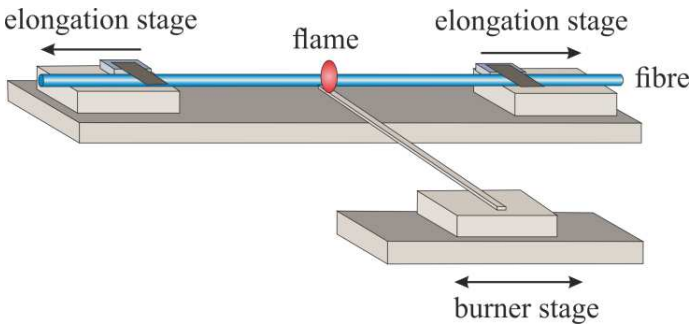

Figure 1-5 Schematic of the flame brushing technique.

The third manufacturing method replaces the heat source of the flame brushing technique. A sapphire tube heated by a CO_2 laser and a microheater have been used as heat sources. This technique can provide short optical fibre tapers with similar quality to the flame brushing technique and is not limited to silica but it can deal with a wide range of glass. In Figure 1-6, the burner in the flame brushing technique is replaced with a microheater and it can be used to manufacture fibre tapers from soft glasses and avoid any excess hydroxyls in the silica tapers [2].

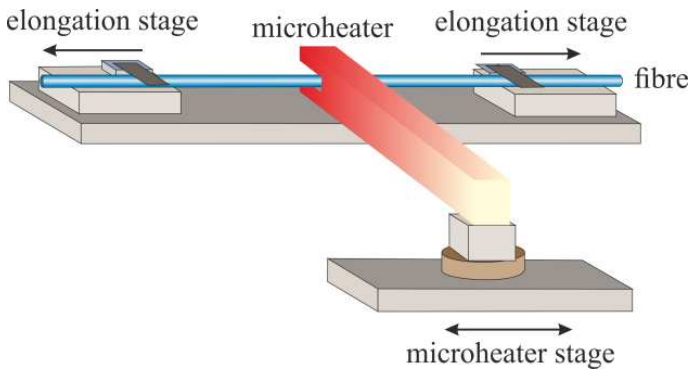

Figure 1-6 Illustration of the set-up for drawing optical fibre tapers using a microheater.

HF etching has been used to manufacture optical fibre tapers. This class of methodologies relies on the physical removal of material from the fibre surface using acids, which in a controlled environment allows a relatively accurate and constant etch rate. Etching speeds of 50-100 nm/s are common with this technique for highly concentrated HF acids at room temperature. Although etching does not require much equipment for the manufacture of fibre tapers, it also provides a sample with poor surface roughness quality [40] and therefore a high propagation loss.

If only a fiberized pigtail is needed, the simplest and quickest way to fabricate optical fibre tips is using a commercial machine which exploits a working principle similar to the modified flame brushing technique explained above. Figure 1-7 shows a P-2000 micropipette puller (SUTTER INSTRUMENT Inc., Novato, USA) which is a CO_2 laser based pulling machine controlled by a microprocessor. The default configuration of the P-2000 allows the fabrication of optical fibre tips with extremely small diameters: typically, fibres can be pulled from 125 μm down to 40 nm diameters and have a taper length of about 1 mm. Although the pipette puller is a convenient machine to fabricate fibre tips, it has drawbacks: samples can have only one pigtail and reproducibility is very poor. It is difficult to obtain tips with the same profile even using the same parameters because the machine is extremely sensitive to the environment. Therefore, this method requires sample characterization after manufactured. More details will be discussed in Chapter 2.

Figure 1-7 Picture of P-2000 micropipette puller (SUTTER INSTRUMENT Inc., Novato, USA).

1.1.2 *Nanostructuring techniques*

The requirement of feature sizes smaller than 100 nm motivates the development of nanofabrication methods. Several techniques have been used in nanofabrication. All of these methods have broad flexibility in nanopatterning and can fabricate structures with dimensions in the range of few nanometres to few hundred micrometres. In this section, five technologies will be discussed [43].

The first one is photolithography. Photolithography is widely used in the *Integrated Circuit* (IC) manufacture. It uses light to transfer a geometric pattern from a photomask to a light-sensitive chemical (photoresist) on the substrate. However, this approach is limited by the diffraction limit which is in the order of the wavelength in free space.

Another method is X-ray lithography [44] which represents the short-wavelength limit. Although structures as small as 30 nm have been achieved, the implementation of this technique in IC production is still difficult because there is no commercial way to produce the masks, mirrors tend to be lossy and processing needs to be performed in vacuum. Moreover, the reproducibility is bad due to the challenges related to the mask positioning close to (but out of physical contact from) the substrate.

Laser nanofabrication (i.e. *Femtosecond* (*fs*) laser) has been extensively applied in the industry, to carry out marking, drilling, annealing, and surface modification, as a reliable energy source in cost-effective manufacturing systems. As a maskless and noncontact process, laser nanofabrication has its unique advantages in a flexible setup, able to be operated in air, vacuum or liquid environment, which makes it as the most attractive processing or manufacturing tool for much more extensive applications. However, it is also limited by diffraction.

Focused electron beam can also be used to fabricate nanostructures in electron-sensitive resist films [45]. Electron beam writers are not limited by diffraction and are mostly used to produce photomasks in optical lithography or to produce small numbers of nanostructures for research purposes. The key limitation of electron beam lithography is throughput, i.e., the very long time it takes to expose an entire silicon wafer or glass substrate. A long exposure

time leaves the user vulnerable to beam drift or instability which may occur during the exposure.

Focused Ion Beam (FIB) is another attractive tool primarily used for generation of patterned nanostructures, repair of defects in photo- and X-ray mask, inspection in IC processes, failure analysis, and surface characterization. To some extent, the FIB resembles a *Scanning Electron Microscope* (SEM), the major difference being the use of a gallium ion (Ga^+) beam that can be operated at low beam currents for imaging or high beam currents for sputtering or milling instead of an electron beam.

As shown in Figure 1-8, the Ga^+ primary ion beam hits the sample surface and sputters a small amount of material, which leaves the surface as either secondary ions (i^+ or i) or neutral atoms (n^0). The primary beam also produces secondary electrons (e^-). As the primary beam raster scans on the sample surface, the signal from the sputtered ions or secondary electrons is collected to form an image. At low primary beam currents, very little material is sputtered and modern FIB systems can easily achieve a 5 nm imaging resolution. At higher primary currents, a great deal of material can be removed by sputtering, allowing precision milling of the specimen down to dozens of nanometres.

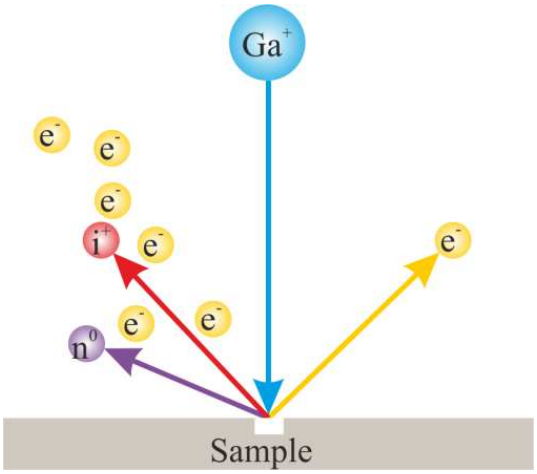

Figure 1-8 Principle of FIB.

Compared with electron beam lithography, FIB has higher resist exposure sensitivity, higher efficiency, negligible ion scattering in the resist and very low backscattering from the substrate. However, the damage to samples because of the material re-deposition is a major problem in FIB. In the following work,

we use FIB to nanostructure optical fibre tapers. Figure 1-9 gives a SEM image of a "Light" logo of Optoelectronics Research Centre, University of Southampton written on silicon with 35 nm minimum linewidth using the FIB system “Helios 600” (FEI Inc., Hillsboro, USA).

Figure 1-9 SEM image of “Light” logo of Optoelectronics Research Centre (ORC), University of Southampton. (Fabricated by Jun-Yu (Bruce) Ou in ORC)

1.2 Motivations and key achievements

In recent years, optical fibre tapers have attracted much attention and found a wide range of applications because of their unique properties [35]. Simultaneously, nanofabrication techniques have been used widely to manufacture features smaller than 100 nm [43]. This thesis combines the two fields, exploring nanostructured optical fibre tapers and related applications.

The first device introduced in this thesis is the sub-wavelength light confinement source. Since the diffraction limit relates to the wavelength of the propagation light and to the refractive index of the medium where light is focused, this becomes a limitation to optical imaging and focusing systems [46]. In this thesis, an efficient sub-wavelength light confinement source capable to focus relatively high powers is proposed to overcome the diffraction limit, which can be exploited in optical memory, SNOM, photolithography etc.. Theoretical simulations using COMSOL Multiphysics have been carried out to predict optima and provide a reference for the device fabrication. Spot sizes as

small as ~λ/15 and transmission efficiencies in the order of 10^{-2} have been obtained in the experiments. The device is very stable with temperature and no shape changes could be detected within the accuracy of the SNOM system which was used to test the thermal expansion.

The second group of devices relate to microcavities. Since resonators based on optical microcavities can confine light in a small volume by resonant recirculation and have been demonstrated in several structures, they have been used in a wide range of applications [47]. Microcavities were manufactured in optical fibre tapers and 3D light confinement was achieved in *Microfibre Phase-Shifted Bragg Gratings* (MPSBG) nanostructured by FIB. In this work, only dozens of periods can achieve high reflectivities because of the large refractive index contrast between silica and air. Therefore, the size of the device is extremely small (tens of micrometres long and few micrometres wide).

A third device is an ultracompact thermometer. Temperature measurement is vital for many applications in harsh environments, such as the oil and gas industries, power generation, or engine turbines. Temperature sensors using optical fibre devices have been developed because of their immunity to electromagnetic interference and possibility to work in contact with explosives [48-51]. For example, *Fibre Bragg Grating* (FBGs) inscribed in telecom optical fibres, can reach temperatures T as high as 1295ºC [52]. However, FBG high temperature sensor requires speciality fibres, complex process, and big size. The *Microfibre Coupler Tips* (MFCT) high temperature sensor demonstrated in this thesis can reach up to 1511ºC which is the highest temperature measured with a silica optical fibre device. The response time is very fast and the responsivity is comparable to the value obtained from FBGs thermometers at low temperature [53, 54]. This temperature sensor offers several advantages, including compactness, extremely high temperature measurement capabilities, fast response, easy connection with other fiberized optical components, simple fabrication and low cost.

A fourth class of devices relate to mode selectors in high-Q resonators. Nanostructuring has been used to select a specific *Whispering Gallery Mode* (WGM) in optical *Bottleneck Microresonators* (BMRs) in Chapter 5. In BMRs, the spectrum is very dense because of the strongly broken degeneracy between WGMs with common azimuthal and differing axial mode numbers. Such spectral characteristics are a serious hindrance if BMRs are to be used as

sensors, where a spectrum with features more easily identifiable and traceable over large wavelength ranges is desirable. In our work, microgroove scars were inscribed on the BMR surface by FIB and used to clean-up the resonator spectrum. A single high-*Q* mode was predominantly selected using two asymmetrical perpendicular scars. This technique can also be employed to clean-up spectra in other types of non-spherical micro-resonators [55].

Finally, the fifth and last group of nanostructured optical fibre tapers considered in this thesis are the *Plasmonic Slot Nano-Resonators* (PSNRs) embedded in metal-coated optical fibre tapers. Nanoscale apertures in thin noble-metal films, with dimensions comparable to the light wavelength, can form *Plasmonic Nano-Resonators* (PNRs) and show astonishing optical properties leading to enhanced and selective light transmission and confinement. At resonance, such structures can concentrate an incident light field into a small volume with orders-of-magnitude intensity enhancement. PNRs can provide hot spots in the near-field with dimensions determined mainly by the structure size rather than by the diffraction limit. Differently from other PNRs, where excitation occurs under plane-wave excitation directed perpendicularly to the plane of the resonator [56, 57], in this thesis light is launched from one end of the fibre taper and the various resonances can be identified simply monitoring the transmitted and reflected light. Simulations show that a single PSNR has enhancement factors in excess of 9×10^5. A rectangular PSNR embedded in a thin gold film plasmonic fibre tip was demonstrated theoretically and experimentally. The electric field was highly localized in the cavity centre. The strongest enhancement factor 7.24×10^3 was achieved for the resonance at the wavelength $\lambda\sim1450$ nm, recorded when light was polarized perpendicularly to the PSNR. This device can find a wide range of applications such as *Surface-Enhanced Raman Scattering* (SERS), optical filtering, spectroscopy and bio-sensing.

1.3 Outline

Chapter 2 presents preliminary studies on the efficient 2D sub-wavelength light confinement of high powers in apertured optical fibre tips. The

background on diffraction limit and methods to overcome the diffraction limit are summarized in Section 2.1, together with some applications. In Section 2.2, theoretical simulations are discussed to predict the optimal device design, e.g. the transmission efficiency dependence on aperture size, slope angle, coating materials, coating thickness and operation wavelength. Devices fabrication is introduced in Section 2.3 and is divided into four steps (i) manufacture of optical fibre tips, (ii) tip milling, (iii) gold layer deposition, and (iv) aperture opening at the coated fibre tip apexes. Finally, Section 2.4 presents the characterization experiment and the result analysis.

In Chapter 3, 3D light confinement is achieved using microcavities in optical MPSBG. The fibre grating theory and optical microcavities are briefly reviewed in Section 3.1. *Microfibre Bragg Gratings* (MFBGs), including the working principle, fabrication, characterization and numerical modelling are firstly studied in Section 3.2, which gives a reference to the MPSBG. Section 3.3 discusses MPSBGs both in experiments and in simulations. Finally, a conclusion is drawn in Section 3.4.

A fast response *microfibre coupler tip* (MFCT) high temperature sensor is demonstrated in Chapter 4. A short review on temperature sensing is summarized in Section 4.1. Section 4.2 presents the MFCT temperature sensor fabrication. The temperature dependence of this temperature sensor is discussed in Section 4.3. The properties of the MFCT are given in Section 4.4. Section 4.5 summarizes this work.

Chapter 5 represents a method to excite selected WGMs in optical *bottleneck microresonators* (BMRs) by inscribing microgroove scars on their surface by FIB milling. Section 5.1 gives a background of BMRs and the current methods used to clean-up the spectrum. Section 5.2 introduces the design of microgrooves and the microgrooves fabrication. The properties of the nanostructured BMRs are investigated by placing a tapered fibre to couple the light in and out of the BMRs. Taper transmission spectra for different taper positions are presented and analysed in Section 5.3. Section 5.4 gives a theoretical explanation of the spectra behaviour in Section 5.3 in details. The work is concluded in Section 5.5.

Chapter 6 focuses on *plasmonic slot nano-resonators* (PSNRs) embedded in metal-coated optical fibre taper. Section 6.1 introduces the current research on

plasmonic nano-resonators (PNRs). A strongly-coupled 3D PSNR-by embedding a slot nano-cavity in a plasmonic cylindrical waveguide formed by a thin-metal-film coated microfibre-is studied theoretically in Section 6.2. Section 6.2.1 presents the modelling of bow-tie and rectangular PSNRs embedded in cylindrical plasmonic waveguides. Section 6.2.2 explores the resonance wavelength and intensity enhancement dependence on the PSNR geometry. Section 6.2.3 discusses the resonance characteristics and intensity enhancement in cascaded multiple bow-tie PSNRs. Section 6.3 and Section 6.4 present the study, both theoretically and experimentally, of the transverse excitation of a strongly-coupled 3D PSNR by embedding a rectangular slot nano-cavity in a plasmonic structure formed by a thin-metal-film coated fibre tip. A conclusion is drawn in Section 6.5.

Finally, Chapter 7 concludes the thesis and presents the potential future works.

Chapter 2 Two dimensional light confinement with nanostructured optical fibre tips

> Above all, don't fear difficult moments. The best comes from them.
>
> Rita Levi-Montalcini

In this chapter, nanostructured optical fibre tips are proposed and experimentally demonstrated to efficiently confine light beyond the diffraction limit at high powers. *Focused Ion Beam* (FIB) milling is used for the nanostructuring of gold-coated optical fibre tips with both single-ramp and wedge geometries. Small apertures are formed by flat cutting or hole drilling and optical spot sizes of ~λ/15 with high transmission efficiency are achieved. Numerical simulations are carried out to optimize the device design with circularly polarized light. Enhanced transmission efficiencies (higher than 10^{-2}, compared with 10^{-4}-10^{-5} in common SNOM probe) are achieved by optimizing the overall light throughput along the fibre tips. The tip thermal behaviour is investigated by launching high powers into the device and recording the tip

M. Ding, O. Fenwick, F. Di Stasio, J.-Y. Ou, N. Sessions, Y. Jung, F. Cacialli, and G. Brambilla, "Efficient light confinement with nanostructured optical microfibre tips," *Opt. Commun.* **285**, 4688-4697 (2012).

position in a *Scanning Near-field Optical Microscope* (SNOM) set-up. This nanostructured optical fibre tip has the potential for applications in optical recording, SNOM and lithography.

2.1 Background

2.1.1 Diffraction limit

The resolution of an optical imaging system can be limited by lens quality or misalignment. However, there is a fundamental limitation which is due to diffraction. Diffraction comes from the wave property of light and is determined by the finite aperture of the optical component. It was expressed more than one century ago by Ernst Abbe and later reformulated by Lord Rayleigh. Abbe's definition of the refractive index relates the mimimum spatial detail that can be resolved to the wavelength of light used [58]:

$$\Delta x \geq \frac{\lambda_0}{2n\sin\theta} \geq \frac{\lambda_0}{2n} \tag{2-1}$$

where Δx is the minimum spatial detail, θ is the angular resolution, λ_o is the light wavelength in free space and n is the refractive index.

In recent years many methods of breaking this diffraction limit have been developed, leading to optical resolution significantly smaller than the ~λ/2 diffraction limit being achieved. The following section will discuss some of these methods.

2.1.2 Methods to overcome the diffraction limit

To overcome the diffraction limit, several techniques have been proposed, including metamaterials [59-63], high index contrast waveguides [64], optical fibre with a sub-wavelength air core [65], micro/nanofibre array [66], tapered microtube [67], longitudinal evanescent waves/ SNOM [68-70], and *Surface Plasmons* (SPs) [71-74].

2.1.2.1 Metamaterials

In 1967, V. Veselago [75] proposed a new material with a negative index of refraction which is not limited by diffraction (called metamaterial). Figure 2-1 shows that in this case radiation will be focused on a spot when a point source transmits radiation to a plane-parallel plate of this material, though the plane plate is not a lens.

The idea of the negative index media lens remained obscure for some decades after V. Veselago proposed it, primarily because no such material exists in nature. In the late 1990s, J. B. Pendry [76] proposed that electromagnetic resonances in artificially engineered metamaterials made of metal loops and wires could reach values not accessible in natural materials.

Soon after Pendry's theoretical proposal, experimental attempts to test the superlens concept began. An image below the diffraction limit (at $\lambda/5$) was reported at ~1 GHz frequency by using a negative index planar transmission-line structure [77].

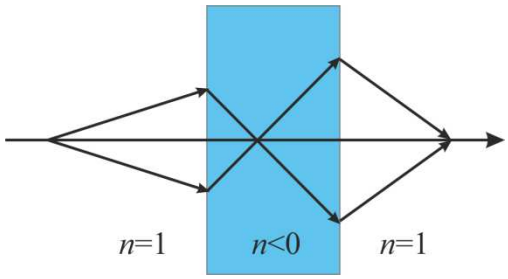

Figure 2-1 Beam path in a plane-parallel plate made from a material with $n<0$.

2.1.2.2 High index contrast waveguide/ optical fibre with a sub-wavelength air core

Guiding light in low index materials such as air is thought to be prohibited in conventional waveguides based on total internal reflection. However, in 2004, Q. Xu [64] proposed a structure that has a low index (silicon oxide) nanometre wide area embedded in a high index material medium (silicon). In this proposed waveguiding structure, the optical field can be enhanced and confined in a low refractive index material because of the discontinuity of the electric field at high index contrast interfaces between silicon and silicon oxide even when light is guided by total internal reflection.

G. S. Wiederhecker demonstrated the concentration of optical energy within a sub-wavelength-scale air hole running down the length of photonic crystal fibres core in 2007 [65]. The core resembles a sub-micrometre diameter tube. In such a small waveguide, guided light is not tightly confined within the high index glass, but also extends into the low index material surrounding it. The evanescent light decaying into the central hole decays about 2% before meeting the opposite side at wavelength λ=900 nm when the hole diameter is 100 nm. This ensures a stronger electric field inside the bore in air than just outside it, in the silica. The very low effective refractive index of the cladding maximizes the power fraction inside the bore and ensures that the mode remains guided.

2.1.2.3 Microfibre arrays/tapered microtubes

A structure based on-micro/nanofibre arrays has been used to focus optical beams with sub-wavelength resolution in the far-field [66]. By optimizing the structure with numerical simulations, spots with *Full Width at Half Maximum* (FWHM) of 0.43 λ at a distance of 9 λ from the output end face of the micro/nanofibre array were obtained. Sub-wavelength far-field focusing was also proposed with a tapered microtube fabricated from a glass capillary [67]. Experimental results revealed the smallest spot, with a near diffraction-limited FWHM of 0.65 λ, was positioned at a distance of 2.2 λ from the output end face of the microtube. Although these two techniques allow for far-field focusing, they provide only limited confinement, which is typically few hundreds nanometres.

2.1.2.4 Longitudinal evanescent fields

Longitudinal evanescent fields have been exploited to obtain sub-wavelength confinement of light in metal-coated tips (Figure 2-2) and found applications in SNOM systems [78-82]. Yet, SNOM probes have very low transmission efficiencies, e.g. 10^{-3} ~10^{-6} [79, 83], as they require small apertures and small tapering angles, which results in a strong decay in the evanescent field intensity. Also, they usually can only support relatively small powers, typically of the order of 1 mW, above which they experience a catastrophic damage by melting.

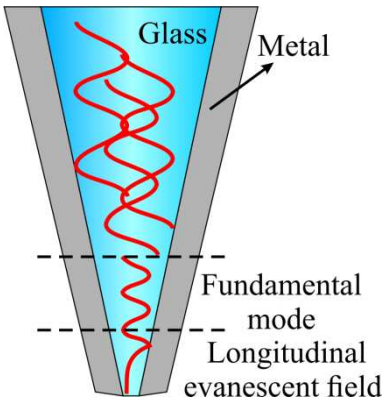

Figure 2-2 The schematic of light propagation in metal-coated tips, showing longitudinal evanescent field after fundamental mode cut off.

2.1.2.5 Plasmons

Another common technique to overcome the diffraction limit is using plasmons in sub-wavelength structures. *Surface Plasmons* (SPs) are electromagnetic excitations propagating at the interface between a dielectric and a conductor, evanescently confined in the perpendicular direction. These electromagnetic surface waves arise via the coupling of the electromagnetic fields to oscillations of the conductor electrons and are possible only when the vacuum propagation constant of light matches the SP propagation constant along its direction of propagation. Confinement is achieved since the propagation constant is greater than the wave vector, leading to evanescent decay on both sides of the interface. Extreme confinement can be achieved because SPs do not experience diffraction in the region of the wavelength in free space.

Devices based on SPs have been proposed and experimentally demonstrated for efficient sub-wavelength light confinement, but they always dealt with small powers and mostly in planar geometries. In 2007, W. Ding [84] proposed an apertureless silver-coated optical fibre tip in which the radially polarized waveguide modes of an optical fibre taper were converted into plasmons propagating at the outer surface of the tip. Although they are predicted to have extremely high transmission efficiency, apertureless optical fibre tips with high transmission efficiency have never been manufactured [85, 86]. On the contrary, apertured tips have been widely used in light nano-focusing, albeit without the aid of the SPs [79, 87-89]. In 2009, apertured tips exploiting the SPs to confine light to sub-wavelength spot sizes ($\lambda/3$) in optical fibres and fibre tapers were realized [90, 91]: the use of the SPs improved transmission efficiency by several orders of magnitude. Yet, the use of SPs

limits the minimal spot size, as the radial component of the evanescent field becomes increasingly more important for reducing aperture sizes.

In this work, an efficient sub-wavelength light confinement source capable to focus relatively high powers is proposed by nanostructuring an optical fibre tip. Its design for the case of circularly polarized light is discussed and some examples of fabrication shown.

2.1.3 Applications of fibre sub-wavelength sources

High transmission efficiency and high powers are fundamental requirements for many applications, which include amongst others data recording, imaging and photolithography.

2.1.3.1 Optical memory

Optical storage relies on the phase change of a glassy (mainly chalcogenide (its crystalline and amorphous states represent binary 0 and 1 respectively)) thin layer of a disc exposed to a focused laser beam. The *Compact Disc – Read Only Memory* (CD-ROM) was the first important example of optical storage and it used a 1.2 mm thick disc of polycarbonate plastic with a thin layer of aluminium to store up to 703.1 MB of data using a 780 nm laser. Few years later, the *Digital Versatile Disc-Read Only Memory* (DVD-ROM) used a shorter wavelength (λ~650 nm) to phase change a smaller area of the media surface compared to CDs (1.32 μm versus 1.6 μm for CD), allowing for a storage capability of 4.7 GB for a single-sided single layer and 8.54 GB for a single-sided double layer. 2006 saw the release of the *Blu-ray Disc* (BD) which can store up to 128 GB. The improvement in the data storage was made possible mainly by the use of a semiconductor laser diode with a reduced wavelength of 405 nm and a high refractive index lens. All existing commericial methods to improve the storage capability in CD, DVD and BD rely on the shift of the diffraction limit to smaller sizes by reducing the laser wavelength and increasing the refractive index. Multilayer [92, 93] and holographic [94, 95] recording are being investigated as an alternative route. Sub-wavelength light confinement devices can be used to improve further the storage capability [91, 96]. If spot sizes smaller than 30 nm are used, storage in excess of 1 TB can be predicted on a single disk.

In *All-Optical Magnetic Recording* (AOMR), high storage capability is obtained by efficiently delivering optical energy which reverses the magnetization in a spot on the medium that is much smaller than the diffraction limit. In AOMR, circularly polarized light should have the ability to act upon a magnetic system in a way similar to a magnetic field directed parallel to the wave vector of the light via the inverse Faraday effect [97, 98]. Moreover, right- and left-handed circularly polarized waves should act as magnetic fields of opposite signs. This effect was only recently confirmed experimentally [99, 100] and has also been demonstrated to be an efficient tool for coherently controlling the small angle processional magnetization dynamics in magnetic dielectrics [101, 102].

2.1.3.2 Near-field optical imaging

Near-field optical imaging, usually referred as SNOM, is another important application of fiberized sub-wavelength sources. This technique is used for optical investigation and breaks the observed far-field resolution limit by exploiting the properties of evanescent waves of the near-field. This is done by placing the probe very close to the specimen surface (typically in the region of 10 nm) and allows for surface inspection with high spatial, spectral and temporal resolution. In this technique, the image resolution is limited by the size of the probe aperture and not by the wavelength of the illuminating light. Light from a laser is sent to a fibre and then to a sub-wavelength aperture, in the tapered end, which is positioned very near to the sample [69]. Collecting the reflected or transmitted light with a normal optical system and with a light detector, it is possible to achieve image resolutions better than ~100 nm [79]. The scanning tip, depending upon the operation mode, is usually a tapered or etched optical fibre coated with metal [79, 103, 104] or a standard atomic force microscope cantilever with a hole in the centre of the pyramidal tip [105]. The transmission efficiency of the scanning tip affects the quality of the images.

2.1.3.3 Photolithography

Photolithography is a process used in microfabrication to selectively remove parts of a thin film (or of a substrate). It uses light to transfer a geometric pattern from a mask to a light sensitive chemical (photoresist) on the substrate. In order to have more complex *Integrated Circuit* (IC) [106, 107], the

aim of photolithography is to reduce feature sizes as much as possible. In previous years, the technological limit has been related to the focusing of light and the way forward was to reduce the wavelength of the light used for the exposure of the photoresist. As a result, this method is subject to the diffraction limit. Current state-of-the-art photolithography tools use deep ultraviolet light with wavelength 193 nm and immersion lithography and/or mask shifting, which allow minimum feature sizes down to 32 nm [108].

A fiberized sub-wavelength light source can be used to overcome the diffraction limit and it can be used in the photolithography world in three ways. One consists in directly "writing" the photoresist layer [83, 109]. The fiberized sub-wavelength light confinement source can be conceived like a "pen". Using a matrix of pens the exposure time for the wafer can be substantially reduced. The second application of sub-wavelength light sources is for mask repair. Masks that are used for photolithography are extremely expensive. The possibility to have a light source to repair a mask with sufficient detail can increase the mask life span, thus decrease its overall cost. Finally, another important application is the diagnosis of defects. In fact, at the moment, there is no way to investigate defects with size smaller than 22 nm [110, 111].

In some cases, for example for organic semiconductors, it is also possible to write directly the final semiconductors nanostructures by exposure to optical evanescent waves without the use of a sacrificial resist [89].

2.1.3.4 Fibre-based *Surface Plasmon Resonance* (SPR) sensor

SPR devices have also been integrated in optical fibres and used as sensors for liquid and gas phase analyses. Compared with other sensors, a fibre-based sensor is fundamentally simpler in construction, requires a small sample volume, and can be used for remote sensing applications. In this sensor, the reflection characteristics of the metal film are highly sensitive to refractive index variations in the sample medium. Y. Kim reported single-crystal sapphire-fibre optic sensors based on SPR for refractive index measurements of aqueous and hydrothermal water solutions in 2005 [112]. However, sensors based on sub-wavelength light confinement sources have additional advantages: they can be put into extremely small volumes due to the extra

small size of the tip; moreover, this device can be shaped using high precision milling machines, difficult to use with fibres because of their big size.

2.2 Device design and numerical analysis

2.2.1 *Device design*

In this section, nanostructured optical fibre tips are optimized to improve transmission efficiency at high transmitted powers.

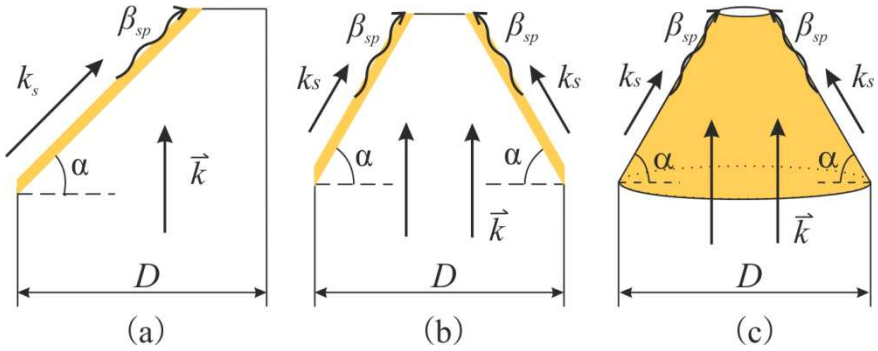

Figure 2-3 Schematic of (a) single-ramp sample, (b) wedge sample and (c) cone sample. α represents the slope angle. β_{sp}, $\vec{k}$ and k_s represent the surface plasmon propagation constant, the light wave vector and its component along β_{sp}, respectively. D is the diameter of fibre tip.

Three structures with a thin layer of gold (thinkness is in the order of dozens of nanometres) and an extremly small aperture (diameter is less than 100 nm) in the apex have been investigated: the single-ramp (Figure 2-3 (a)), where one surface was cut at a specific angle α; the wedge (Figure 2-3 (b)), where two surfaces were cut with the same slope within the instrument resolution; and the cone (Figure 2-3 (c)), which can exploit the various polarization directions when circularly polarized light is used. While the first design is easier to fabricate, the second and third designs offer a shorter light path for a given fibre tip diameter. Since light propagation is not permitted in coated sub-wavlength diameter waveguides, only a longitudinal evanescent field exists; the evanescent wave experiences exponential attenuation along its path, thus a shorter path assures higher transmission efficiency. α is the free parameter chosen to optimize transmission and beam confinement.

Simple mathematical manipulations show that SPs can be excited when transversely magnetic polarized beams hit the interface between the metal

(gold in this work) and dielectric at a specific slope angle α_{sp}. Resonance occurs when the projection of the light wave vector on the newly formed surface ($k_x = k\sin\alpha$) equals the SPs propagation constant β_{sp} in the same direction (Figure 2-3). This phase matching condition can only be fulfilled at the gold/air interface. The resonance condition can be expressed as:

$$\alpha_{sp} = \arcsin\left(\frac{1}{n_{eff}}\sqrt{\frac{\varepsilon_{gold}\varepsilon_{air}}{\varepsilon_{gold}+\varepsilon_{air}}}\right) \tag{2-2}$$

where n_{eff} is the effective index of the mode (which decreases for decreasing fibre tip diameters), ε_{gold} and ε_{air} are the dielectric constants of gold and air, respectively. Although SPs can aid the power confinement, they also exhibit a radial exponential dependence, which limits the ultimate tight confinement over small spot sizes. For this reason designing the slope angle α is the most important feature for efficient light confinement.

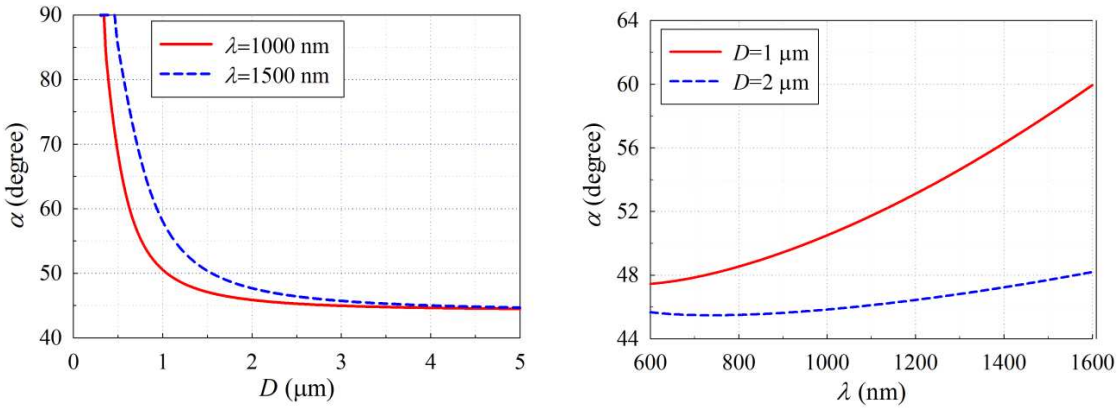

(a) (b)

Figure 2-4 Dependence of slope angle α on (a) fibre tip diameter D and (b) wavelength λ for a SP excitation.

Figure 2-4 shows the dependence of α on the fibre tip diameter and on the wavelength for SP excitation. Figure 2-4 (a) shows that α varies from 44° to 90° for tip diameters D ranging from 0.3 μm to 5 μm. Figure 2-4 (b) reveals that α varies more than 10° in the wavelength range 600-1600 nm and that the smaller is D, the stronger is the dependence of α on the wavelength. As a result, in tips not only λ but also D can be used to fulfil the resonance condition. In our experiments, fibre tips with D~1 μm were chosen because they provide a tight confinement, a reasonable stiffness and better tolerance to

nanostructuring imprecision: in tips, a small imprecision in α results in a shift of the SP resonance peak wavelength that is relatively small: a 100 nm wavelength shift is observed for an angle imprecision of 0.1° when D=5 μm.

2.2.2 Numerical analysis

In order to optimize the fibre tip design and obtain high transmission efficiencies η which is the ratio of the output power and input power, theoretical analysis was carried out using 3D finite element method to numerically solve Maxwell equations in the frequency domain. The numerical model was defined, solved and analysed using the commercial software COMSOL 3.5a Multiphysics.

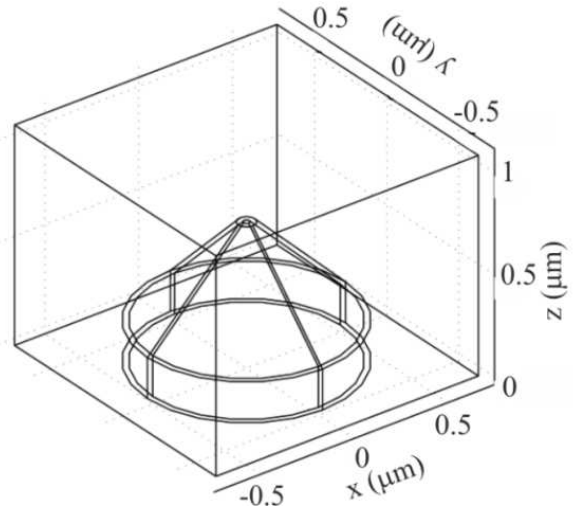

Figure 2-5 Geometry of the modelled conical cut structure.

In AOMR, circularly polarized light is the most favourable polarization because it leads to three desirable features for the optically-induced magnetization: a relatively high spatial confinement, a direction nearly perpendicular to the opto-magnetic medium and a large magnitude [113, 114]. For this reason, light with circular polarization is launched into the fibre tip conical cut structure shown in Figure 2-5. The fibre tip, made from a telecom single mode fibre (SMF-1300/1550-9/125-0.25-L (OZ optics, Canada) which has ~8.2 μm core diameter, ~125 μm cladding diameter, ~0.12 numerical aperture and 1250 nm cut-off wavelength), has 1 μm diameter after pulling and was operated at the input wavelength λ=800 nm; a layer of gold is coated on the optical fibre tip and an aperture is opened at its apex. The dispersion of the gold's real and imaginary parts of the refractive index is taken into account

from the Drude model [115]. The tip is surrounded by air in a box aimed to avoid reflections from the boundary. The chosen boundary conditions were: scattering boundary condition in the exterior boundary and continuity boundary condition in the interior boundary (the definitions of boundary conditions are presented in Appendix A). Simulations were run with different mesh size to choose an optima mesh size. Controlled mesh size (50 nm in silica, 10 nm in gold coating and 100 nm in air surrounding) was selected to make efficient use of computer memory and ensure the accuracy of the modelling results.

Firstly, the modelling assumed a coating thickness t=20 nm, an aperture diameter d=30 nm, and a slope angle of α=48.713° (chosen according to Figure 2-4). This angle was chosen to take advantage of SPs for energy confinement. The refractive index of gold, silica and air were assumed to be 0.1808-5.11731i [115], 1.45, and 1 at the wavelength λ=800 nm, respectively. Figure 2-6 shows the electric field distribution across the x-z plane passing through the tip longitudinal axis. From the electric field plot, the field experiences a considerable enhancement at the tip apex. It is also evident that strong radial evanescent fields are present outside the tip for z~0.6 μm.

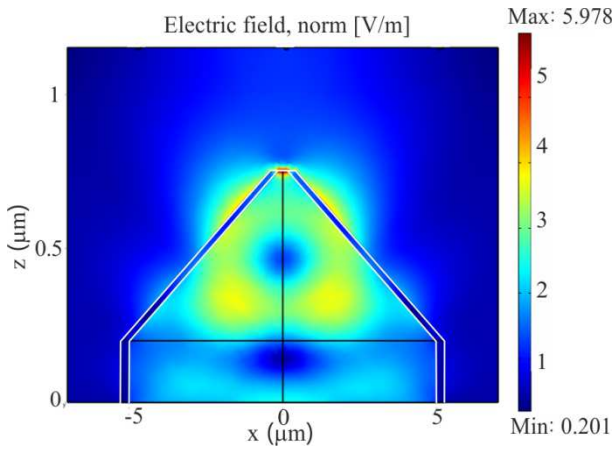

Figure 2-6 Electric field distribution across the x-z plane passing through the structure centre. Coating thickness, aperture diameter and slope angle were t=20 nm, d=30 nm and α=48.713°, respectively.

In optical recording, as in SNOM and photolithographic applications, the working distance is of the order of a few nanometres. A 2 nm working distance has been used in the heat-assisted magnetic recording technique reported by Seagate Technology PLC [116]. The 2D electric near-field on the x-y plane (the

grey plane in Figure 2-7 (a)) of 5 nm above the apex is showed in Figure 2-7 (b). The field is observed to be highly localized. The 3D image of the electric near-field distribution is also plotted using MATLAB (Figure 2-7 (c)). Finally, a cross section of the electric field intensity at y=0 is presented in Figure 2-7 (d); the FWHM which can be used to characterize the device spot size was calculated from this plot to be 44.7 nm, i.e. $\lambda/17$. Although the SP radial evanescent field could represent a limitation to field concentration, Figure 2-7 (d) shows that in this case its field strength is well below 30 % of the maximum. Because electric field intensity goes down further to ~0 for $|x|>$ 60 nm, the FWHM was calculated considering the baseline at 0. If we consider the baseline at 30%, the FWHM would be smaller (36 nm in Figure 2-7 (d)).

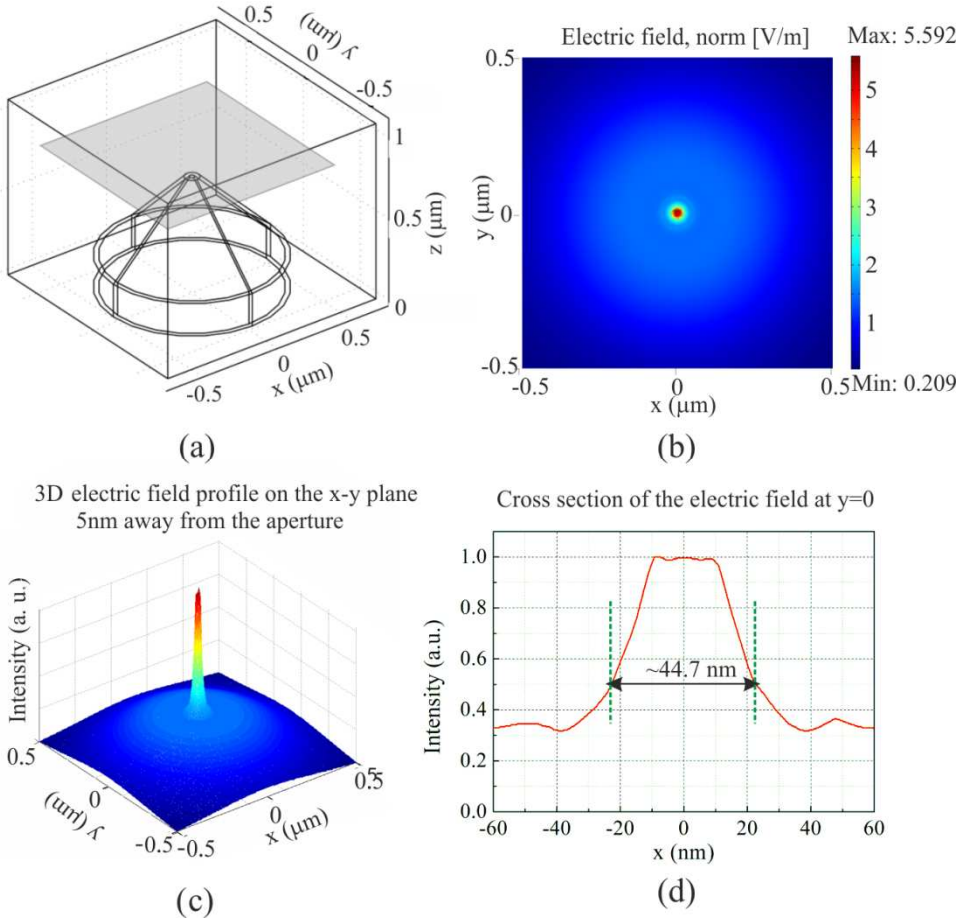

Figure 2-7 (a) Geometry of the modelled conical cut structure, in which grey plane represents the plotted plane in (b); (b) 2D electric near-field distribution at x-y plane 5 nm above the aperture for a tip with slope angle α=48.713° and d=30 nm aperture; (c) 3D electric near-field distribution at the x-y plane 5 nm above the aperture; (d) a cross section of the electric field intensity at y=0.

In order to identify whether a smaller spot size can be achieved with the designed structure, the modelling for a 5 nm aperture size was carried out.

The electric field in the same plane as shown in Figure 2-7 (a) is plotted in Figure 2-8 (a). Figure 2-8 (b) show that in this case the electric field is localized due to the aperture but a strong evanescent field can be observed for distances larger than 20 nm. Figure 2-8 (c) (cross section of the electric field at y=0) shows that the evanescent field outside the aperture is above 50%, thus will affect the efficient confinement.

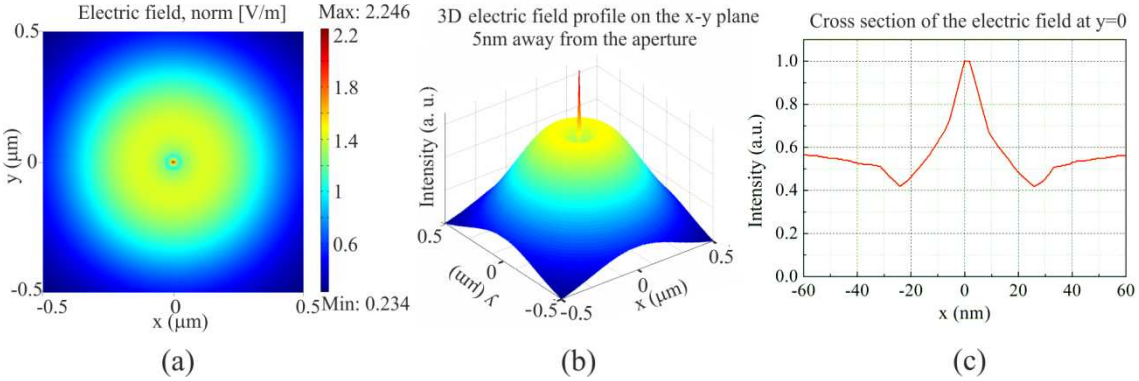

Figure 2-8 (a) 2D electric near-field distribution on an x-y plane 5 nm from the aperture for microfibre tip with α=48.713° and a d=5 nm aperture; (b) 3D electric near-field distribution on the x-y plane, 5 nm from the microfibre tip aperture; (c) a cross section of the electric field intensity at y=0.

The tip transmission efficiency in simulations was defined as the absolute value of the ratio between the Poynting vector integral at the input and output planes (only the section above the aperture), and is several orders of magnitude larger than what was observed in common SNOM tips [79].

Figure 2-9 shows the transmission efficiency variation dependence on the slope angle α for 30 nm and 5 nm aperture size, revealing that smaller slopes are associated with higher transmission efficiencies. High transmission efficiency is the result of two main factors. When the fibre tip diameter becomes smaller than a cut-off value (typically $\lambda/3$ in silica), no modal propagation occurs and only evanescent modes with a field decaying exponentially along the longitudinal direction (towards the aperture) exist. The longer the distance between the position of the cut-off diameter and the aperture, the smaller the transmission efficiency. On the other hand, when plasmons are excited at the interface with gold, the transmission efficiency can be improved. Figure 2-9 shows that this latter contribution is negligible, as SP

excitation is strongly angle dependent and no evident peaks have been observed at specific angles.

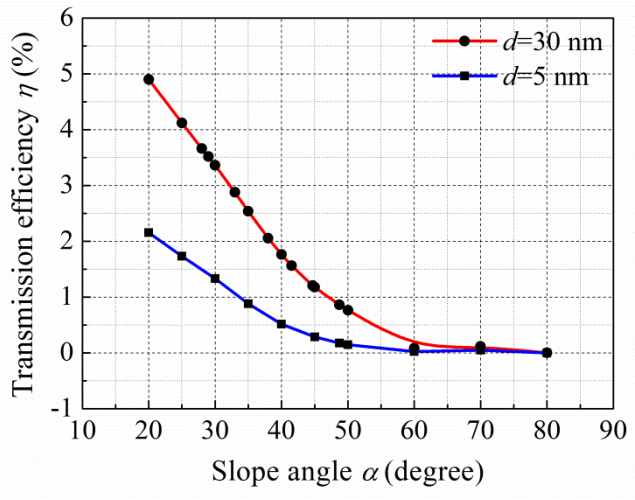

Figure 2-9 Transmission efficiency versus slope angle at λ=800 nm. Tip diameter is D=1 μm, coating thickness t=20 nm, aperture diameter is d=30 nm (red line with circle symbol) and d=5 nm (blue line with square symbol).

Electric field distributions at λ=800 nm across the x-z plane passing through the structure centre for slopes α=20°, 25°, 30°, 35°, 40°, 45°, 50°, 60°, 70°, and 80° are shown in Figure 2-10 for aperture size d=30 nm (Figure 2-10 (a)) and 5 nm (Figure 2-10 (b)). At α=20°, 25° and 30°, a negligible SP excitation was observed. As the slope angle increases, an increased field localization at the gold/dielectric interface is observed, with a maximum being reached at α=70°. Figure 2-9 shows that transmission efficiency decreases for increasing angles and at α=70° has an extremely small enhancement compared with α=60° and α=80°. Therefore, although SPs can be excited in the gold-coated fibre tip, their contribution to transmission efficiency can be considered negligible. Transmission efficiency is mainly dominated by the distance between the position of the cut-off diameter and the fibre tip aperture.

Figure 2-10 clearly shows that at small angles the contribution of the radial evanescent field is small, thus allowing for a better confinement. Figure 2-11 shows the simulations carried out assuming a coating thickness t=20 nm, an aperture diameter d=5 nm, and a slope angle of α=20°. In these conditions light is confined to 25 nm spot sizes with a relatively small intensity in the evanescent field. A FWHM of ~25.3 nm was observed (Figure 2-11 (c)) which can be decreased by further optimization.

(a) d=30 nm

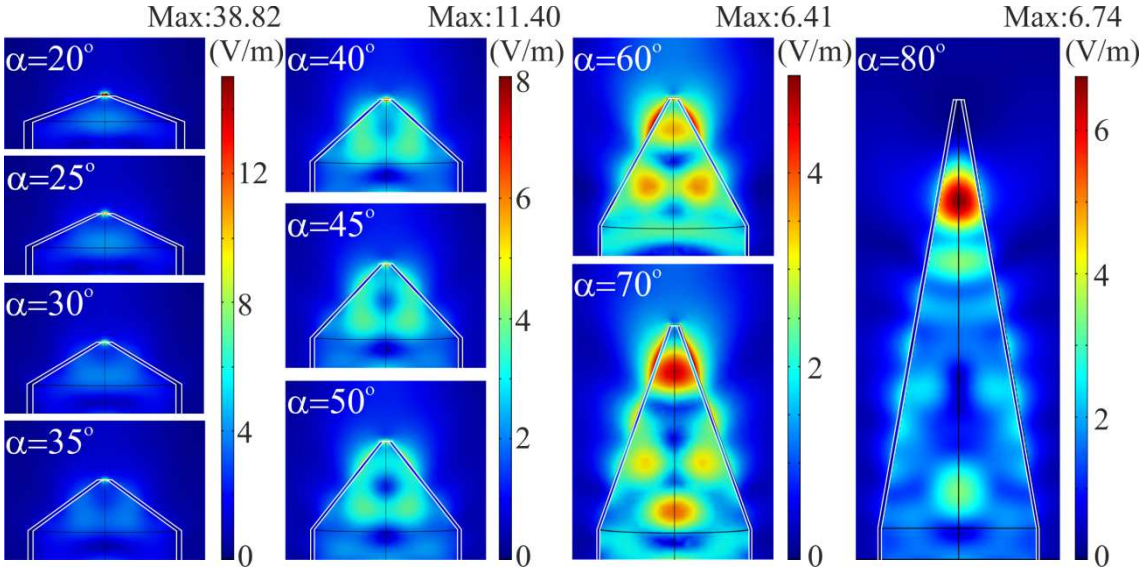

(b) d=5 nm

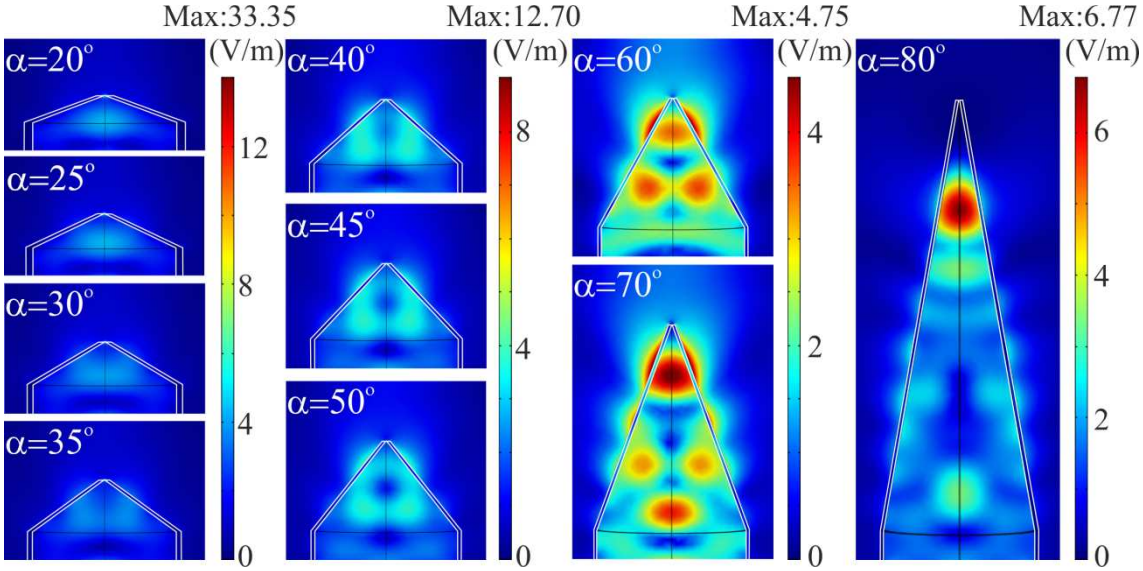

Figure 2-10 Electric field distribution at λ=800 nm across the x-z plane passing through the structure centre for slope angle α=20°, 25°, 30°, 35°, 40°, 45°, 50°, 60°, 70°, and 80°. Coating thickness and aperture diameters were t=20 nm and (a) d=30 nm, (b) d=5 nm respectively.

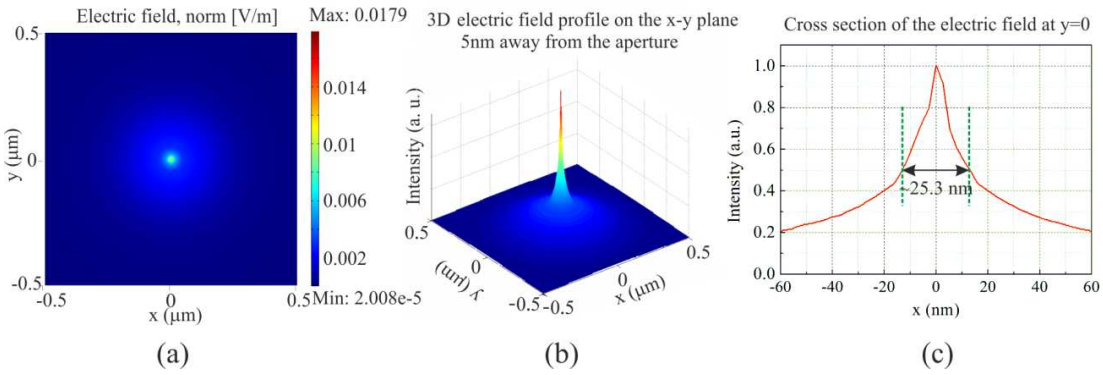

Figure 2-11 (a) 2D electric near-field distribution at *x*-*y* plane 5 nm above the aperture for 20° slope angle and 5 nm aperture size; (b) 3D electric near-field distribution at the *x*-*y* plane of 5 nm above the aperture; (c) a cross section of the electric field intensity at *y*=0.

The transmission efficiency dependence on aperture size is analysed in Figure 2-12, which clearly shows a decrease for decreasing aperture sizes. Although the spot size is determined by the aperture size, smaller aperture sizes are also associated with smaller transmission efficiencies. Yet, Figure 2-12 shows that efficiencies as high as 0.5% can be predicted even for apertures as small as 5 nm.

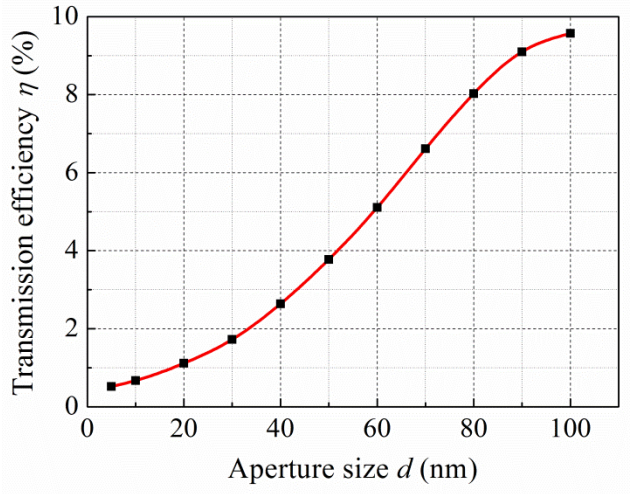

Figure 2-12 Transmission efficiency dependence on aperture size. Taper diameter, slope angle, coating thickness and wavelength are D=1 μm, α=40°, t=30 nm and λ=800 nm, respectively.

Other factors, e.g. metal materials, coating thickness and input light wavelength also play a role in the transmission efficiency and spot size. Figure 2-13 shows the simulations carried out to compare different metal materials at λ=800 nm. Trends in Figure 2-13 are primarily due to the dielectric constants which have greatest influence on the absorption loss. Silver shows the largest enhancement and widest angle tolerance because of its unique dielectric

constant. Gold also presents a relatively large enhancement compared with aluminium and platinum. However, silver is easily oxidized in air, whereas gold is much more stable. Thus, gold was chosen as the metal coating material in the experiments. Indeed, high powers tend to increase the tip temperature, facilitating surface oxidation, thus gold appears to be an excellent candidate for its relatively poor tendency to oxidize.

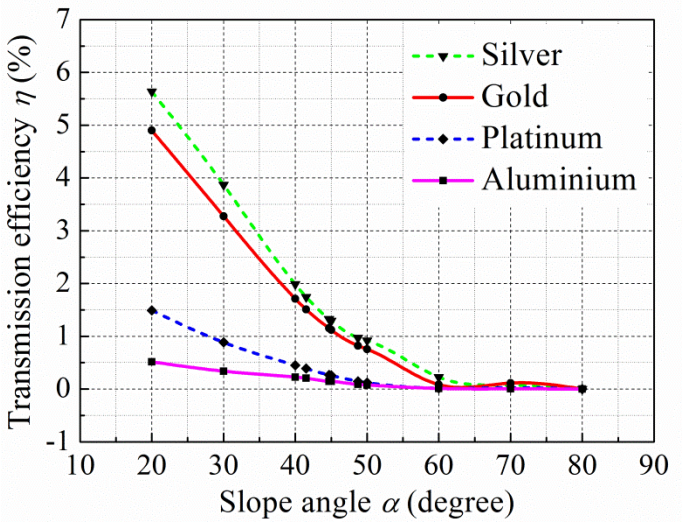

Figure 2-13 Transmission efficiency dependence on slope angle for four different coating metals: silver (green dash line), gold (red solid line), platinum (blue dash line) and aluminium (pink solid line). Tip diameter, aperture diameter, coating thickness and wavelength are D=1 μm, d=30 nm, t=20 nm and λ=800 nm, respectively.

Figure 2-14 shows the dependence of transmission efficiency on the coating thickness in the range 15 nm to 100 nm at 800 nm wavelength in simulations. The tip diameter, aperture size and slope angle are D=1 μm, d=30 nm, and α=40°, respectively. The maximum at t~30 nm allows for more fabrication tolerance and a reduction of charging issues during FIB milling. A possible explanation for the transmission efficiency decrease for t<30 nm is that at small gold coating thicknesses a considerable fraction of power lies in the radial evanescent field outside the gold coating and it is not included in the transmission efficiency calculation. This effect is also deleterious for the beam size, which is increased. As the longitudinal evanescent field overlaps with the gold coating, when the coating thickness increases above 30 nm, the overall absorption increases, thus transmission efficiency decreases. The thickness of t~30 nm has therefore been used in the experiments [117-119].

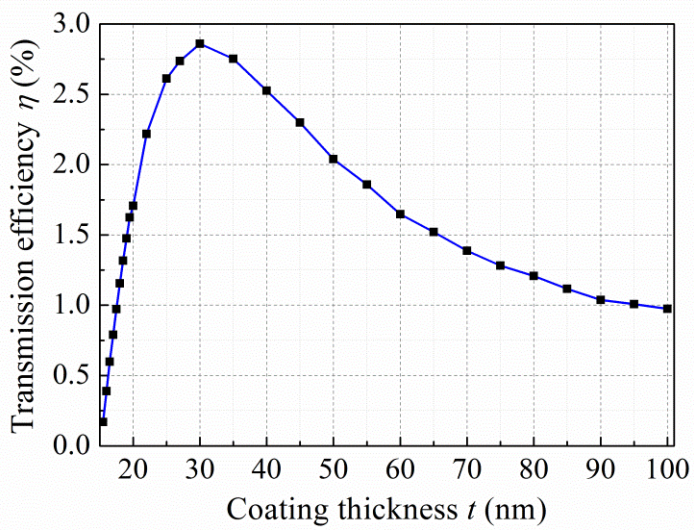

Figure 2-14 Fibre tip transmission efficiency versus gold coating thickness. The tip diameter, aperture diameter, slope angle and wavelength are D=1 μm, d=30 nm, α=40° and λ=800 nm.

Figure 2-15 presents the transmission efficiency dependence on the input wavelength when tip diameter, aperture diameter, slope angle and coating thickness are D=1 μm, d=30 nm, α=40° and t=30 nm, respectively. The influence of wavelength is rather complicated. Firstly, the dispersion of gold dielectric constant varies considerably with the wavelength [120]. Secondly, the cut-off diameter changes with the wavelength causing a change in the extent of its evanescent field.

It is known that when features become smaller than a certain limit the non-locality of the dielectric function should be taken into account [121]. According to ref. [122], for a metal-silica-metal waveguide, plasmon modes undergo a blue shift exceeding 10% at metal thicknesses below 5 Å because of the non-locality of the dielectric function and the blue shift decreases when the metal thickness increases. There is no obvious shift when the thickness is larger than ~6 nm. Since the gold thickness is chosen to be ~30 nm in the design, the non-local effect can be neglected. Moreover, the electromagnetic field enhancement between gold nanoparticle dimers is well approximated by the localised model above ~1 nm. Since the apertures considered in this work are never less than 5 nm, the field enhancement near the aperture is also well approximated by the localised model.

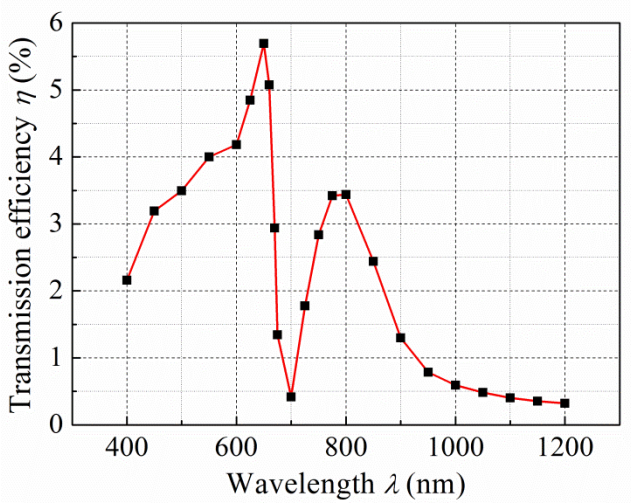

Figure 2-15 Transmission efficiency dependence on the wavelength. Tip diameter, aperture diameter, slope angle and coating thickness are D=1 μm, d=30 nm, α=40° and t=30 nm, respectively.

2.3 Device fabrication

Devices have been fabricated using the cleanroom facilities available at the Optoelectronics Research Centre (University of Southampton, U.K.). The fabrication process can be divided into four main steps: (i) manufacture of optical fibre tips, (ii) tip milling, (iii) gold layer deposition, and (iv) aperture opening at the coated fibre tip apex. Figure 2-16 shows the schematic diagram of the proposed device fabrication process.

Firstly, optical fibre tips were manufactured (Figure 2-16 (a)) using a commercial micropipette puller (P-2000) (SUTTER INSTRUMENT Inc., Novato, USA) which is a CO_2 laser based pulling machine controlled by a microprocessor. The specifications of P-2000 have been introduced in Section 1.1.1.2. Since high transmission efficiency is targeted in this work, the taper angle of the optical fibre tips has to be small enough to adiabatically convert the fundamental mode in the fibre core into a fundamental mode in the fibre taper [37]. Transmissions larger than 98% can be obtained in adiabatic fibre tapers [123]. CO_2 laser power, pulling speed, tension and delays were optimized to maximize the adiabaticity of the transition region between the optical fibre and fibre taper.

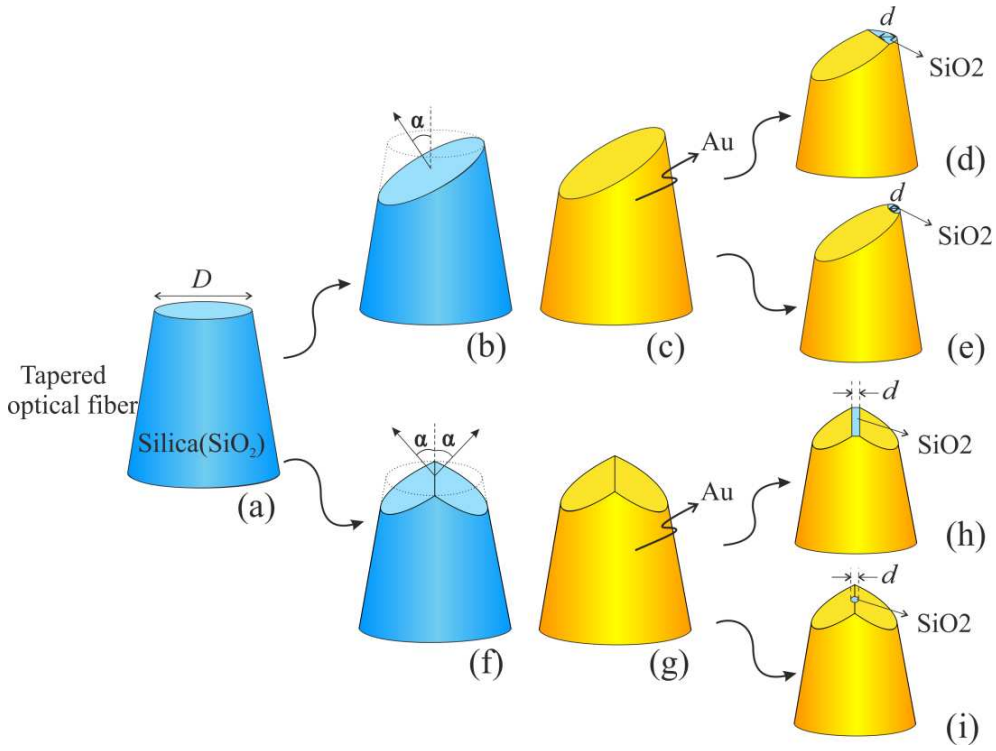

Figure 2-16 Schematic of the nanostructured fibre tip fabrication process. (a) Optical fibre tips are made using a P-2000 micropipette puller, *D* is the tip diameter; (b, f) the tips are cut at a slope angle *α* using FIB milling; (c, g) a thin layer of gold is deposited on the fabricated surface and (d, e, h, i) a small aperture with size *d* was opened at the apex.

Adiabatic fibre tips were then coated with a layer of gold (to avoid charging during FIB processing. Indeed, charge accumulation is a major issue and seriously degrades FIB imaging and processing capabilities) and nanostructured using a FIB milling system (Figure 2-16 (b) and (f)). As FIB is a direct writing technique with resolution smaller than 10 nm, it offers extreme flexibility and allows for high precision in the nanostructuring process. Figure 2-17 shows SEM images of the first two fabricated tips: (a) a single-ramp fibre tip and with a slope angle α=50.4° (b) a wedge fibre tip with a slope angle α=50°. The gold layer was removed by gold etching solvent after this step.

A <5 nm layer of chrome and 30 nm thin layer of gold was then deposited on the tips using a thermal evaporator with 2×10^{-6} mbar pressure, 2.4 mA current and 0.06 nm/s sputtering rate, to confine light and to avoid charging during processing.. Chrome was used to ensure a good gold adhesion to the silica tip even at high incident powers [91]. Although chrome can affect the SPs resonance [124], it is not detrimental in this work because SPs contribution is negligible. Finally, extremely small apertures were finally opened at the tips apexes (Figure 2-16 (d), (e), (h) and (i)).

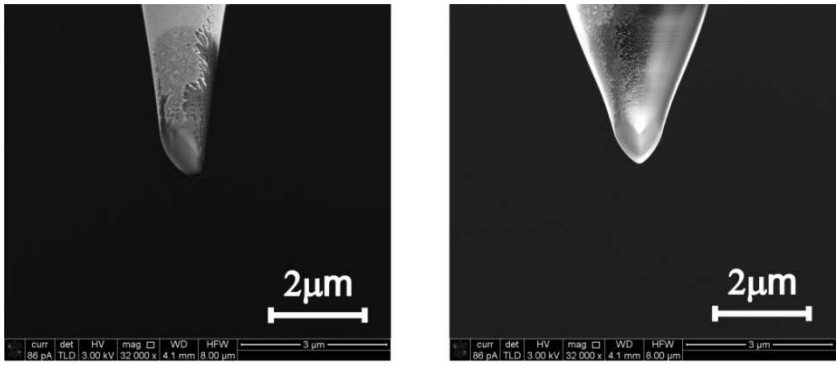

Figure 2-17 SEM images of the first two milled tips. (a) single-ramp and (b) wedge fibre tip.

Figure 2-18 shows the SEM images of some devices. Single-ramp tips have apertures made by flat cutting (Figure 2-18 (a) with *d*~66 nm) and hole drilling (Figure 2-18 (c) with size *d*~21 nm), respectively; apertures in the wedge tips are ~84 nm (Figure 2-18(b)) made by flat cutting and ~14 nm (Figure 2-18 (d)), ~13 nm (Figure 2-18 (e)) and ~21 nm (Figure 2-18 (f)) made by hole drilling. Because of the limited FIB stage travel in our fabrication facility, up to now it has been impossible to fabricate the conical fibre tip as simulated in theoretical analysis.

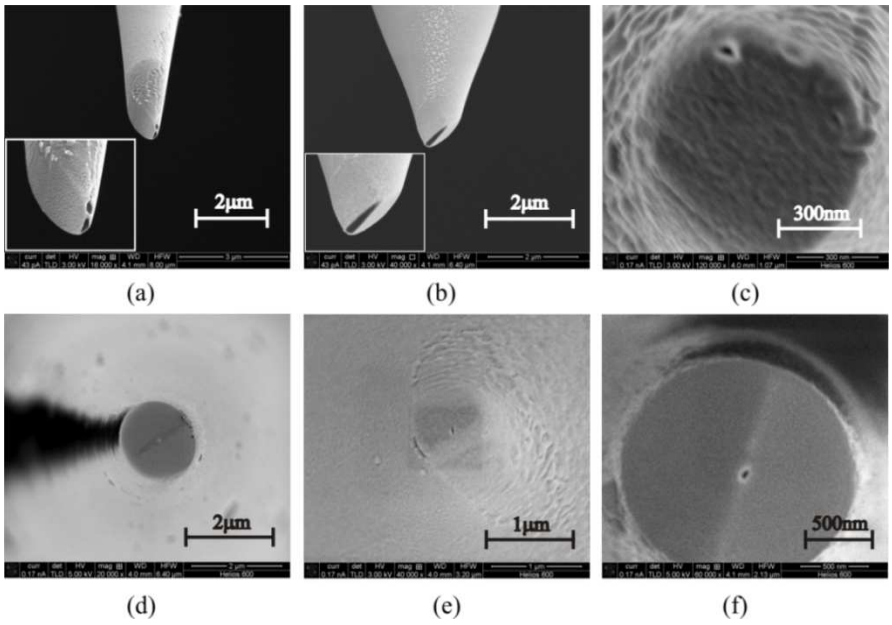

Figure 2-18 SEM images of fibre tips with nanometre apertures. Tips were cut at slope angle α and apertures (dark regions) were opened at the apexes of gold-coated tips. (a) single-ramp fibre tip with flat cut aperture size~ 66.4 nm; (b) wedge fibre tip with slit aperture size ~84 nm; (c) single-ramp fibre tip with a hole size ~21 nm; wedge fibre tips with a hole size (d) ~14 nm, (e) ~13 nm and (f) ~21 nm. Insets on (a) and (b) are magnification of the aperture regions.

2.4 Characterization

Figure 2-19 shows the characterization set-up. Device transmission efficiency was characterized using a *Supercontinuum* (SC) source (FIANIUM Inc., Southampton, UK) delivering 6 W of 400 fs, 50 nJ pulses over a very broad range of wavelengths from 450 nm to 1800 nm to inject light into the samples under test. The SC output fibre pigtail was angle cleaved to avoid back reflection, thus damage to the source. A modal filter was inserted to minimize the fraction of power in high order modes [123]. Light was then launched into the sample and finally collected using a multimodal pigtail connected to an *Optical Spectrum Analyser* (OSA) (AQ6317, Yokogawa, Japan). XYZ stages were used to align the different fibre components.

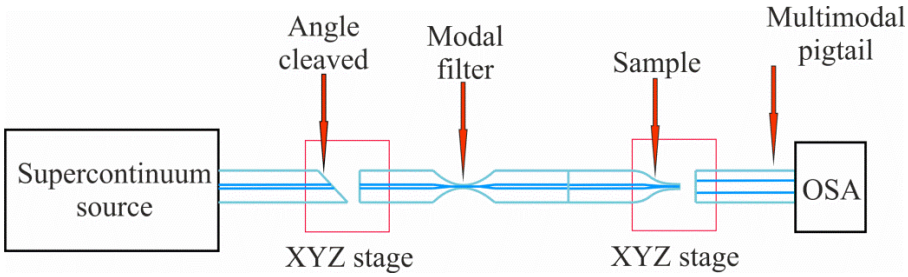

Figure 2-19 Schematic of the set-up to characterize the samples.

Preliminary measurements were carried out without any sample to provide a normalization base for the following spectra and to remove any wavelength dependence related to the source and to the modal filter. Sample spectral measurements were then carried out.

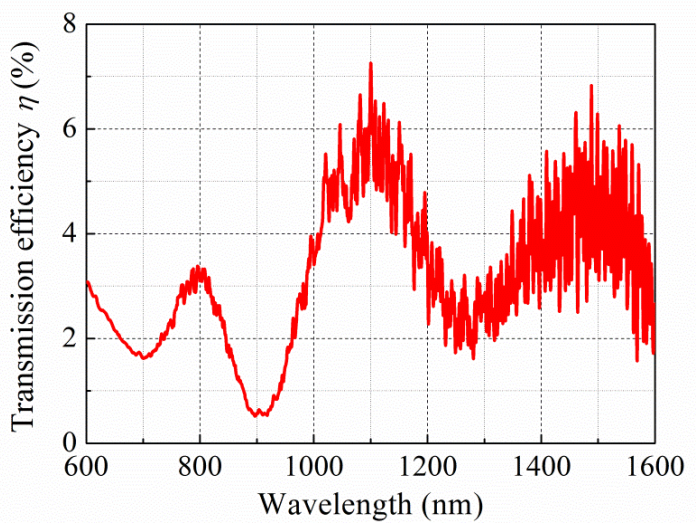

Figure 2-20 Transmission efficiency of the single-ramp fibre tip A in Figure 2-18 (a).

Tips A and B in this characterization are shown in Figure 2-18 (a) and (b). Measurement results for the single-ramp sample A transmission efficiency are summarized in Figure 2-20. Three peaks at about 800 nm, 1100 nm and 1500 nm were observed. They could originate from the presence of different cleaving angles in the tip due to the imprecision in the FIB and/or multiple modes in the fibre taper. The small periodicity noise is probably due to the interference generated at air gaps between the various optical components. The transmission efficiency of sample A is ~10^{-2} and several orders of magnitude larger than that observed in common SNOM tips (10^{-4}~10^{-5}). The spot size of this sample along the smaller axis is as large as ~λ/15. Powers close to 1 W were injected in the tip without any apparent damage. It is interesting to note that fibre tips which exploited SPs for focusing could not stand powers of 0.1 W, as the strong field at the metal/air surface probably damaged the fibre tip surface.

Figure 2-21 shows the normalized transmission of sample B, which reaches ~3% transmission efficiency at λ~750 nm: the wavelength dependence clearly resembles that predicted by simulations of Figure 2-15. As for the results presented in Figure 2-20, the small periodicity noise in this graph could be due to the interference generated by air gaps between the various optical components again. The spot size along the smaller axis of this sample is approximately λ/10.

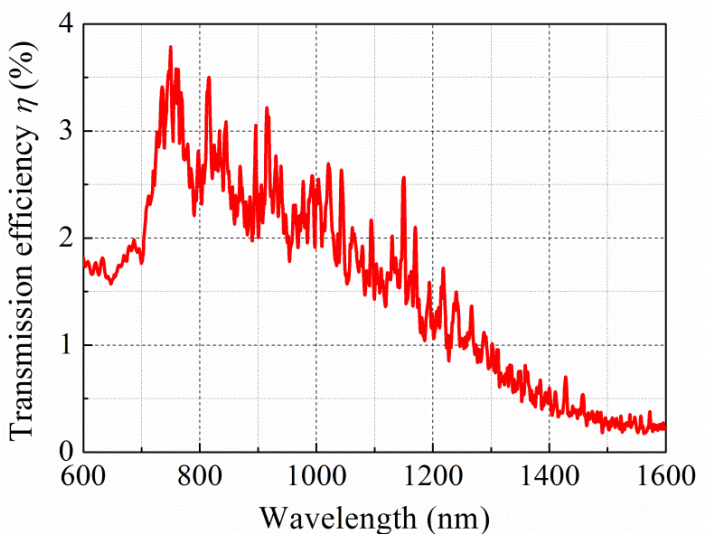

Figure 2-21 Transmission efficiency of the wedge fibre tip of Figure 2-18 (b).

The transmission efficiency measured in the experiments is of the same order of magnitude of (indeed a little lower than) those predicted by simulations. The mismatch is probably due to the presence of additional modes in the fibre tip, to surface/coating nonuniformities, the shape of nanostructured tip difference and to the different polarization used in the simulations and in the experiments. In addition, since we used a multimode fibre to collect the light, the measurement cannot discriminate between the light in the hot spot and "unfocused" light around it.

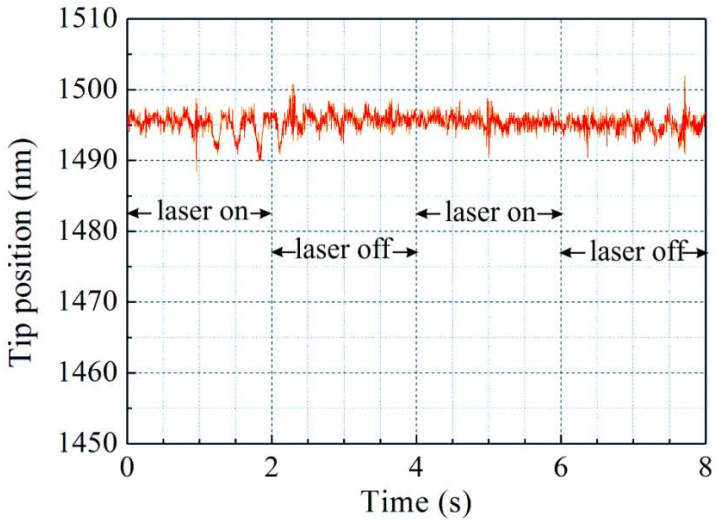

Figure 2-22 Tip position as a function of time. The laser (9 mW) was switched on and off every ~2 s. (The data was collected by Dr. Oliver Fenwick at UCL)

Since the metal-coated fibre tips may undergo thermal expansion due to the energy absorption by the metal when high laser powers are injected into them, their transmission efficiency (and reliability) can be affected. The study of the tips thermal expansion was carried out using a homemade SNOM following a method reported previously [89] in University College London (London, UK) [125]. A He-Cd laser with λ=325 nm and power of 9 mW was launched into the fibre tip C shown in Figure 2-18 (f) made from a pure silica fibre (OZ QSMF-320-2/125-0.25-L). The tip, which had been mounted on a tuning fork, was held in close contact with the surface of a bare glass surface using shear force feedback. If, due to absorption, the tip heats up, its length varies by an amount Δh_{tip}, and the feedback responds by adjusting the sample position by an equivalent amount. Thus the sample position was followed as a function of the time and used as a measure of Δh_{tip} whilst using a shutter to switch the laser power on and off with a ~2 s period (Figure 2-22). The

thermomechanical response of the tip can thus be measured by monitoring the error voltage provided by the feedback circuit. From the data, no discernible variation in Δh_{tip} related to the laser power could be detected within the accuracy of the system (~2 nm). This result is remarkable when comparing to measurements made on other fibre probes where Δh_{tip} of up to hundreds of nanometres have been measured for similar injected laser powers, but confirms the good mechanical stability of our tips.

2.5 Conclusions

In this chapter, preliminary studies on the efficient sub-wavelength light confinement of high optical powers in apertured optical fibre tips were presented. Theoretical simulations were carried out to predict optima, which could provide a reference for the fabrication of devices suitable for data recording (like AOMR), photolithography and imaging. Devices were manufactured using a P-2000 micropipette-puller, an evaporator, and a FIB system. Device transmission spectra were measured with a SC source and transmission efficiencies of the order of few percent were recorded. Fibre tips could survive powers as large as 1 W and thermal expansion measurements showed no shape change could be detected within the accuracy of the SNOM system (~2 nm) for 9 mW injected powers. Future optimizations will require the use of conical tips and near-field measurement to characterize the spot size. Effective confinements to 10 nm or smaller can be envisaged by decreasing the aperture size and slope angle. Application of this small spot size source can include SNOM, optical recording, photolithography and bio-sensing.

Chapter 3 Three dimensional light confinement with optical microfibre grating

> Now I just work as hard as I can and left the rest fall where it may. It still doesn't feel great most of the time, but I push through it, for the sake of so much good.
>
> Andre K. Agassi

Fibre Bragg Gratings (FBGs) have played an important role in optical communication. Based on FBG, fibre *Distributed Feedback* (DFB) lasers and *Phase-Shifted Bragg Gratings* (PSBGs) also have attracted many researchers' attention due to their narrowband band-pass features. Several technologies were used to fabricate gratings [126-132], e.g. bulk interference [133], phase mask interference [134-136] and point by point writing [137]. However, these methods either rely on expensive phase masks or high precision alignment to induce a very small refractive index change. *Focused Ion Beam* (FIB) technology brings the possibility to modify the refractive index of fibres with high modulation and can directly write in optical fibres.

M. Ding, M. N. Zervas, and G. Brambilla, "A compact broadband microfibre Bragg grating," *Opt. Express* **19**, 15621-15626 (2011).

M. Ding, P. Wang, T. Lee, and G. Brambilla, "A microfibre cavity with minimal-volume confinement," *Appl. Phys. Lett.* **99**, 051105 (2011).

In this chapter, 3D confinement is proposed using a microcavity in a *Microfibre Phase-Shifted Bragg Grating* (MPSBG). This structure can provide axial confinement by the large contrast (air-dielectric) index guiding and longitudinal cavity confinement by the phase shift in the centre of the MPSBG. If a high refractive index material is used, high reflection can be obtained even with only a few periods.

In the next sections, an introduction to Bragg gratings and microcavities is presented firstly. The *Microfibre Bragg Grating* (MFBG) is then discussed in both experiments and simulation. Based on MFBG, the fabrication and characterization of MPSBG are introduced. Simulations are carried out to verify the experimental results.

3.1 Background

3.1.1 Fibre grating theory

3.1.1.1 Fibre Bragg grating (FBG)

A FBG is a periodic or aperiodic perturbation of the effective refractive index in the core of an optical fibre [138]. Typically, the perturbation is approximately periodic over a certain length of e.g. a few millimetres or centimetres, and the period is of the order of the optical wavelength. The modulation is most commonly achieved by variation of the refractive index. At each change of refractive index a reflection of the propagation light occurs. The repeated modulation of the refractive index results in multiple reflections of the forward travelling light. The period of index modulation relative to the wavelength of the light determines the relative phase of all the reflected signals. At a particular wavelength, known as the Bragg wavelength, all reflected signals are in phase and add constructively and a back reflected signal centred at the Bragg wavelength is observed. Reflected contributions from light at other wavelengths do not add constructively and are cancelled out and, as a result, these wavelengths are transmitted through the grating. Figure 3-1 shows the schematic of a FBG.

Although a FBG in single mode, step index optical fibre is not an identical structure manufactured in microfibres, it still allows for the key principles to be understood.

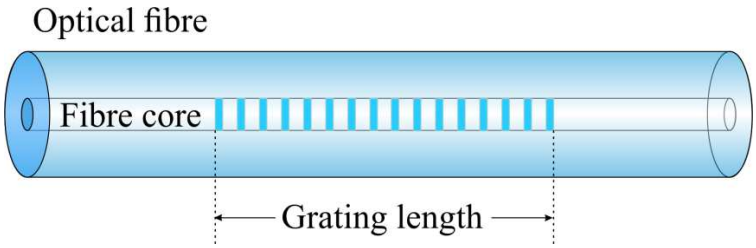

Figure 3-1 Schematic of a FBG. The blue bars in the fibre core indicate the refractive index modulation.

Using the principles of energy and momentum conservation, the central wavelength reflected by a FBG can be determined. For energy to be conserved there can be no change in frequency as a result of reflections at grating planes. For conservation of momentum the sum of the incident wave vector $\vec{k}_i$ and the grating wave vector $\vec{K}$ must equal the wave vector of the reflected wave $\vec{k}_r$:

$$\vec{k}_i + \vec{K} = \vec{k}_r \tag{3-1}$$

When the Bragg condition is satisfied $\vec{k}_r = -\vec{k}_i$ and Equation (3-1) can be written as following if the modulus of wave vector is considered:

$$\frac{2\pi}{\lambda_B} n_{eff} - \frac{2N\pi}{\Lambda} = -\frac{2\pi}{\lambda_B} n_{eff} \tag{3-2}$$

Solving above equation can get the Bragg wavelength:

$$N \cdot \lambda_B = 2 n_{eff} \Lambda \tag{3-3}$$

where N is an integer that signifies the harmonic order, λ_B is the Bragg wavelength, Λ is the grating period and n_{eff} is the effective refractive index of mode in the fibre.

The first permanent FBG was demonstrated by K. O. Hill et al. in 1978 using an argon ion laser [139, 140]. After that, several technologies were used to inscribe FBGs [138], e.g. bulk interference [133], phase mask interference [134-136] and point by point writing [137]. Laser induced gratings rely on the fibre photosensitivity to induce a very small refractive index modulations (typically $\Delta n \sim 10^{-4}$-10^{-3}). The inscription of relatively long uniform Bragg gratings with

small Δn resulted in a bandwidth of the order of 1 nm or smaller. In recent years *Femtosecond* (*fs*) lasers [141, 142] have been used to write gratings in a range of materials which include also pure silica and ZBLAN glasses (a heavy metal fluoride glasses with a composition ZrF_4-BaF_2-LaF_3-AlF_3-NaF), previously considered insufficiently photosensitive for other lasers. Indeed, *fs* lasers have also been used to ablate the surface of microfibres [143] and exploit the periodic surface damage to write long period gratings; the large refractive index contrast (Δn ~0.45) between silica and air resulted in a long period grating length of ~150 μm.

3.1.1.2 Fibre Phase-Shifted Bragg Grating (PSBG)

A FBG behaves like a band-stop filter because the Bragg wavelength is reflected in such a grating. However, in many applications, selecting a channel is important rather than rejecting it from a broad band spectrum. The fibre phase-shifted Bragg grating is the simplest band-pass filter and introduces a phase-step within the grating. This is effectively a *Fabry-Perot* (F-P) filter with a gap smaller than one Bragg wavelength which induces the phase step. The position and the size of the gap determine the position and the wavelength of the transmission band. A schematic of a PSBG is shown in Figure 3-2. The phase-shifted Bragg grating structure can be used in semiconductor and fibre lasers to enable single frequency operation; these lasers are then called DFB lasers. The application of fibre phase-shifted Bragg grating requires low loss, broad bandwidth and a high-finesse filter. With fabrication technologies available today, it is possible to fabricate transmission filters of less than 1Å linewidth at λ=1.5μm.

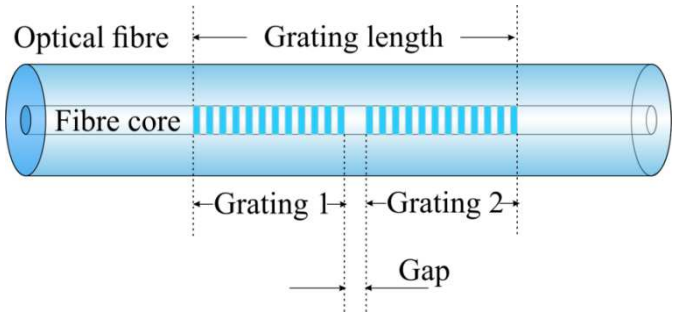

Figure 3-2 Schematic of a PSBG. The blue bars in the fibre core indicate the refractive index modulation.

The PSBG can be analysed by using the coupled mode theory [138]. The matrix method provides a simple way to get the transfer function of the PSBG. A transfer matrix represents the grating amplitude and phase response. The transfer matrix of the PSBG is:

$$T_{PSBG} = T^2 T^{ps} T^1 \tag{3-4}$$

in which T^1 and T^2 are the transfer matrix of grating 1 and 2, T^{ps} is the phase shift matrix:

$$T^{ps} = \begin{bmatrix} e^{-i(\phi/2)} & 0 \\ 0 & e^{+i(\phi/2)} \end{bmatrix} \tag{3-5}$$

where Φ is the phase factor.

Then, the PSBG transfer function T_{PSBG} is:

$$T_{PSBG} = \begin{bmatrix} T_{11}^2 T_{11}^1 T_{11}^{ps} + T_{12}^2 T_{21}^1 T_{22}^{ps} & T_{11}^2 T_{11}^1 T_{11}^{ps} + T_{12}^2 T_{22}^1 T_{22}^{ps} \\ T_{21}^2 T_{11}^1 T_{11}^{ps} + T_{22}^2 T_{21}^1 T_{22}^{ps} & T_{21}^2 T_{12}^1 T_{11}^{ps} + T_{22}^2 T_{22}^1 T_{22}^{ps} \end{bmatrix} == \begin{bmatrix} T_{11}^{PSBG} & T_{12}^{PSBG} \\ T_{21}^{PSBG} & T_{22}^{PSBG} \end{bmatrix} \tag{3-6}$$

The transmissivity of the whole grating is:

$$\left|\tau^{PSBG}\right| = \left|\frac{1}{T_{11}^{PSBG}}\right|^2 = \frac{1}{T_{11}^{PSBG}(T_{11}^{PSBG})^*} = \left|\frac{1}{T_{11}^2 T_{11}^1 T_{11}^{ps} + T_{12}^2 T_{21}^1 T_{22}^{ps}}\right|^2 \tag{3-7}$$

and the reflectivity:

$$\left|\rho^{PSBG}\right|^2 = 1 - \left|\tau^{PSBG}\right|^2 \tag{3-8}$$

In general, both grating sections need not be placed symmetrically around the phase step and the gratings may have different bandwidths and refractive index modulation amplitudes. However, the simple band-pass filter has, in the centre of a FBG, a phase-step, which has the effect of introducing a single pass-band in the transmission spectrum. In this case, $T_{21}^1 = (T_{12}^2)^*$, and $T_{11}^1 = T_{11}^2$. Figure 3-3 shows the band-pass spectrum of a 3 mm long grating with a quarter-wavelength ($\lambda/4$) step in the centre. The amplitude of the refractive index modulation is 5×10^{-4}. Notice that although there is a very narrow transmission band in the centre of the grating spectrum within a band stop of ~1 nm, there are strong side lobes on either side. The band-pass is a highly selective filter within a relatively narrow band stop. A FBG of the same length but without the phase step has a bandwidth approximately half that of the full band stop of the

PSBG grating. The phase-shifted Bragg grating may be viewed as being composed of two single gratings, each half the length of a uniform one.

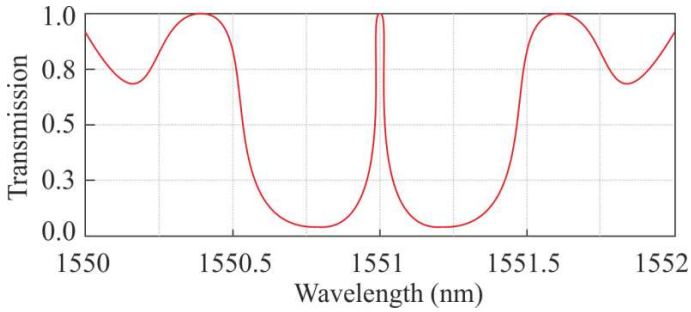

Figure 3-3 The calculated transmission spectrum of a 3 mm long PSBG gratings, with a $\lambda/4$ phase step in the centre and a refractive index modulation 5×10^{-4}.

The phase mask allows the replication of PSBG structures into fibres in a simple and controlled manner. This has been done successfully to produce a variety of band-pass PSBG structures [144].

3.1.2 *Optical microcavities*

In recent years, resonators based on optical microcavities have attracted increasing attention [47] because of their wide range of applications. These objects can confine light in a small volume by resonant recirculation and have been demonstrated in several structures [47]. Whispering gallery modes obtained extreme light confinement within volumes of ~10^3-10^5 μm^3 and have been observed in several geometries including microtoroid [145], microsphere [146], and microdisk [147] resonators. Microcavities based on photonic crystals can also provide extremely small mode volumes (<1 μm^3) [148]: the microcavity is formed by dry etching a hexagonal array of holes and subsequent selective etch of an interior region. One hole is left unetched allowing for the creation of an optical microcavity where a half wavelength thick waveguide allows for vertical confinement, while a photonic crystal mirror provides a 2D lateral localization.

Another type of resonator uses F-P cavities manufactured in a quantum-dot-loaded micropillar [149]: in this device, Bragg mirrors provide longitudinal confinement, whereas air-dielectric guiding provides radial confinement. F-P microcavities have also been demonstrated in optical fibres [150], but with

volumes in the order of 10^3-10^4 mm^3 because of the small refractive index contrast (10^{-3}) in the grating fringes and at the core/cladding interface.

In the next sections, the possibility to inscribe a MFBG by nanostructuring a microfibre with FIB milling is demonstrated. FIB milling allows for extreme flexibility in the grating design, as it is a direct writing technique. The size and the shape of individual grating elements can be controlled over a wide range of values in a straightforward manner. In addition to the Bragg wavelength this results in the control of the out-of-plane scattering and radiation losses. Twenty specially shaped notches were carved in the microfibre and thus achieved a Δn~0.446 (difference between silica refractive index n_{silica}~1.446 and air refractive index n_{air}~1) at the wavelength λ=1.4 μm allowing for a grating length smaller than 10 μm which is the shortest FBG to our knowledge. Based on it, a microcavity in microfibre Bragg grating is proposed for 3D light confinement.

In optical fibres the small refractive index difference in the grating pitches implies that thousands of periods are needed to provide strong reflectivity; on the contrary, in nanostructured microfibres the large refractive index contrast between taper and air will require only dozens of periods to achieve a strong grating. Calculation shows that only ~70 periods are needed to obtain 99% reflectivity. Although it is theoretically possible to carve these high contrast gratings in optical fibres, this process would require an extremely long time because of the large amounts of material to be removed. In addition, if a fibre with a high refractive index core [137] was used to make the taper, the number of grating periods can be decreased even further: by using the large refractive index contrast at the interface between the taper material and air, gratings can be manufactured even with only few periods.

3.2 Microfibre Bragg grating (MFBG)

3.2.1 Working principle and fabrication

Figure 3-4 represents a schematic of MFBG, which is composed of dozens of grooves inscribed in the uniform waist region of a microfibre connected by two conical transition regions to conventional optical fibres. The diameter of the

uniform waist region was chosen to be D~1μm, thus the microfibre operated in single mode regime above λ~1.36 μm.

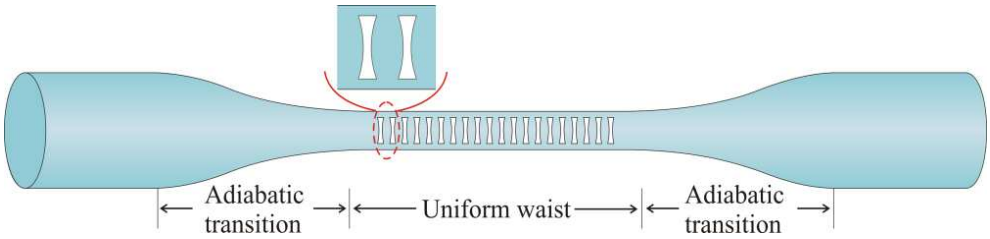

Figure 3-4 Schematic of MFBG. The insert shows a schematic of the biconcave shape of curved air notches.

When a microfibre is periodically machined, air cavities which is milled all the way through the fibre are formed; by exploiting the refractive index difference between silica and air, Δn as high as ~0.446 at λ=1.4 μm can be achieved. At each silica/air interface a fraction of the propagating light is reflected and the repeated refractive index modulations result in multiple reflections of the forward and backscattered travelling components which interfere to give transmission and reflection spectra. At the Bragg wavelength, all reflected signals are in phase and add constructively. Reflected contributions from light at other wavelengths do not add constructively and are cancelled out; as a result these wavelengths are transmitted through the grating. Due to the high refractive index contrast between silica and air, reflection is strong at each interface. Inevitably, such large refractive index changes result in relatively strong radiation-mode excitation and losses. In order to decrease the radiation loss, the air cavities can be designed with a biconcave geometry (shown schematically in Figure 3-4). This effectively results in a periodic series of small biconvex lens-like structures that better confine the light and reduce radiation losses.

In this study, a standard telecom optical fibre (Corning SMF-28) was used to fabricate the microfibre. The low loss microfibre was manufactured by the well-established microheater brushing technique (Section 1.1.1.2). The profile of the conical transition tapers in the experiment was approximated by a decreasing exponential function (transition region length ~25 mm, uniform waist length ~4 mm, relative taper elongation rate=0 [151]) and was achieved by ensuring appropriate control of the translation stage movement during the

tapering process [2, 151]. The microfibre diameter was D~1.34 μm and allowed single mode propagation at λ>~1.8 μm and multimode operation at shorter wavelengths. The microfibre was packaged on an aluminium slide which was coated by a layer of Efiron PC-373 (Luvantix, Ansan-si, Korea), having a cured refractive index of n~1.373@1550 nm, to avoid additional optical losses. To increase device sturdiness, part of the microfibre was embedded in the low refractive index polymer and the microfibre pigtails were fixed to the slide using two small drops of UV curable polymer (UV375, also from Luvantix). A 100 nm layer of gold was deposited on the taper surface by an electron beam evaporator to avoid charging during FIB milling as this can cause large fabrication errors. The grating period was chosen to be Λ~506 nm to obtain the first order Bragg reflection at λ_B~1360 nm since the effective index of the fundamental mode n_{eff}~1.34. In order to optimize the length ratio of the air and silica, simple calculations used an infinite periodic multilayer stack with the same refractive index profile as the microfibre Bragg grating. The reflectivity resulted to have a maximum for notch lengths of the order of 210 nm-310 nm. The FEI "Helios 600" FIB system was used to etch the cavities with a gallium ion beam characterized by a 30.0 kV accelerating voltage and 93 pA current. Biconcave air cavities 287.5 nm long × 850 nm wide were centrally and precisely carved-out along the waist of the microfibre. Features with less than 30 nm width can be easily achieved with this specific ion beam.

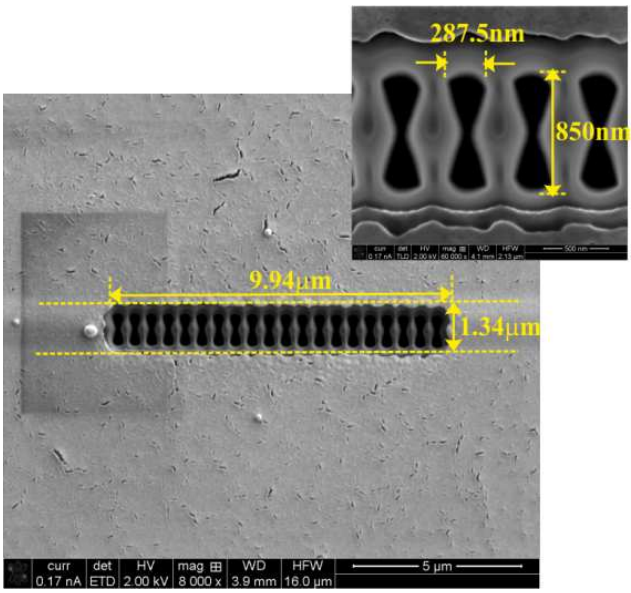

Figure 3-5 SEM image of a MFBG partly embedded in the polymer and coated with a gold layer. Yellow dashed lines indicate the microfibre edge, which is not clear because the microfibre was packaged and coated. The insert shows the details of the biconcave air notches.

Figure 3-5 shows the SEM image of the gold-coated MFBG with 20 periods. The total length of the MFBG is 9.4 μm, which is extremely short compared with conventional FBGs (a few millimetres or centimetres). Gold was subsequently removed using commercial gold etchant which contains iodine and potassium iodine after FIB milling.

3.2.2 Optical reflection properties of microfibre Bragg grating

The Microfibre Bragg grating reflection properties were characterized using the set-up shown in Figure 3-6. A *Supercontinuum* (SC) source is the same as used in earlier experiments of Section 2.4. Light from the SC source was launched into a bi-conical 2×2 microfibre coupler with an extremely wide, single mode operation bandwidth (400 nm-1700 nm) [152]. This coupler is specifically designed to suppress any higher order mode content present at the input fibre whilst at the same time providing efficient power splitting into the fundamental mode equally at the two output ports. One of the output ports was connected to the MFBG. Light reflected by the grating passed through the coupler and was recorded by an OSA which is also the same used in Section 2.4. XYZ stages were used to align the different fibre components.

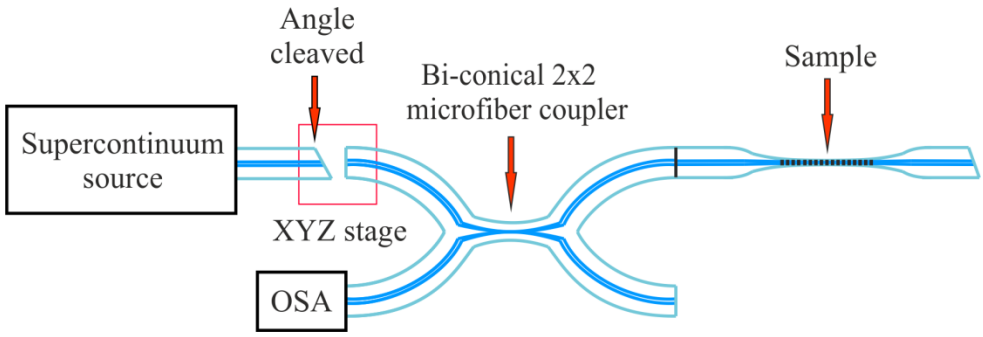

Figure 3-6 Schematic of experimental set-up used to characterize the MFBG.

The spectral response of the coupler output was first recorded without any sample to provide a normalization base line for the following spectra and to remove any wavelength dependence related to the source and to the coupler. Then, the sample reflection spectrum was recorded.

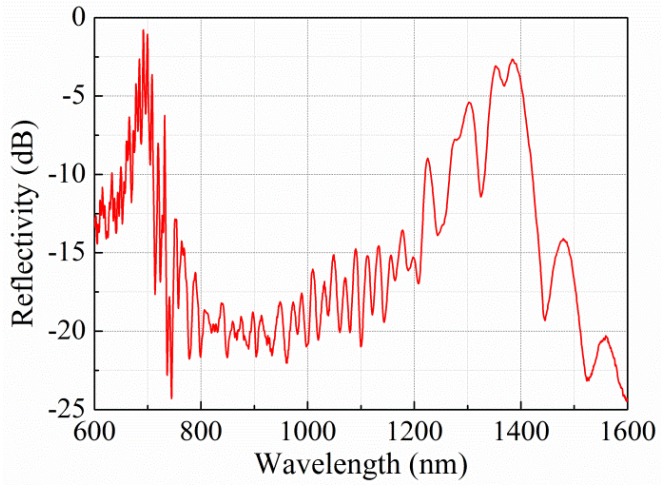

Figure 3-7 MFBG reflection spectrum. The grating has 20 periods with pitch Λ~506 nm.

Figure 3-7 shows the normalised MFBG reflection spectrum. There are two peaks in this spectrum. The peak at λ~1360 nm corresponds to the first order Bragg reflection for the fundamental mode, while that at λ~680 nm comes from the second order Bragg reflection. The width of the fundamental mode peak is ~75 nm, considerably broader than that observed in uniform FBGs (~1 nm) written in conventional fibres. Strong reflection (-3 dB corresponds to 50% reflection) was observed with only 20 periods in the MFBG. The possible explanation of spectrum noise might be the side-lobes in the grating or interfence from the air gap between different optical components. The reflectivity response (amplitude and width of the Bragg peak) can be further improved by optimizing a number of physical parameters for the MFBG, such as the grating period number, their shape and the microfibre material.

3.2.3 *Modelling of microfibre Bragg grating*

To verify the experimental results, a 3D finite element method was used to numerically solve Maxwell equations in the frequency domain and get the electric field and reflectivity of the MFBG. The numerical model was defined, solved and analysed using COMSOL 4.1 Multiphysics. The modelling geometry is presented in Figure 3-8 and it has the same geometry as the Microfibre Bragg grating shown in the SEM image of Figure 3-5. The highlighted lines in the inset of Figure 3-8 show the biconcave air notch profile. The MFBG is surrounded by polymer which has a refractive index n~1.373. In order to decrease calculation complexity and time, symmetry was used to reduce the geometry to half a cylinder. The chosen boundary conditions were: perfect

electric conductor (flat surface at the top in Figure 3-8) at the symmetry planes, scattering boundary condition at the cylinder outer surfaces and port boundary at the input and output surfaces (the definition of boundary conditions are introduced in Appendix A). Simulations were run with a controlled mesh size (150 nm in silica, 250 nm in polymer and 75 nm in air notches) to make efficient use of computer memory. A single mode was launched into the MFBG from the input port.

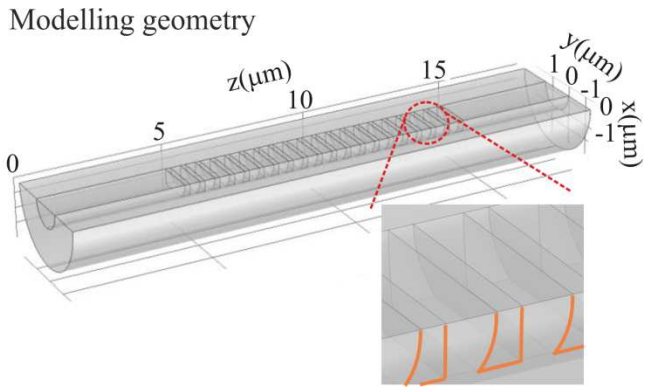

Figure 3-8 Schematic of the MFBG modelling. Inset: magnification of the biconcave air notch region; highlighted orange lines represent interfaces between silica and air.

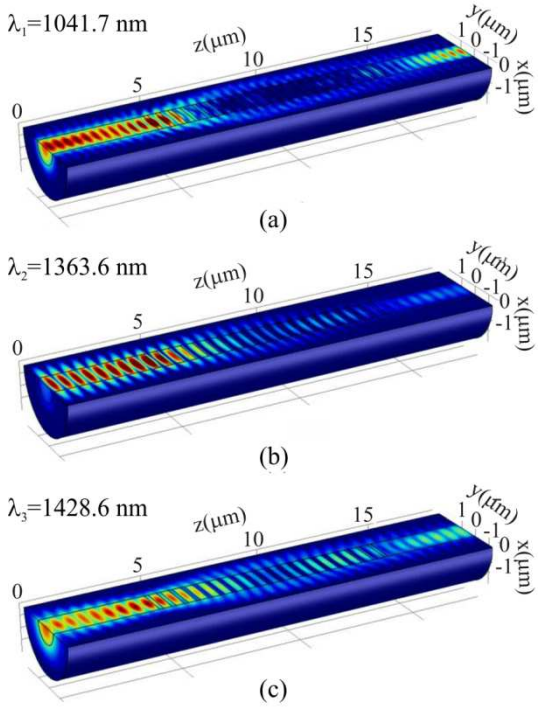

Figure 3-9 Electric field distributions at wavelength (a) λ_1=1041.7nm, (b) λ_2=1363.6nm and (c) λ_3=1428.6nm respectively.

Figure 3-9 (a-c) (corresponding to the wavelengths λ_1, λ_2 and λ_3 in Figure 3-10) show the electric field of the grating at the Bragg wavelength and at wavelengths far from the Bragg condition. The field distribution in Figure 3-9 (b) confirms that the reflection peak around the 1364 nm indeed corresponds to the main Bragg wavelength; on the contrary, far from the Bragg wavelength, at the minimum reflection points as shown in Figure 3-9 (a) and (c), almost all the light passes through the grating.

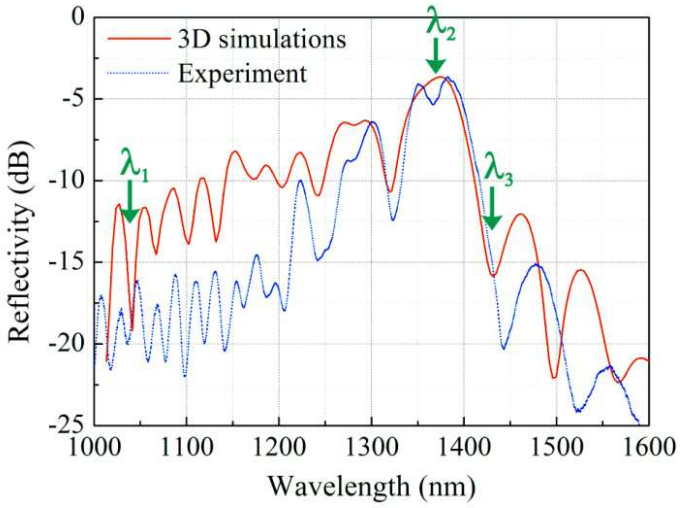

Figure 3-10 MFBG reflectivity spectra. The red and blue lines represent 3D simulations and experimental results, respectively. λ_1, λ_2 and λ_3 represent the wavelengths at which electric fields are shown in Figure 3-9 (a), (b) and (c).

Figure 3-10 presents the theoretical reflectivity against the wavelength (red line) evaluated using the *S*-parameter function. *S*-parameters are complex-valued, frequency dependent matrices describing the transmission and reflection of electromagnetic energy measured at different ports of the device. As for the experiment (reported in blue for reference), numerical calculation shows a reflection peak at λ~1364 nm. The two graphs show a few differences, like a different periodicity, a double Bragg peak in reflection and a wavelength shift. A possible explanation might be related to the different polarization conditions: while in the experiment light was not polarized, simulations allowed for only one linear polarization. Moreover, since the upper part of the MFBG is surrounded by air in the experiment, the two polarizations experience different surroundings, thus a different effective refractive index. Possible explanations for the other spectral mismatches include the presence of unwanted high order modes in the polymer cladding, the only-partial grating

embedding in the experiments, or different effective indices of the mode propagating in the microfibre between experiments and simulations due to diameter fluctuation and/or residual stresses. Finally, small imperfections in periodicity and/or lateral position of the grating notches can amount to small spatial phase and grating strength error, which are known to affect the grating reflectivity more severely in the out-of-band spectral region [153].

3.3 Microfibre phase-shifted Bragg grating (MPSBG)

3.3.1 Working principle and fabrication

As explained in section 3.1.1.2, phase shifted gratings are gratings with a gap inside the grating region. In this section a MPSBG is demonstrated and used to obtain 3D light confinement. Since in optical microfibres light is radially confined by the cladding/air interface, for appropriate taper diameters confinement to the diffraction limit can be achieved. Longitudinally, confinement is provided by the phase shift in the centre of the MPSBG: the distance along which confinement occurs is related to the refractive index contrast of the grating. In order to maximize such confinement (thus minimize confinement length), MPSBGs were manufactured carving notches in the microfibre, thus achieving an index contrast of ~0.45 at the wavelength λ~1 μm.

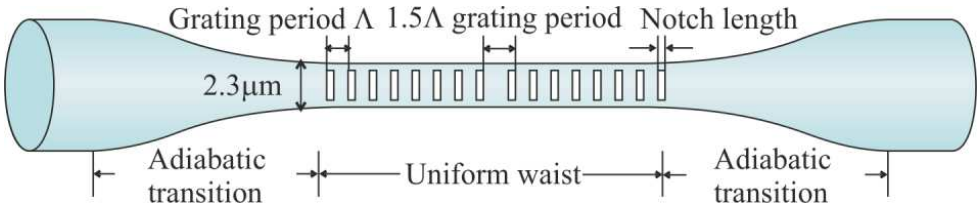

Figure 3-11 Schematic of the MPSBG. The cavity is created by a phase shift in the centre of a grating inscribed in the uniform waist region of an optical fibre taper.

Figure 3-11 shows a schematic of the proposed microfibre phase-shifted Bragg grating resonator with 20 periods (Λ) and a 1.5 Λ phase shift in the centre. The cavity is made by inducing a phase shift in the centre of a grating inscribed in a microfibre (the uniform waist region of an optical fibre taper). The two conical transition regions at the microfibre extremities connect the

cavity to conventional optical fibre pigtails, which allow for a prompt connection to fiberized sources/devices.

As before, the cavity fabrication process involved four main steps: manufacture of optical microfibres; deposition of a thin gold layer; FIB nanopatterning and gold etching.

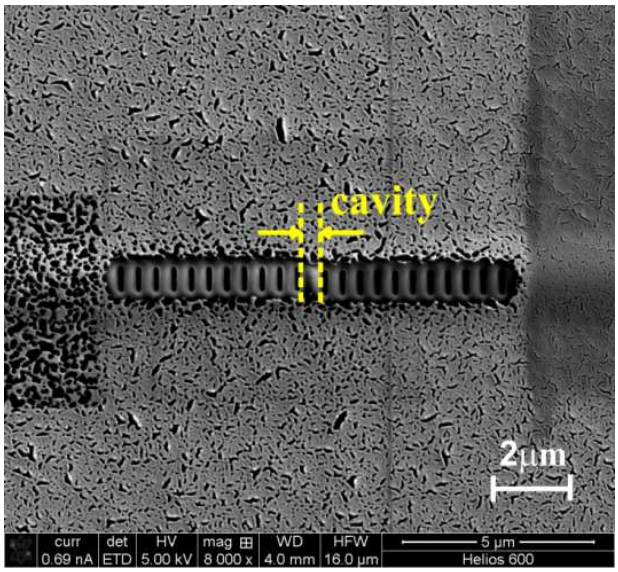

Figure 3-12 SEM image of the MPSBG. The cavity is at the grating centre and is highlighted in yellow. The microfibre is partly embedded in a polymer and coated by a ~50 nm gold layer to avoid charging during FIB milling.

The microfibre was fabricated from a conventional telecom single mode fibre (SMF-1300/1550-9/125-0.25-L (OZ optics, Canada)) down to ~2 μm using the microheater bushing technique (Section 1.1.1.2). To avoid additional optical losses, the microfibre was packaged on a microscope slide coated by a layer of Efiron PC-373 (Luvantix, Ansan-si, Korea), having a cured refractive index of n~1.373 at λ=1550 nm. Since bare microfibres undergo rapid mechanical and optical degradation [154] when their diameter is comparable with the wavelength of the light they guide, to increase the device sturdiness [155, 156] part of the microfibre was embedded in a low refractive index polymer and the microfibre pigtails were fixed to the microscope slide using two small drops of UV curable polymer (UV375, also from Luvantix). A 50 nm layer of gold was then deposited on the taper surface to avoid charging during FIB milling using an electron beam evaporator. Notches were carved using the FIB system "Helios 600" (FEI Inc., Hillsboro, USA); the gallium ion beam accelerating voltage and current were 30.0 kV and 93 pA, respectively. FIB

beam sizes smaller than 30 nm can be easily obtained, thus notch sizes can be controlled with a good degree of precision. Figure 3-12 shows a SEM image of the gold-coated MPSBG: the notch dimensions, microfibre diameter and grating periods are 156.2 nm ×718.7 nm, ~2.3 μm and 467 nm, respectively; the microcavity length is 687.5 nm. Gold coating was removed with gold-etching solvent which contains iodine and potassium iodine after FIB milling was completed.

3.3.2 Microfibre phase-shifted Bragg grating characterization

The device optical properties were characterized with the experimental set-up shown in Figure 3-6. As before, the spectral response of the coupler output was firstly recorded without any sample to provide a normalization base for the following spectra.

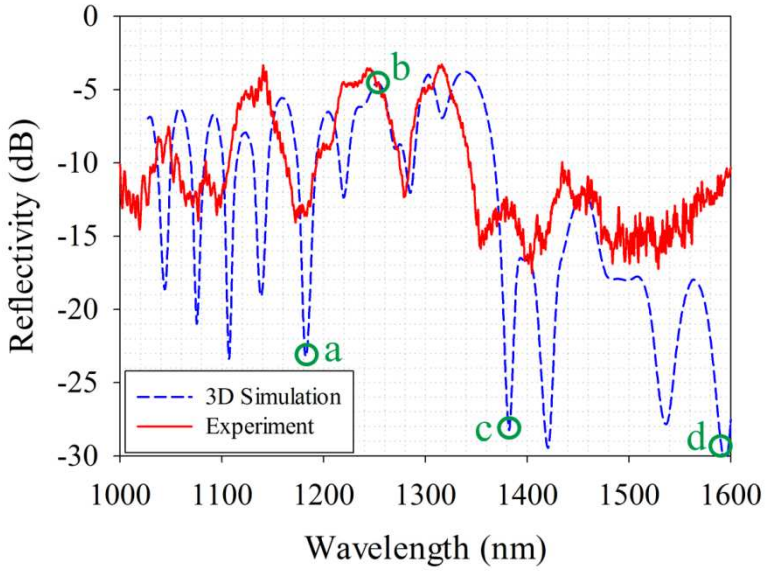

Figure 3-13 Reflection spectra of MPSBG. The red and blue lines represent experimental results and simulations with the same structure as the sample, respectively. Points a, b, c and d in simulations represent the wavelengths of the electric fields which are shown in Figure 3-15 (a), (b), (c) and (d).

Figure 3-13 shows the reflection response of the proposed microfibre phase-shifted Bragg grating. The red and blue lines show the experimental results and the theoretical predictions modelled with the dimensions obtained from the SEM image. Experiments show a resonance dip at λ~1180 nm, which

corresponds to the cavity resonant wavelength. Other dips observed at shorter and longer wavelengths are associated with the F-P nature of the gratings at either side of the cavity. These dips are not associated with energy confinement in the cavity region. From the width ($\Delta\lambda$) and the central position (λ_B) of the cavity dip in Figure 3-13, it is possible to evaluate the cavity quality factor (Q), defined as [157]:

$$Q = \Delta\lambda / \lambda_B \tag{3-9}$$

For the manufactured cavity Q~60.

3.3.3 Modelling of microfibre phase-shifted Bragg grating

Simulations were carried out to evaluate the microcavity confinement properties using COMSOL Multiphysics 4.1. The microfibre diameter (D), grating pitch (Λ), central phase shift (1.5 Λ), notch length and notch width were chosen to be the same as the experimental sample. Figure 3-14 shows the modelling geometry. Due to the symmetry of the structure, a half cylinder was simulated in this study. The chosen boundary conditions were perfect electric conductor at the symmetry plane (flat surface at the top in Figure 3-14) and scattering boundary condition at the cylinder outer surfaces (the definition of boundary conditions are introduced in Appendix A). The maximum mesh element sizes were 150 nm in silica, 300 nm in polymer and 75 nm in air. A single mode was launched from the input port. The reflection spectrum was evaluated using the S-parameter function. The reflection spectrum is shown in Figure 3-13 for comparison with the experimental results, indicating a reasonable agreement. The small wavelength peak shift (~5 nm) shown in Figure 3-13 can be associated to the surrounding refractive index, which in the simulations is taken as polymer, while in the experiments is a combination of air and polymer (the microfibre is only partially embedded in the polymer). Possible explanations for the other spectral mismatches include the presence of unwanted high order modes, the only-partial cavity embedding in the experiments, a different effective index of the mode propagating in the microfibre between experiments and simulations, the Ga^+ contamination and an imperfect periodicity in the grating notches.

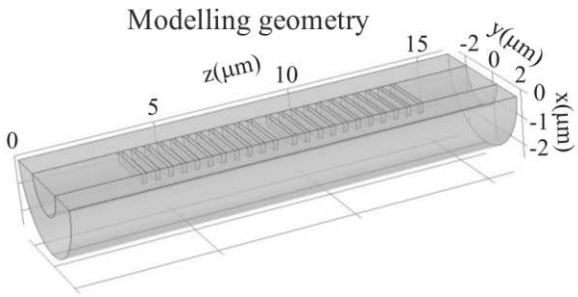

Figure 3-14 The modelling geometry of MPSBG.

The electric fields were evaluated at different wavelengths and points a, b, c and d in Figure 3-13 represent the wavelengths for which the electric field is shown in Figure 3-15 (a), (b), (c) and (d): at λ_a=1181.1 nm (Figure 3-15 (a)), light is longitudinally confined in the cavity MPSBG centre; at λ_b=1252.6 nm (Figure 3-15 (b)), the grating band-stop wavelength, most of the light is reflected similarly to the case of a simple FBG; at λ_c=1382.5 nm (Figure 3-15 (c)), which is not the resonance dip, the electric field shows no confinement; for wavelengths outside the band-stop (Figure 3-15 (d)), almost all the light can be transmitted through the waveguide.

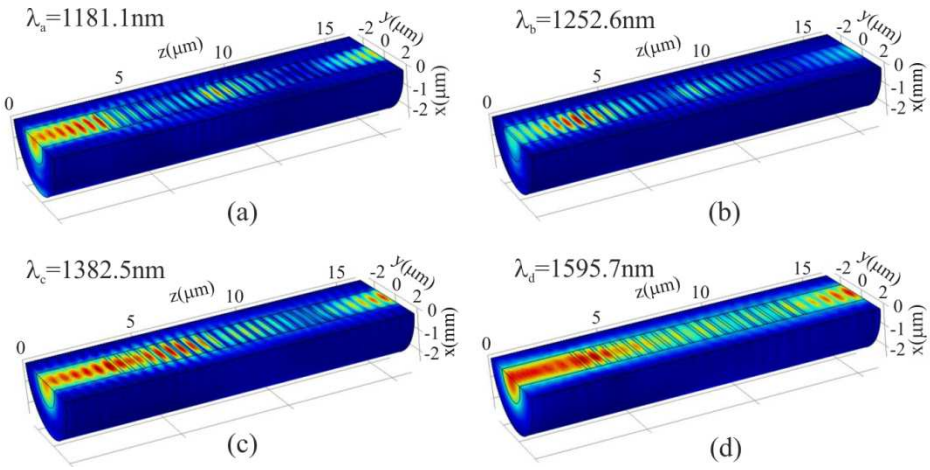

Figure 3-15 Electric field of simulated PSBG at (a) λ_a=1181.1 nm, (b) λ_b=1252.6 nm, (c) λ_c=1382.5 nm and (d) λ_d=1595.7 nm.

Figure 3-16 presents the electric field amplitude along the microfibre phase-shifted Bragg grating axis at λ_a=1181.1 nm, showing that light is longitudinally confined within 2 μm from the centre.

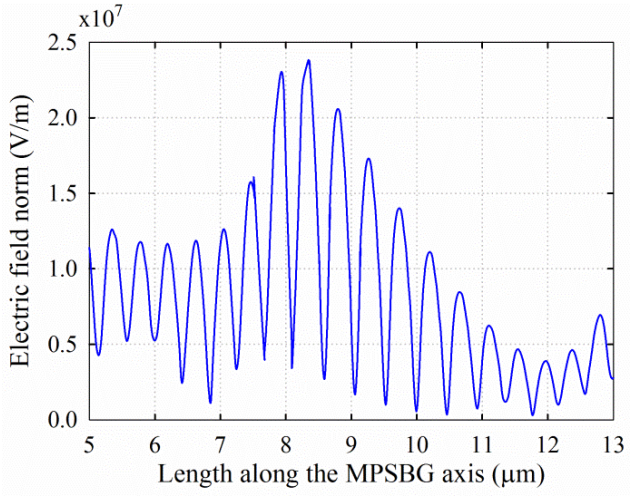

Figure 3-16 Electric field amplitude against the length along the MPSBG axis at λ_a=1181.1 nm.

Although here only a simple structure is considered, further optimization of manufacturing parameters (such as the grating pitch number and period, the notch width and the length and the microfibre diameter) can provide a more compact device with improved performance. In analogy to the case of phase-shifted fibre Bragg gratings [158], the cavity response is related to the grating length and *Q*-factors in excess of 10^3 can be predicted for a larger number of notches.

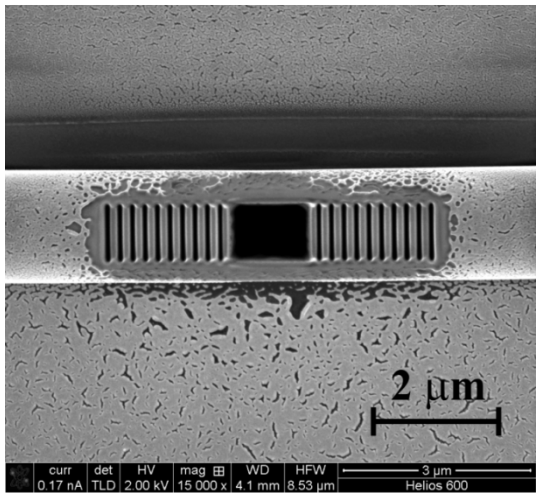

Figure 3-17 A MPSBG designed for polyfluorene emitting at wavelength λ=560 nm. The notch dimensions, taper diameter and grating periods are 100 nm×900 nm, ~1.78 μm and 200 nm, respectively; the microcavity length is 1.23 μm.

If a suitable active medium, e.g. polyfluorene, fills the microfibre phase-shifted Bragg grating central cavity a laser with extremely small size can be achieved. The MPSBG shown in Figure 3-17 is designed for emitting at a wavelength λ=560 nm when polyfluorene is filled in the centre cavity. The

notch dimensions, microfibre diameter and grating periods are 100 nm×900 nm, ~1.78 μm and 200 nm, respectively; the microcavity length is 1.23 μm. Accurate material deposition in the cavity is a big challenge and the laser experiment will be done in future work.

3.4 Conclusion

In this chapter, a robust and extremely short MFBG has been manufactured by inscribing periodic biconcave air notches in a microfibre and 3D light confinement was achieved in a MPSBG microcavity. 3D COMSOL simulations were carried out to support experimental results.

This compact MPSBG can find a wealth of applications, ranging from sensing to triggered single-photon sources [159]. In particular, in sensing, the size of the grating is a key issue: while the size of conventional FBGs is limited by Δn and by the fibre diameter, in a microfibre with only a few micrometres diameter, the grating size can be decreased drastically and the presence of a strong evanescent field can increase the sensor sensitivity to environmental properties.

Chapter 4 Fast-response microfibre coupler tip high temperature sensor

> If I have seen further it is by standing on the shoulders of Giants.
>
> Isaac Newton

A compact thermometer based on a broadband *Microfibre Coupler Tip* (MFCT) is demonstrated in this chapter. The thermometer dynamic range spans from 85ºC to 1511ºC with a response time of tens of microseconds, which is the highest temperature measured with a silica optical fibre device. An average sensitivity of 11.96 pm/ºC is achieved for a coupler tip with ~2.5 μm diameter in the temperature range ~247ºC to ~1283ºC, comparable to the value obtained for FBG thermometers at lower temperature. A resolution of 0.66ºC and 0.10ºC is achieved for a coupler tip diameter of ~12.6 μm and 4.7 μm respectively. Better resolution can be predicted for smaller size MFCTs.

M. Ding, P. Wang, and G. Brambilla, "A microfibre coupler tip thermometer," *Opt. Express* **20**, 5402-5408 (2012).

M. Ding, P. Wang, and G. Brambilla, "Fast-response high-temperature microfibre coupler Tip thermometer," *IEEE Photonics Tech. Lett.* **24**, 1209-1211 (2012).

4.1 Background

Temperature monitoring is vital for many applications in harsh environments, such as the oil and gas industries, power generation, or engine turbines. Because of their immunity to electromagnetic interference and possibility to work in contact with explosives which is because the optical fiber is a dielectric and thus is nonconducting, the use of optical fibres for temperature monitoring has been widely investigated [48-51]. Among optical fibre devices, *Fibre Bragg Gratings* (FBGs) [49, 160, 161] are possibly the most common tool used for temperature sensing. FBGs inscribed in telecom optical fibres can reach temperatures T as high as 800ºC [162]. Regenerated FBGs written in silica optical fibres have been shown to be capable to reliably with stand 1000ºC [163] and reach temperatures as high as 1295ºC [52], but they require specialty fibres and a long manufacturing process which includes hydrogen loading, a cumbersome grating writing equipment working with toxic gases and a relatively long post fabrication annealing. In addition to a relatively complex and expensive process, FBGs are large (diameter ~125 μm and length ~1 cm) which restricts their application for high resolution measurements. The performance of sensors is typically defined using a set of parameters including: responsivity, repeatability, resolution and response time. These parameters are defined as:

Responsivity (also called sensitivity) R: responsivity describes the change in the parameter used for detection as a result of a change in the parameter being monitored. For example in the case of refractometric sensors a change in the refractive index, which is a parameter to monitor and is measured in refractive index units (RIU), is very often understood in terms of shift in wavelength, which is a detection parameter, measured in nm, yielding the value of responsivity as nm/RIU. In this work, R is defined as the wavelength shift associated to a temperature change.

Repeatability: repeatability is an indication of the agreement between the measured performances of the same sample taken under the same experimental conditions at different times. A good repeatability reflects the stability and life-time of the sensor head.

Resolution *S*: resolution indicates the smallest detectable change in the parameter used for detection. For this sensor, *S* is defined as the minimum temperature change that the sensor can distinguish. Spatial resolution is defined as the minimum spatial size that the sensor can distinguish.

Response time τ: response time is typically defined as the time required taken for the detection parameter to rise from 1 to 1/e of its initial value.

In this chapter, a compact thermometer based on a microfibre coupler tip (Figure 4-1 (b)) is presented. In 2009, Y. Jung et al. [152] demonstrated a broadband single mode bi-conical 2×2 *Microfibre Coupler* (MFC) (Figure 4-1 (a)) with specifically designed transition regions which effectively suppress any high order mode present at the input fibre and provide efficient power splitting of the fundamental mode at the two output ports. The microfibre coupler was manufactured by laterally fusing and tapering two twisted optical fibres. By controlling the taper transition profiles and the MFC minimum diameter in the uniform waist region, single mode operation over the wavelength range 700 - 1700 nm was demonstrated.

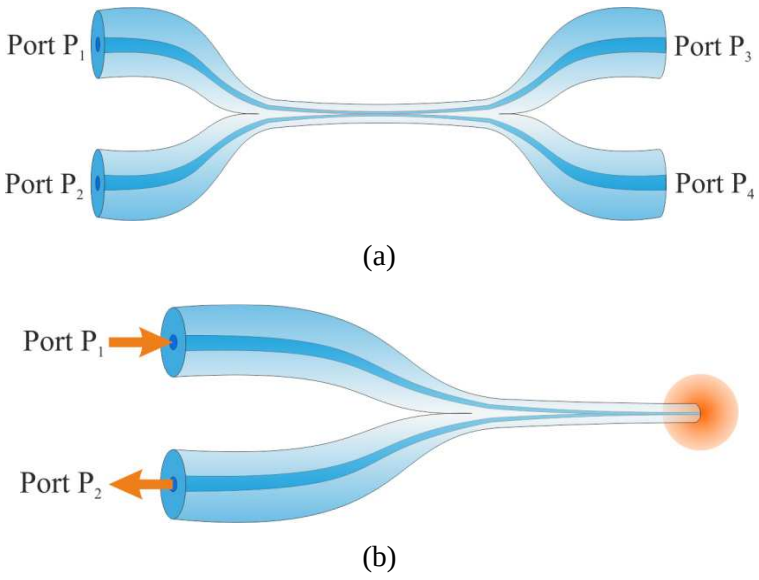

Figure 4-1 Schematic of (a) a bi-conical MFC and (b) a bi-conical MFCT.

While fused optical fibre couplers have found many applications in optical communication due to their high performance and low cost, their application to temperature monitoring [164] is related only to low temperature (below 100ºC) and resulted in low responsivity. In this chapter, MFCs with diameters larger than 2 μm were chosen to ensure high sensitivity, high spatial resolution,

an adequate rigidity for the thermometer head and a wide temperature measurement range, even if this potentially resulted in multimode guidance. In the coupling region, supermodes (the modes generated by the combination of the input modes in the waist) with different propagation constants provide a continuous change in the power distribution along the coupler cross-section, which results in a different power splitting at the output ports for different optical paths. The modes' optical paths depend both on the coupling region length and the refractive index of the coupling region; since both depend on the surrounding environment, and in particular on the temperature, the microfibre coupler can be used as a highly sensitive thermometer. In conventional optical fibre couplers, the periodicity in the coupler transmission spectrum is typically few hundred nanometres, therefore a small temperature increase results in a proportionally small shift, thus small responsivity [164]. On the contrary, in MFCs, this periodicity is of the order of few/tens of nanometres: a wavelength shift of few nanometres generally results in large changes in the transmitted power at a specific wavelength, thus a high responsivity. Moreover, since the microfibre coupler tip is made of silica, which softens at 1680ºC [165], it is predicted that it can potentially reach very high temperatures.

4.2 Microfibre coupler tip (MFCT) sensor fabrication

The MFCT thermometer was manufactured by cutting a MFC (Figure 4-1 (a)) into two equal parts at the centre of the minimum waist region. A microfibre coupler comprises two conical transition regions, a central uniform waist region and four input/output ports: light injected into ports P_1 or P_2 exits the MFC from ports P_3 and P_4. In the microfibre coupler tip, light launched into port P_1 is partially reflected by the flat surface of the tip and can be measured at port P_2. In these experiments, a low-loss MFC was fabricated from two standard telecom optical fibres (Corning SMF-28) using the microheater brushing technique (Section 1.1.1.2). The lengths of tapered and uniform waist regions were ~25 mm and ~6 mm, respectively. Figure 4-2 (a) shows the SEM image of

the MFCT: the minimum diameter and length of the uniform waist region were ~2.5 μm and ~3 mm. The microfibre coupler tip spectral characterization was carried out using the set-up shown in Figure 4-5 (a): a *Supercontinuum* (SC) source was connected to port P_1 and an OSA to port P_2 (SC source and OSA are the same as used in earlier experiments of Section 2.4). The reflection spectrum at room temperature is presented in Figure 4-2 (b) and shows the periodic multipeak pattern of optical fibre couplers. In contrast with conventional fused couplers made from telecom single mode optical fibres, the pattern is not limited to the 1250-1750 nm range, but covers the whole investigated wavelength range 700-1700 nm. A long wavelength modulation is superimposed on the coupler spectrum and it is due to the difference in coupling coefficient for *x* and *y* polarizations.

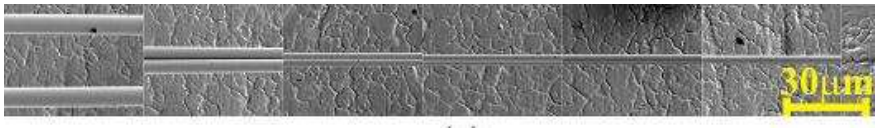

(a)

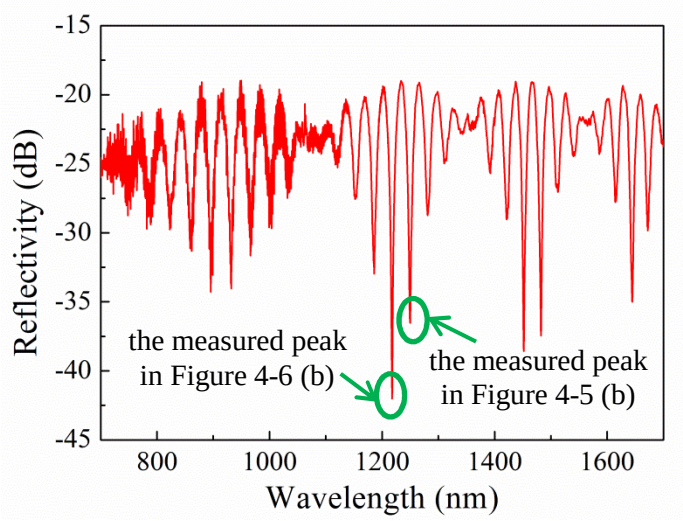

(b)

Figure 4-2 (a) SEM images of selected sections of the MFCT. Single microfibre diameter and uniform region length are ~2.5 μm and ~3 mm, respectively; (b) MFCT reflection spectrum at room temperature.

Figure 4-3 shows a photograph of the packaged microfibre coupler tip: the MFCT was inserted into a glass capillary with 600 μm inner diameter and 2 cm length to increase the thermometer stiffness. The capillary was fixed by superglue and ~1 cm length of tip is exposed in air. Three MFCTs were

fabricated in the experiments. Table 4-1 shows the specification of the samples.

Figure 4-3 Picture of a MFCT. The capillary has 600 μm inner diameter.

Table 4-1 The specification of MFCTs

Sample number	Diameter (μm)
1	2.5
2	12.6
3	4.8

4.3 Temperature dependence of the microfibre coupler tip

The microfibre coupler output can be understood by assuming that power exchange at the output ports occurs as a result of the interference between the lowest order symmetric and antisymmetric modes of the waveguide formed by the whole of the cross section of the fused region. From Figure 4-2 (a), the MFCT can be assumed to be a "weakly fused" coupler, approximated by two touching cylindrical waveguides (the inset of Figure 4-4 shows a schematic of the coupler cross section in this approximation). Since the original taper cores have a negligible size, they can be ignored and the coupling coefficients, C_x and C_y, for the *x* and *y* polarizations are given by [166]:

$$C_x = \frac{2^{3/2}(n_{silica}^2 - n_{air}^2)^{1/2} U_\infty^2 (2n_{silica}^2 V + 1)}{n_{silica}^3 D(\sqrt{\pi}) V^{7/2}} \quad (4\text{-}1)$$

$$C_y = \frac{2^{3/2}(n_{silica}^2 - n_{air}^2)^{1/2} U_\infty^2 (2n_{silica}^2 V - 1)}{n_{silica}^3 D(\sqrt{\pi}) V^{7/2}} \quad (4\text{-}2)$$

where n_{silica}=1.444 and n_{air}=1.0003 are the refractive indices of silica and air at wavelength λ=1550 nm, D is the diameter of one of the microfibres, $U_\infty = 2.405$ [36] and $V = [(2\pi D)/\lambda](n_{silica}^2 - n_{air}^2)^{1/2}$ [36].

If light entering the input port P_1 in the MFC is unpolarized, the normalized power at the output port P_4 can be described by:

$$P_4 = \frac{1}{2}\{1 - \cos[(\overline{C_x} + \overline{C_y})L]\cos[(\overline{C_x} - \overline{C_y})L]\} \quad (4\text{-}3)$$

where L is the coupling length of the MFC which includes the waist uniform region and the transition region and $\overline{C_x}$ and $\overline{C_y}$ are the values of (4-1) and (4-2) averaged over the whole length where coupling occurs. Because of the large modal size and the relatively small overlap, the contribution of the transition regions to the average coupling coefficients is small/negligible.

In the microfibre coupler tip, light launched from port P_1 is reflected by the tip and the power emerging from P_2 is proportional to P_4 such that:

$$P_2 = \left(\frac{n_{silica} - n_{air}}{n_{silica} + n_{air}}\right)^2 P_4 \quad (4\text{-}4)$$

Equations (4-1) (4-2) (4-3) and (4-4) show that the output power depends on the wavelength λ and on three factors (refractive index, coupling length L and coupler radial size $2D$), which are temperature dependent. The temperature dependence of the MFCT output spectrum was evaluated assuming that at λ~1530 nm the refractive index of silica at T=26ºC, 471ºC and 828ºC is 1.44444, 1.44961 and 1.45352 [167], respectively. The diameter of each microfibre in the uniform region and the length of the uniform region (2.5 μm and 3 mm, respectively) were assumed to expand with an average thermal coefficient 5.5×10^{-7}ºC^{-1}[168]. Figure 4-4 shows the output power variation at three different temperatures. The resonance peak shifts 15.5 nm when T is increased from 26ºC to 828ºC, with an average responsivity of 19.3 pm/ºC.

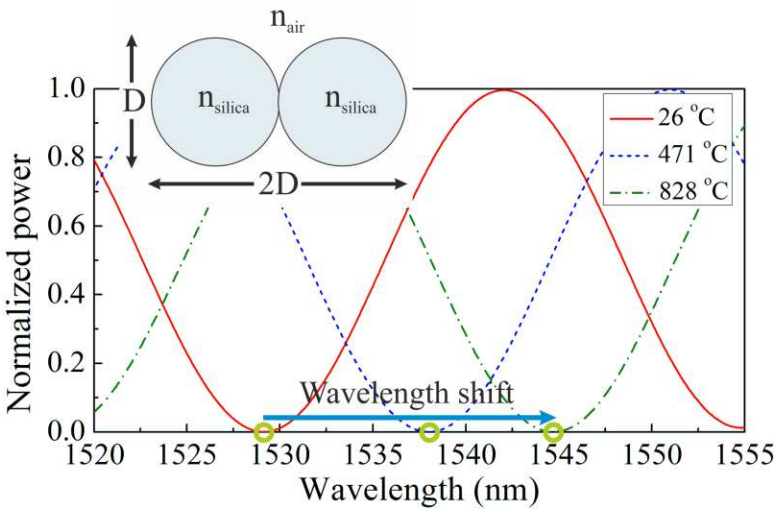

Figure 4-4 The output power from port P_2 at 26ºC, 471ºC and 828ºC. Inset: MFCT cross section in the "weakly fusing" approximation.

4.4 MFCT characterization

4.4.1 Temperature monitoring methods

The MFCT spectral characterization was carried out using the set-up shown in Figure 4-5 (a). The microheater (NTT-AT, Tokyo, Japan) used to fabricate the MFC was also used for temperature testing, as it can reach temperatures in excess of 1500ºC. The MFCT was inserted into the microheater centre and reflection spectra were recorded at different temperatures. The microheater temperature was changed by increasing the current flowing into the microheater.

The reflection spectrum of sample 2 for increasing temperatures is presented in Figure 4-5 (b) and shows a resonance peak at the wavelength λ~1246 nm (red dash curve). When the microheater current is increased, the temperature increases and the peak redshifts to longer wavelengths. Two temperature monitoring methods can be used to measure the temperature: (I) at a fixed power, the wavelength shifts to longer wavelengths with increased temperature and this shift can be evaluated by recording the reflection spectrum using an OSA; (II) at a fixed wavelength the power change over a bandwidth of 1 nm is evaluated. The OSA was used as a replacement for a

passband filter and a power meter at a certain wavelength (λ=1300 nm in Figure 4-5 (b)). When the temperature was increased, the recorded intensity at λ=1300 nm decreased.

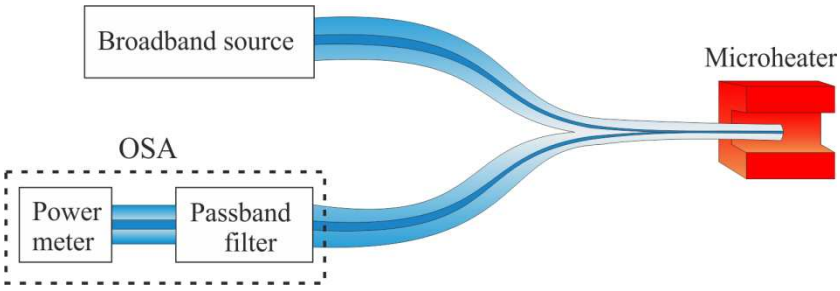

(a)

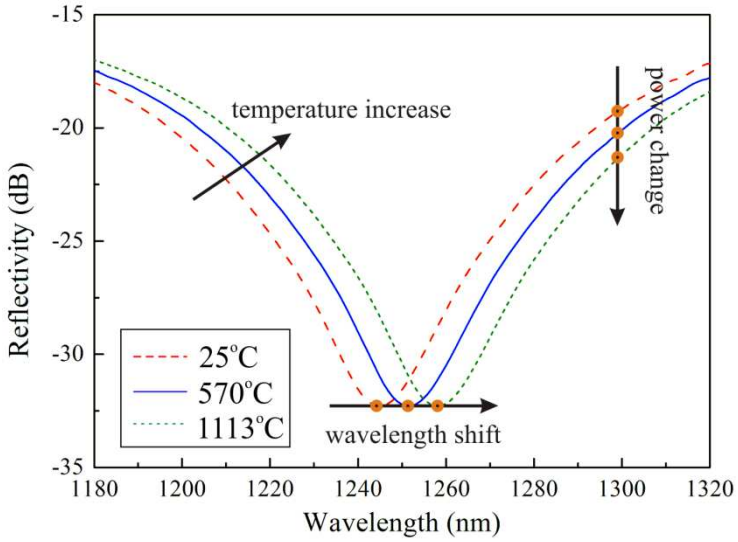

(b)

Figure 4-5 (a) MFCT characterization set-up; a broadband SC source injects light into port P_1, and reflected light is collected at port P_2 by an OSA (SC source and OSA are the same as used in earlier experiments of Section 2.4); (b) reflection spectra of sample 2 when the temperature increases.

4.4.2 *Temperature monitoring from wavelength shifts*

4.4.2.1 Responsivity

The sensor responsivity (also called sensitivity) *R* is defined as the wavelength shift associated to a temperature change. The temperature responsivity of sample 1 was monitored from the wavelength shift as shown in Figure 4-5 (b). The microheater temperature was changed by increasing the current flowing into the microheater from 0.4 A to 2.8 A in steps of 0.2 A. Measurements were taken every 15 minutes to ensure a stable temperature. The microheater

response was previously proposed in ref. [169] and we measured and reported it again in Figure 4-6 (a) to include small currents. Figure 4-6 (b) shows the spectral shift of the peak at 1219 nm in Figure 4-2 (b) for increasing currents. When the driver current is increased, the temperature increases and the peak redshifts to long wavelengths, as predicted by simulations in Figure 4-4.

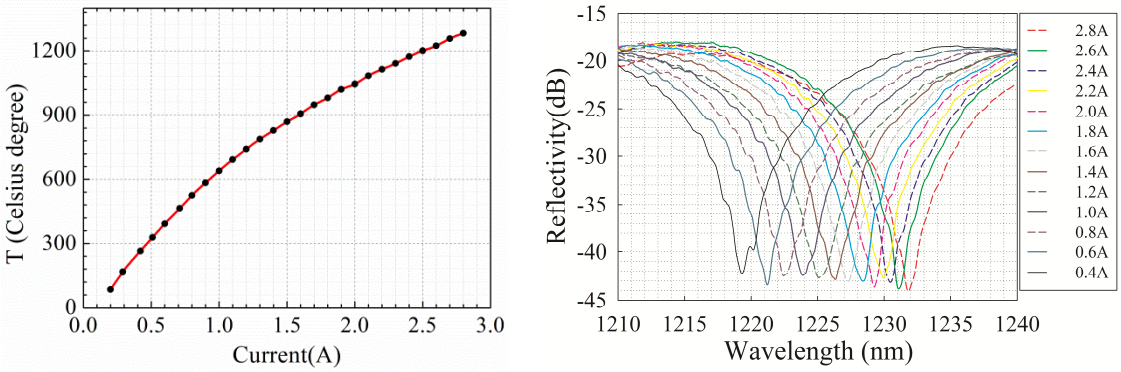

(a) (b)

Figure 4-6 (a) Relation between the driver current and temperature of microheater; (b) reflection spectra of the peak at 1219 nm in Figure 4-2 (b) when the driver current increases from 0.4 A to 2.8 A by steps of 0.2 A (sample 1).

In order to minimize the measurement error, spectra were fit with Lorentzian functions and the fit peak wavelength was used to calculate the wavelength shift. An average R~11.96 pm/ºC was achieved in the temperature range ~247ºC to ~1283ºC, comparable to the value obtained for FBG thermometers at lower temperature [53, 54]. The possible explanation for the difference between the theoretical calculation R~19.3 pm/ºC in Figure 4-4 and experimental measurement could be the non-perfect weakly fused coupler structure, the error in the measured wavelength difference and/or in the refractive index. The sensor resolution S was estimated to be ~0.836ºC for an OSA resolution of 0.01 nm. Better resolutions can be potentially achieved with more spectral data points for the Lorentzian fitting and/or better signal/noise (i.e. spectral averaging).

4.4.2.2 Repeatability

The MFCT temperature sensor repeatability was measured by recording spectra for increasing and decreasing temperatures with an interval of one hour for sample 1. The wavelength shift with the temperature is shown in Figure 4-7:

data from the two curves fit very well within 3ºC, showing that the MFCT thermometer has good repeatability. The measured errors in wavelength shift and temperature are within 50 pm and 0.5ºC respectively.

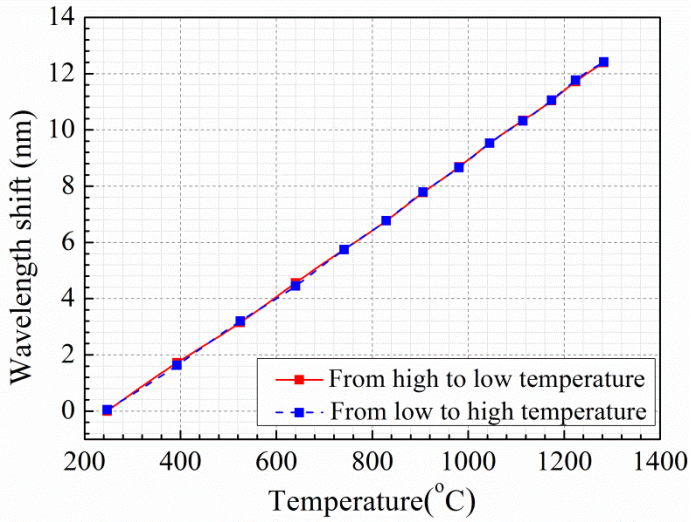

Figure 4-7 Wavelength shift dependence on the microheater temperature. The red solid curve and the blue dash curve report measurements for decreasing and increasing temperatures, respectively (sample 1).

4.4.2.3 2D spatial resolution

In order to demonstrate the sensor's high 2D spatial resolution, measurements with sample 1 were carried out as shown in Figure 4-8 (a). A Nickel-Chromium (Ni-Cr) wire with ~500 μm diameter was heated exploiting its Ohmic effect. Spectra were recorded every 125 μm at a distance of ~250 μm from the Ni-Cr surface along the tangential direction: the peak shift of the Lorentzian fitting spectra variation with the MFCT position is presented in Figure 4-8 (b), with the origin taken at the central axis of the wire. A sharp peak with a *Full Width at Half Maximum* (FWHM) of ~1150 μm was observed. A wavelength shift of 1.19 nm was recorded at the wire centre corresponding to a temperature difference of ~99ºC. If heat is assumed to be dissipated by conduction in air, the T profile can be easily found from the solution of Fourier's law in stationary state, which leads to the Laplace equation: $\nabla^2 T = 0$ [170]. The solution provides the following equation along the line used for measurement:

$$T = C_1 \times \ln[x^2 + (500\mu m)^2]^{1/2} + C_2 \qquad (4\text{-}5)$$

where C_1 and C_2 are constants related to the heat transfer density and wire diameter, and x is the distance from the closest point in the measurement. A

reasonably good fit between Equation (4-5) theory and experimental data shown in Figure 4-8 (b) occurred for C_1=-284.7ºC/µm and C_2=1114.7ºC, respectively. The small difference between the two curves can be associated to the tip head movement, to the wire temperature fluctuations during the measurement and to the stage movement error. Measurement errors are shown with error bars.

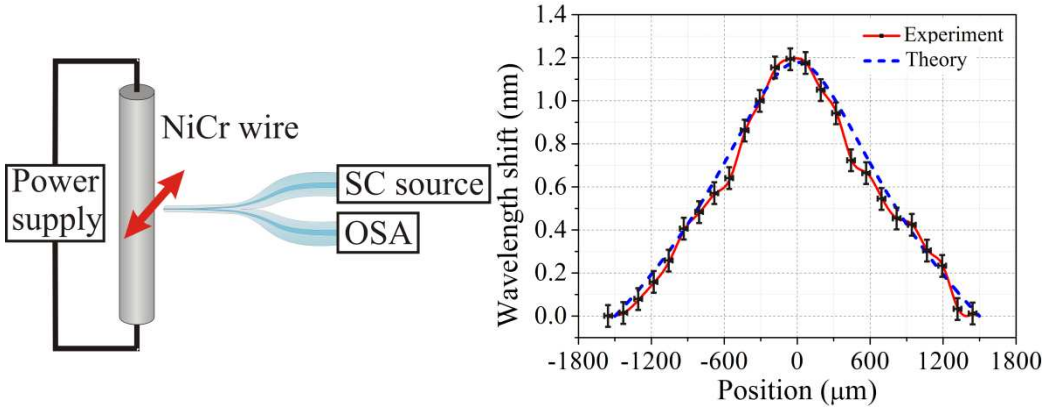

(a) (b)

Figure 4-8 (a) Experimental set-up used to demonstrate the MFCT 2D spatial resolution; (b) sensor response when the MFCT was scanned along the tangential direction of the Ni-Cr wire at ~250 µm from the wire surface. The red solid and the blue dashed curves are the experiment results and the curve expected from the heat transfer equation, respectively (sample 1).

4.4.3 *Temperature monitoring from power changes*

Power changes at a fixed wavelength (Figure 4-5 (b)) were used to characterize sample 2 and 3.

4.4.3.1 Response time

The device response time is related to its mass and thermal properties. In the heat transfer calculation, the Biot number is a dimensionless number and it determines whether the temperatures inside a body will vary significantly in space, while the body heats or cools over time, from a thermal gradient applied to its surface. It also defines whether the heat exchange with the body's surroundings will occur mainly by convection or conduction. The Biot number (*Bi*) is defined as [170]:

$$Bi = \frac{hL_C}{k_b} \tag{4-6}$$

where h is convective heat transfer coefficient, L_C is characteristic length, which is commonly defined as the volume of the body divided by the surface area of the body, k_b is thermal conductivity of the body.

In this work, as the Biot number is greater than 10^3 [170], heat loss by convection is considerably greater than that by conduction and the MFCT dynamic thermal behaviour can be described by:

$$h_s A(T_f - T)dt = c\rho V dT \tag{4-7}$$

where V and A are the volume and surface area of the heated region, h_s, c and ρ are the surface convection coefficient, heat capacity and density and T_f is the surrounding fluid temperature. The integration of this equation shows that the time constant (thus response time) of the device is given by:

$$\tau = \frac{c\rho V}{h_s A} = \frac{c\rho}{h_s}\frac{a}{2} \tag{4-8}$$

and it is proportional to the MFCT radius a. Assuming h_s=418.68 W/m^{2}K [171], c=0.8 kJ/kg·K, ρ=2300 kg/m^3 and a=6.28 μm, the device response time results to be τ=13.8 ms.

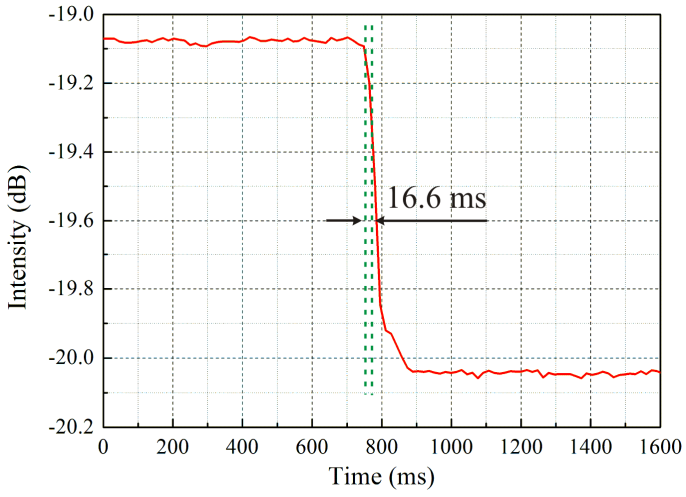

Figure 4-9 Measurement of MFCT response time of sample 2: the temporal dependence of the MFCT reflected intensity was recorded for a rapid temperature change, resulting in a response time of ~16.6 ms.

The thermometer response time was measured by rapidly inserting the MFCT into the microheater; the driver current was set at ~2.00 A corresponding to T~1045°C (Figure 4-9). For sample 2, a response time of

~16.6 ms was measured, comparable with the value obtained from Equation (4-8).

4.4.3.2 Dynamic range, Responsivity and Resolution

The temperature response of sample 2 was carried out using the set-up shown in Figure 4-5 (a). The microheater temperature was changed from 0.2 A to 3.6 A in steps of 0.2 A. Measurements were taken every 15 minutes to ensure a stable temperature. When the temperature stabilized, the MFCT was rapidly inserted into the microheater and then taken out. The intensity response is presented in Figure 4-10 and it shows that the intensity dip increases for increasing currents. The intensity dip at microheater current 0.6 A is presumably a measurement error.

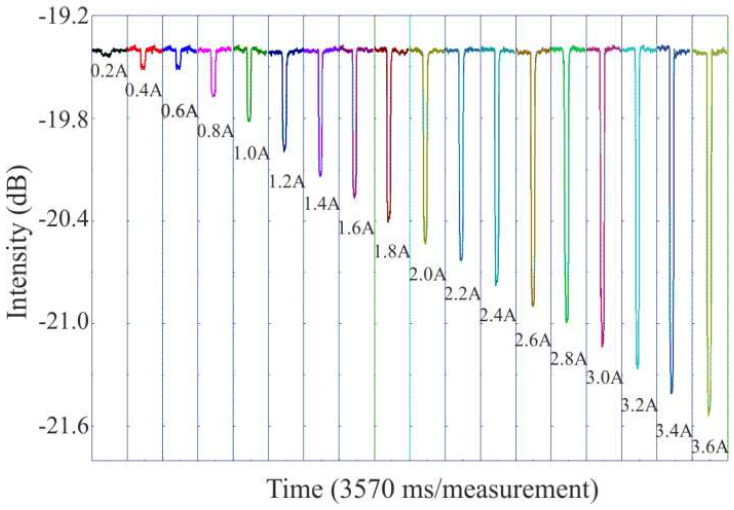

Figure 4-10 Temporal intensity change for sample 2 when the tip is repeatedly inserted and taken out from the microheater at different temperatures. The temperature was changed by changing the driver current from 0.2 A to 3.6 A in steps of 0.2 A. The current of 3.6 A corresponds to T~1511ºC. Current-temperature calibration is reported in Figure 4-6 (a).

Figure 4-11 presents the relationship between the measured intensity and the microheater temperature for samples 2 and 3, which are both monotonically decreasing functions. The maximum dynamic range was achieved for sample 2, which reached T=1511ºC. The sensor responsivity R, defined as the change in the sensor output per unit signal change, corresponds to the curve slope in Figure 4-11. Sample 2 has R~1.514×10^{-3} dB/ºC, smaller than that of sample 3 (~9.748×10^{-3} dB/ºC).

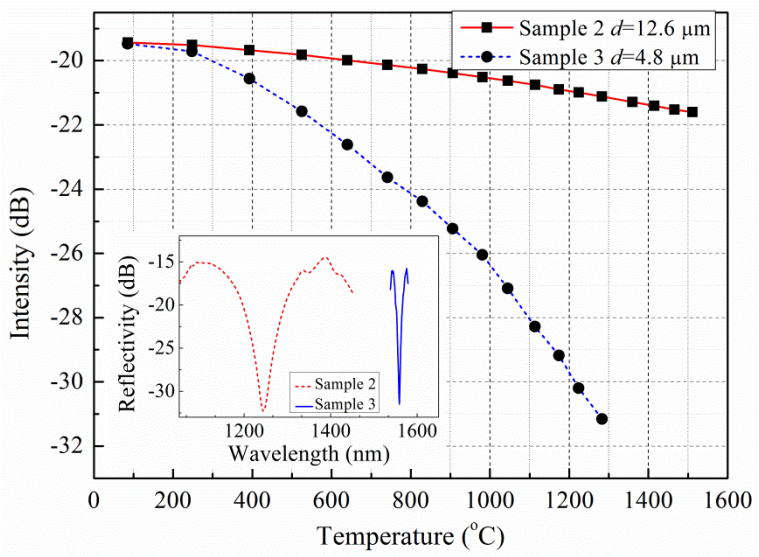

Figure 4-11 Relationship between measured intensity and the microheater temperature. Inset: resonance peaks used for *T* measurements in sample 2 and 3, respectively.

The sensor resolution *S* is defined as the minimum temperature change that the sensor can distinguish. Since the power resolution of the OSA (and commonly of many power meters) is of the order 10^{-3} dB, an average *S*~0.66ºC was achieved in the temperature interval ~85ºC to ~1511ºC for sample 2; this is higher than that previously obtained measuring the peak shift in Section 4.4.2.1 [172]. Sample 3, with smaller diameter, has better resolution *S*~0.10ºC but smaller dynamic range (from *T*~85ºC to *T*~1283ºC). The inset of Figure 4-11 presents the resonance peaks used for *T* measurements in sample 2 and 3, respectively. In sample 2, which has a FWHM of 127 nm, the gradient of the resonance peak is small, corresponding to a wide temperature measurement range and low *S*. On the other hand, in sample 3 a smaller diameter corresponds to a sharper resonance peak: the steep slope provides a high *S* in exchange for a smaller dynamic range.

4.5 Conclusion

In summary, a compact temperature sensor which uses a MFCT for fast response, high temperature sensing with high 2D spatial resolution has been demonstrated. This device exploits the temperature dependence of intermodal coupling in the coupler uniform waist region. Two different methods were used to monitor the temperature: monitoring the wavelength shift at the peak

intensity and monitoring the power change at a constant wavelength. By evaluating the wavelength shift at a fixed power, sample 1 with a 2.5 μm diameter was characterized, having a responsivity of 11.96 pm/ºC and an operational range exceeding 1200ºC (from room temperature to ~1283ºC). A measurement with a sub-200 μm 2D spatial resolution has also been demonstrated. Because of the small coupler cross section, the theoretical device resolution is limited by the Raleigh criterion, meaning that measurements with resolutions smaller than 5 μm can be possible. Sample 2 with a 12.6 μm diameter and sample 3 with a 4.8 μm diameter were characterized by evaluating the power change at a fixed wavelength. The temperature sensor 2 had a resolution of 0.66ºC and wide temperature measurement range from 85ºC to ~1511ºC while sample 3, with smaller diameter, has better resolution S~0.10ºC but smaller dynamic range (from T~85ºC to T~1283ºC). To the best of our knowledge, 1511ºC is the highest temperature measured with a silica optical fibre device. Resolution can be improved with smaller size MFCTs.

MFCT offers several advantages, including compactness, extremely high temperature measurement capabilities, fast response, easy connection with other fiberized optical components, simple fabrication and low cost. By setting a reference wavelength and measuring the intensity ratio between the two wavelengths, the sensitivity can be further improved and the error associated with the source power drift/oscillations can be minimized [173].

Chapter 5 Whispering gallery mode selection in optical bottleneck microresonators

Nothing is withheld from us
which we have conceived to do.

Russell A. Kirsch

In this chapter, selective excitation of *Whispering Gallery Modes* (WGMs) in optical *Bottleneck Microresonators* (BMRs) is demonstrated by inscribing microgroove scars on their surface by *Focused Ion Beam* (FIB) milling. Substantially cleaner spectra are obtained in appropriately scarred BMRs; single mode operation is achieved by two asymmetrical perpendicular scars, providing the potential for high performance in sensing and other optical devices.

M. Ding, G. S. Murugan, G. Brambilla, and M. N. Zervas, "Whispering gallery mode selection in optical bottle microresonators," *Appl. Phys. Lett.* **100**, 081108 (2012).

5.1 Background

In recent years, devices based on optical microresonators have attracted increasing attention providing a wide range of applications, including strong-coupling *Cavity Quantum Electrodynamics* (CQED), efficient microlasers and filters, optical delay lines and miniature sensors [47, 174]. Several microresonator geometries, such as microdisks [147], microspheres [175] and microtoroids [145] have been studied and reported extensively in the literature. Optoelectronic devices based on optical microresonators rely predominantly on the excitation of high-Q WGMs, which can trap light in small volumes by total internal reflection between the resonator and the surrounding media. Thus optical WGM resonators can strongly confine photons and can potentially provide important functionalities in next-generation, compact-size, low-power and high-speed photonic circuits.

Recently, a new type of microresonator, the bottleneck microresonators [176-182] (Figure 5-1), has been demonstrated, which consists of a solid, strongly-prolate spheroid structure with the neck-to-neck distance L_b, bottle diameter D_b and stem diameter D_s, supporting highly non-degenerate WGMs and showing quite dense spectral features. In fact, unlike microspheres where mode-degeneracy masks such excitation, a rich variety of modes can be efficiently excited [179] in BMR depending on the excitation arrangement. The dense spectral features are highly advantageous when BMRs are used in CQED studies [180]. However, such spectral characteristics are a serious hindrance if BMRs are to be used as sensors, where a spectrum with features more easily identifiable and traceable over large wavelength ranges is desirable. The rich spectral features are a result of the strongly broken degeneracy between WGMs with common azimuthal and differing axial mode numbers, as a result of the highly prolate shape. In addition to different eigen frequencies, these non-degenerate resonances exhibit substantially different spatial intensity distributions along the bottle length [181]. This property of the resonant modes in a BMR can be exploited to differentially attenuate some of the modes, depending on axial mode number, and thereby substantially reduce the number of resonances in the spectrum. Different mechanisms, such as micro-droplets [181, 183] and high-index prisms [184], have been used to

differentially attenuate modes and clean-up the spectrum, by introducing a localized scattering loss on the BMRs outer surface which preferentially attenuates a subset of the bottle modes and results in substantial spectral "cleaning-up". However, these techniques are cumbersome, not accurately controlled and difficult to apply in practical systems.

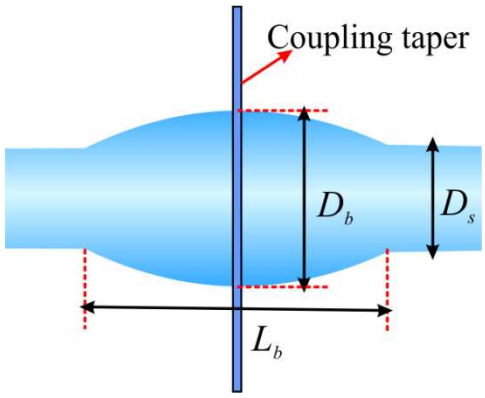

Figure 5-1 Geometry of bottleneck microresonator (BMR).

In the next sections, the number of resonances in the BMR spectrum is reduced by inscribing microgroove scars on the BMR surface with FIB milling. The introduction of this localized damage ("scar") on the BMR surface preferentially attenuates a subset of modes and results in substantial reduction of the number of spectral resonances. Due to the high precision of FIB, the microgroove shape and size can be controlled resulting in precise mode selection.

5.2 Optical bottleneck microresonators (BMRs) nanostructuring

High-*Q* double-necked BMRs were manufactured using the "soften-and-compress" technique already presented in literature [177-181] using a standard fibre fusion splicer. Fibre splicing is a mechano-thermal process in which the cleaved fibre ends are pushed towards each other while heating the fibre ends to a temperature at which they soften and fuse together. The heating is performed in two ways, either by resistive coil (filament) heating or arc discharge. The heating method used in the present study was arc discharge with arc duration just below a second. Multiple short arcs were used in order to

controllably soften the glass. This process can be repeated several times with re-clamping one end of the fibre between stages to release any residual stresses. This results in a robust double-neck BMRs (see Figure 5-2 (a)). The BMR shape is controlled by the softening temperature profile and the applied compression, and defines the resonator spectral characteristics and optical properties. The shape of such resonators can be accurately fitted by a harmonic-oscillator profile [179, 183, 185]. In this work, a standard telecom optical fibre (Corning SMF28) was used to fabricate BMRs. The BMR dimensions were extracted from optical images (see Figure 5-2 (a)) and were estimated to be L_b=350 μm, D_b=170 μm and D_s=125 μm.

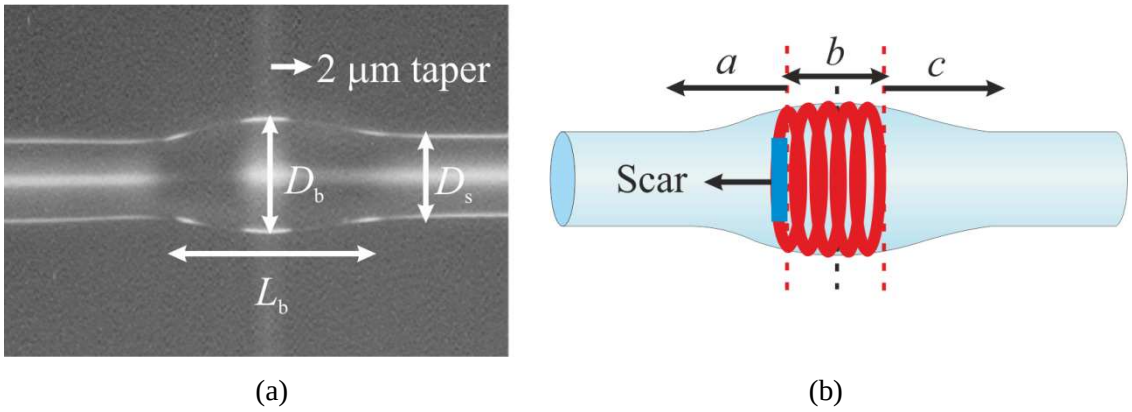

(a) (b)

Figure 5-2 (a) Microscope image of the BMR; (b) schematic of mode selection in a "scarred" BMR. (The BMRs were manufactured by Dr. Ganapathy)

The bottle shape was fitted very well with a truncated harmonic-oscillator profile $R(z) = R_b(1+\Delta k z^2)^{-1/2}$ with Δk a constant (R_b is the bottle radius). For a given polarization, the BMRs modes are characterized by three modal numbers (m, p, q), where $2m$ (m=0,1,2,…) gives the number of field nodes around the circumference, p (p=1,2,…) gives the number of power maxima along the radius, and q (q=0,1,2,…) gives the number of field nodes along the axis of the BMR. In the scalar approximation, the transverse electric field is given by $E(r,\varphi,z)=\Phi(r,z)\Psi(z)\exp(im\varphi)$ [176, 180] , where the radial distribution of the field is given by [186]:

$$\Phi(r,z) = \begin{cases} A_m \dfrac{J_m(U_{mp} r / R(z))}{J_m(U_{mp})} & r \le R(z) \\ A_m \dfrac{K_m(U_{mp} r / R(z))}{K_m(U_{mp})} & r > R(z) \end{cases} \qquad (5\text{-}1)$$

J_m is the Bessel function, K_m is the modified Hankel function and the normalization coefficient A_m is determined such that the boundary conditions are satisfied. In highly multimode fibres, ignoring polarization effects, U_{mp} is approximated by the p^{th} root of the $J_m(U)$ function. U_{mp} can also be approximated by the analytical expression [187, 188]:

$$U_{mp} = m + \alpha_p (m/2)^{1/3} + (3/20)\alpha_p^2 (m/2)^{-1/3} \tag{5-2}$$

where α_p is the p^{th} root of the Airy function (α_p = 2.3381, 4.0879, 5.5205, 6.7867, 7.9441 for p=1,2,3,4,5 respectively). The two aforementioned approximations give almost identical results. In the case of a harmonic oscillator profile, the axial distribution of the field is given analytically by:

$$\Psi(z) = C_{mq} H_q\left(\sqrt{\frac{\Delta E_m}{2}}\, z\right) \exp\left(-\frac{\Delta E_m}{4} z^2\right) \tag{5-3}$$

where the energy levels difference $\Delta E_m = 2U_{mp}\Delta k / R_b$, H_q is the m^{th} order Hermite polynomial and $C_{mq} = [\Delta E_m / (\pi 2^{2q+1} (q!)^2)]^{1/4}$. The axial spreading of each mode is defined by the corresponding turning point, given by [179]:

$$z_c = \pm\left[\frac{4}{\Delta E_m}\left(q + \frac{1}{2}\right)\right]^{1/2} \tag{5-4}$$

measured from the bottle centre. Beyond this point the mode is evanescent. The resonant wavelength for each (m,p,q) mode is given by:

$$\lambda_{mpq} = 2\pi n_0 \left[\left(\frac{U_{mp}}{R_b}\right)^2 + \left(q + \frac{1}{2}\right)\Delta E_m\right]^{-1/2} \tag{5-5}$$

When Δk=0 [$R(z)$=R_b: the case of a cylindrical resonator], Equation (5-5) reduces to the well-known formula $\lambda_{mp} = 2\pi n_0 R_b / U_{mp}$ giving the resonant wavelength of the (m,p) mode supported by a cylindrical resonator of radius R_b.

Based on the calculations [183], it has been shown that microbottle modes with radial mode number p>3 exhibit highly mismatched propagation constants and are not expected to show significant excitation. Only modes with p≤3 can be efficiently phase-matched and substantially excited. For these modes the penetration depth from the BMR surface into the microresonator is less than 6 μm (shown in ref. [183]). Therefore, if scars with depth of ~6 μm are inscribed on the surface of BMRs (see Figure 5-2 (b)) the modes which extend outside the scars (regions *a* and *c* in Figure 5-2 (b)) will experience

extremely high scattering losses and will not survive. Modes, on the other hand, which are localized in the central part (region *b*) will experience minimum losses and will resonate efficiently. The red lines in Figure 5-2 (b) show the survived mode intensity distribution.

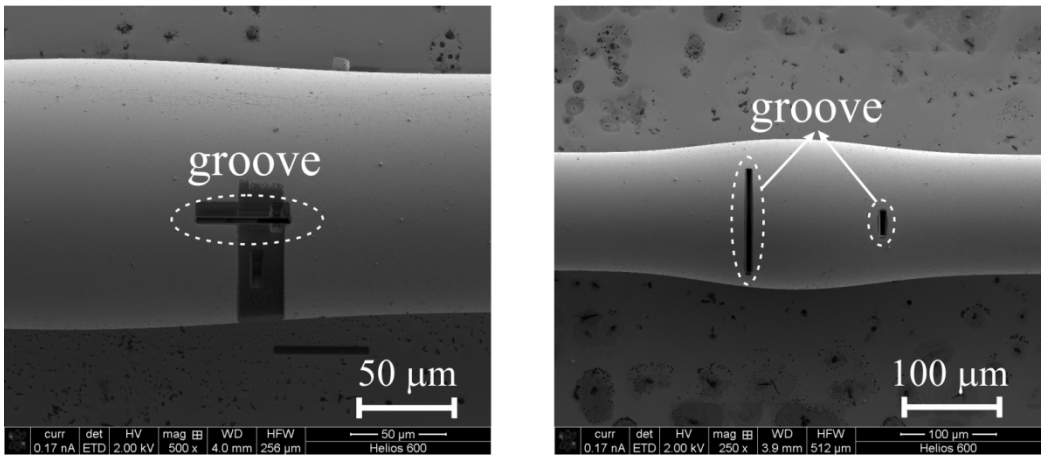

(a) (b)

Figure 5-3 SEM images of microstructured BMRs and the white dashed lines show the grooves: (a) in sample 1 the horizontal groove was 50 µm away from the centre with 5 µm width, 50 µm length and 6 µm depth; (b) in sample 2 the width, length, depth and distance from the centre for the left and right grooves were 5 µm, 109 µm, 6 µm, 50 µm and 5.5 µm, 27.5 µm, 6 µm and 83 µm, respectively.

FIB milling was used to microstructure BMRs. As FIB is a direct writing technique with a beam size frequently smaller than 30 nm, it offers extreme flexibility and allows for high precision in the scar design. We used a FIB system "Helios 600" (FEI Inc., Hillsboro, USA) equipped with gallium ion beam at 30.0 kV accelerating voltage and 2.8 nA current. Figure 5-3 shows SEM images of the gold-coated FIB milled BMRs and the white dashed lines show the grooves. A groove with 50 µm length, 5 µm width and 6 µm depth was carved at 50 µm away from the centre parallel to the BMR axis in sample 1 (shown in Figure 5-3 (a)). In this SEM image, only the horizontal groove contributed predominantly to the mode selection. The rest of the dark region is just the gold removed region and an additional shallow groove. In sample 2 (Figure 5-3 (b)), two scars were milled perpendicularly to the resonator axis and placed asymmetrically with respect to the BMR centre. The left groove is 5 µm wide, 109 µm long and 6 µm deep and was placed 50 µm away from the BMR centre; the right groove is 5.5 µm wide, 27.5 µm long and 6 µm deep and positioned

83 μm away from the centre. The gold coating was removed by gold-etching solvent which contains iodine and potassium iodine after FIB milling was completed.

5.3 Characterization

In order to spectrally characterize the resonators, micro-positioning stages were used to place a ~2 μm diameter fibre taper at various positions along the BMR (shown in Figure 5-1). The fibre taper was in contact with the BMR and was perpendicular to its axis. Although this overloads the cavity and reduces the *Q*, it results in a robust and stable arrangement. Light from a tuneable laser with linewidth of 100 kHz (Agilent 81600B) was launched into the fibre taper and coupled into the BMR evanescently. The output of the fibre taper was monitored by an InGaAs detector.

Figure 5-4 shows the fibre taper transmission spectra of sample 1 for different fibre taper positions. Resonance spectra of the pristine BMR were measured first for reference and comparison. Before FIB milling, rich and dense spectral characteristics were observed (see Figure 5-4 (a)). Resonances with *Q* between 10^6 and 10^7 were observed when the fibre taper was positioned at the centre of the microresonator. Figure 5-4 (b-f) show the corresponding spectra for sample 1 after FIB microstructuring when the fibre taper was placed at the centre and 30 μm, 50 μm, 60 μm, 120 μm off-centre, respectively. The white line on the SEM image at the right side of each spectrum shows the position of the fibre taper. The cleaned-up spectra consist of a sub-set of modes which occupy the central part of the bottle and therefore do not suffer significant scar-induced scattering losses and experience only a small deterioration in their *Q*. As the taper is moved closer to the scar position, both the resonance and the *Q* factor decrease. Modes, on the other hand, which overlap or extend beyond the FIB grooves experience severe scattering losses and are not excited. When the fibre taper was placed beyond the scar position all transmission resonances disappeared (Figure 5-4 (e-f)). In this case no mode can tunnel through the 50 μm long scar and no resonance survives.

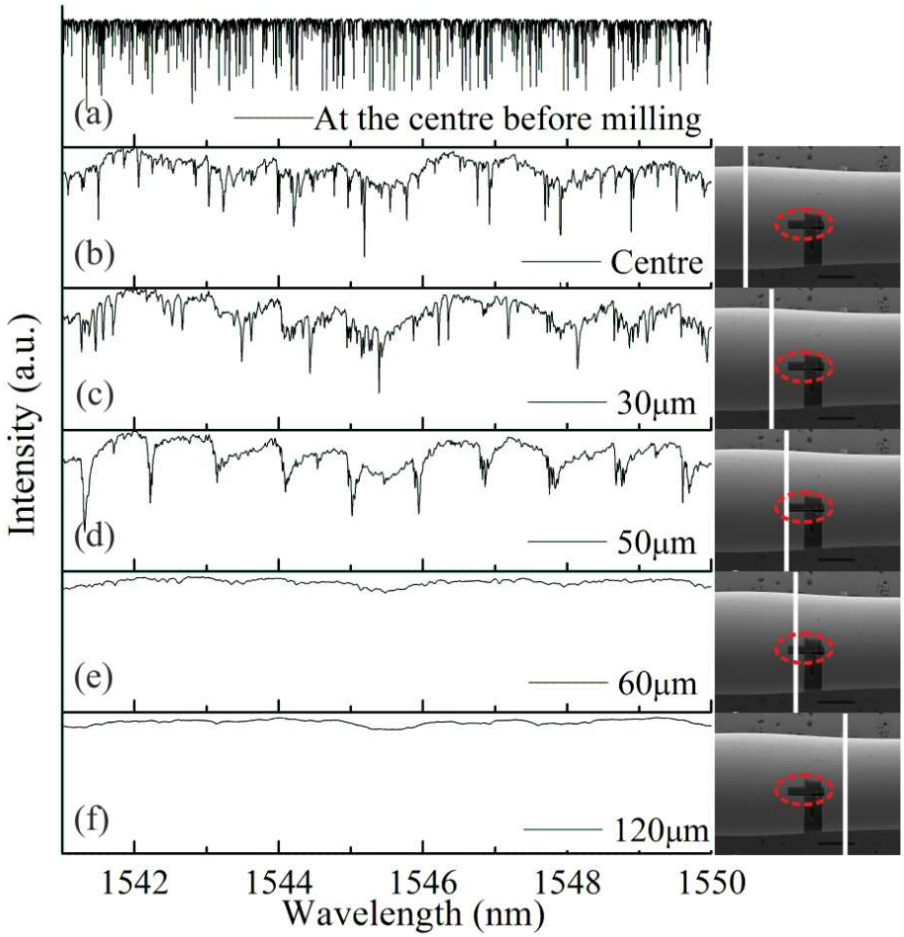

Figure 5-4 Transmission spectra of the taper-coupled BMRs (sample 1). (a) Before scarring with the taper at the microresonator centre; (b-f) after scarring with the taper at the centre and 30 μm, 50 μm, 60 μm 120 μm off-centre, respectively. The white lines on the SEM images on the right show the position of the fibre taper with respect to the scar and the red dash lines show the groove position. (The characterization data was collected by Dr. Ganapathy.)

Figure 5-5 shows similar characterization results for sample 2. Again, the white line on the SEM image at right side of each spectrum shows the position of the fibre taper. The presence of the two perpendicular scars results in substantial spectral clean-up when the excitation fibre taper lies in the central region, defined in this case by the scar closer to the centre (Figure 5-5 (b-d)). Outside this region, resonances again disappear (Figure 5-5 (e)). However, quite unexpectedly, when the taper was placed 120 μm away from the centre, sharp and well defined resonances re-appeared (see Figure 5-5 (f)). This is a particular feature of the two asymmetrically placed perpendicular scars of sample 2 and were not observed in the case of the long longitudinal groove of sample 1 (see Figure 5-4) or the diffractive localized loss of Ref.[181].

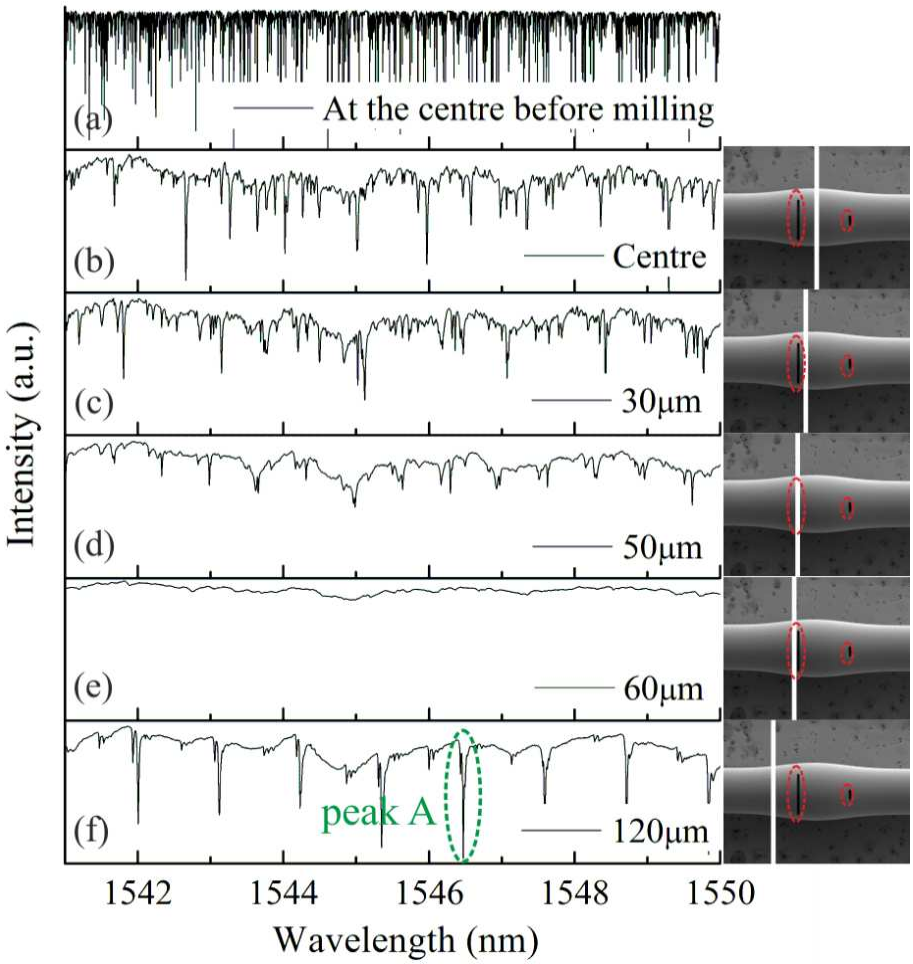

Figure 5-5 Transmission spectra of the taper-coupled BMRs (sample 2) (a) before scarring with the taper at the microresonator centre; (b-f) after scarring with the taper at the centre and 30 μm, 50 μm, 60 μm 120 μm off-centre, respectively. The peak A in (f) is analysed in Section 5.4. The white lines on the SEM images on the right show the position of the microfibre with respect to the scar and the red dash lines show the grooves position. (The characterization data was collected by Dr. Ganapathy.)

5.4 Analysis

Figure 5-6 shows a close-up of one of the resonances (peak A) in Figure 5-5 (f) fitted with a number of Lorentzian lines. This demonstrates that each spectral feature corresponds to the excitation of a small number of closely packed eigenmodes.

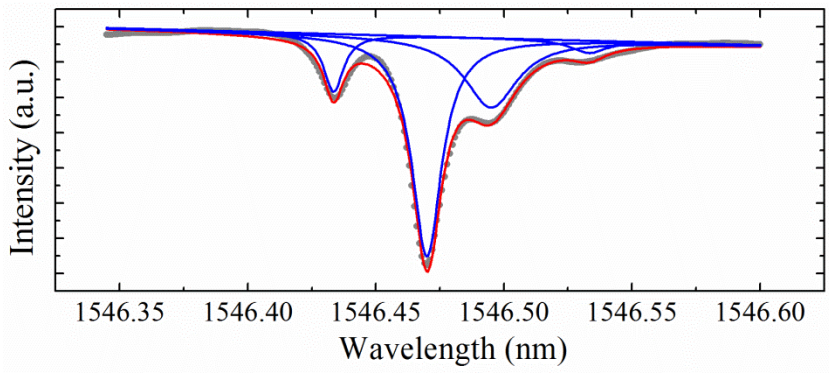

Figure 5-6 Lorentzian line fitting of a resonance (peak A) in Figure 5-5 (f). Red line is one of the resonances in Figure 5-5 (f) and blue lines are Lorentzian fitting lines.

Figure 5-7 shows the intensity distribution of the two individual contributing eigenmodes [183]. These two modes have the same azimuthal mode number and axial mode numbers differing by 5. Individual modes show standing-wave patterns with low-intensity nodes extending over ~500 nm and, therefore, overlap strongly with the 5 μm wide scar and scatter out.

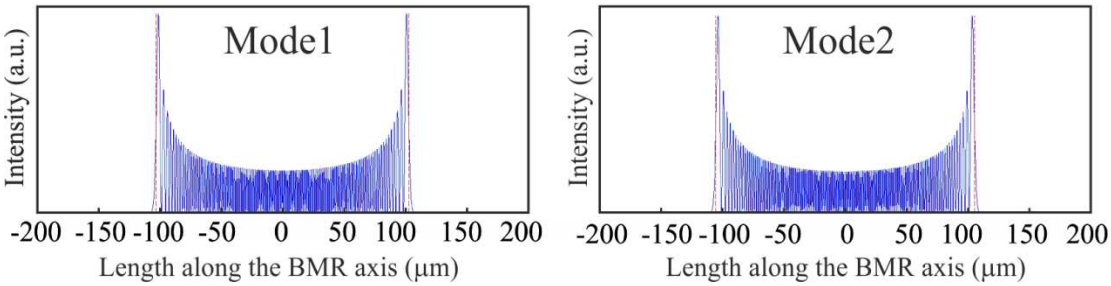

Figure 5-7 The intensity distributions of the two individual modes having the same azimuthal mode number and axial mode numbers differing by 5.

The intensity distribution along the BMR length when two bottle eigenmodes are excited simultaneously is shown in Figure 5-8. When modes combine and beat together the standing-wave patterns show intensity minima over regions in excess of 5 μm in two places along the resonator length (Figure 5-8 insets). When these minima coincide with the scars, the effects of the scattering loss are minimized and sharp resonances, corresponding to the surviving low-loss modes, re-appear. These resonators show cleaned-up spectra with extremely large free spectral range and can be very useful in sensing applications. It is predicted that finer grooves can reduce further the residual scattering losses and improve the *Q* factor of the milled BMRs. For

individual modes to survive, scars with thickness <500 nm should be employed.

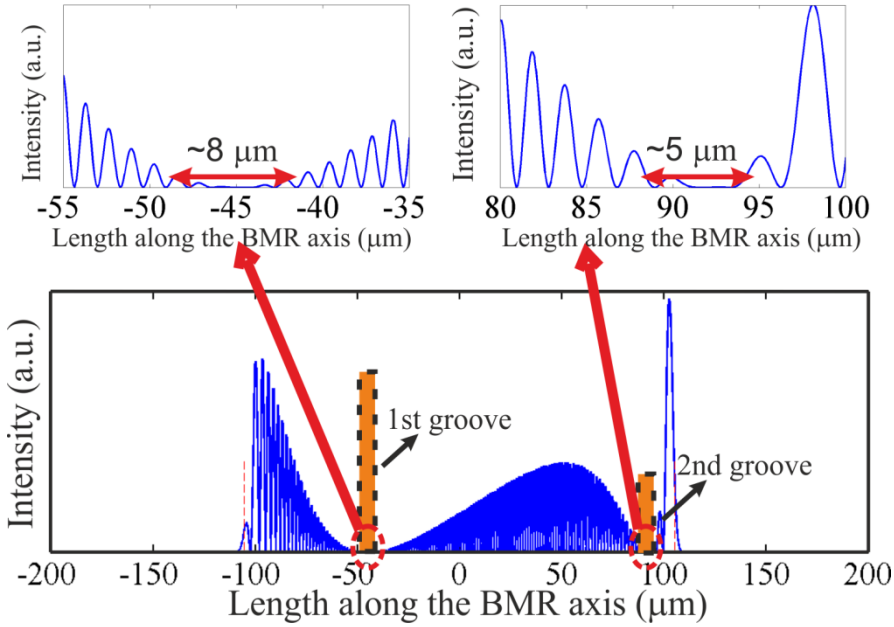

Figure 5-8 Intensity distribution along the BMR axis when two modes are excited simultaneously (the insets show the intensity distributions in two intensity minima regions).

5.5 Conclusions

In conclusion, an efficient, controllable and repeatable method to select WGMs in BMRs was presented. This method exploited FIB milling to scar the BMR surface with high precision. Modes overlapping with the milled grooves experience high losses and disappear, while modes in the bottle central part can survive and resonate efficiently. A single high-*Q* mode was predominantly selected using two asymmetrical perpendicular scars. By placing the grooves closer to the BMR centre, only the modes with resonance in the bottle centre can be excited and truly single mode operation can be achieved. The shapes and positions of the milled grooves can be chosen according to the application and the performance of microstructured BMRs can be further improved by optimizing the scar shape, size and orientation. This technique can also be employed to clean-up spectra in other types of non-spherical micro-resonators [55].

Chapter 6 Plasmonic slot nano-resonator embedded in metal-coated optical fibre tapers

> There is no use trying, said Alice; one can't believe impossible things. I dare say you haven't had much practice, said the Queen. When I was your age, I always did it for half an hour a day. Why, sometimes I've believed as many as six impossible things before breakfast.
>
> Lewis Carroll

In this chapter, *Plasmonic Slot Nanoresonators* (PSNRs) embedded in a gold-coated optical fibre taper are studied. Light is coupled from the plasmonic waveguide into the PSNR, showing strong localization in three dimensions. Single bow-tie and rectangular PSNRs, as well as cascaded multiple bow-tie PSNRs in gold-coated microfibres have been considered numerically. The intensity enhancement (in excess of 10^6) and the resonance wavelength depend on both the PSNR and microfibre dimensions. A rectangular PSNR in a gold-coated optical fibre tip was both simulated and realised in experiments. The PSNRs embedded in plasmonic optical fibre tapers could find applications in *Surface-Enhanced Raman Scattering* (SERS), optical filtering, bio-sensing and spectroscopy.

M. Ding, M. N. Zervas, and G. Brambilla, "Transverse excitation of plasmonic slot nano-resonators embedded in metal-coated microfiber tips," *Appl. Phys. Lett.* **102**, 141110 (2013).

6.1 Background

In recent years, research in plasmonics and *Surface Plasmon Polaritons* (SPPs) has attracted considerable interest. SPPs have been extensively studied in a number of structures, such as single metal/dielectric interfaces [189], thin dielectric-metal-dielectric [190-192], or metal-dielectric-metal films and integrated-optics waveguides [193] as well as cylindrical structures [194-196]. They support a number of different types of symmetric and anti-symmetric bound and leaky modes. The propagation characteristics and field distributions of these modes depend on the geometry and physical properties of the noble metal and the surrounding dielectrics. Since SPPs do not experience diffraction in the micrometres region, they can confine energy to spot sizes considerably smaller than the excitation light wavelength. As a result, they have found a multitude of applications based on their localized nature, ranging from highly-integrated photonic circuits [197, 198], optical data storage [199], lithography, microscopy, SERS or spectroscopy, and bio-photonics [200] . SPPs have also been utilized in metal-coated fibre tapers for sensing [201, 202] and sub-wavelength light confinement [203, 204].

In addition, nanoscale apertures in thin noble-metal films, with dimensions comparable to the light wavelength, can form *Plasmonic Nano-Resonators* (PNRs) and show astonishing optical properties leading to enhanced and selective light transmission and confinement. At resonance, such structures can concentrate an incident light field into a small volume with orders-of-magnitude intensity enhancement. In contrast to conventional optical systems using lenses and mirrors, PNRs can provide hot spots in the near-field with dimensions determined mainly by the structure size rather than by the diffraction limit. A number of different nano-structures have been considered and studied in detail for their ability to concentrate light. These include circular, square, rectangular, bow-tie, as well as, L-, C- and H-shaped nano-structures [205]. So far, the transmission and field-enhancement properties of these nano-resonators have been studied primarily under plane-wave excitation in 2D arrangements. When such shapes are formed in thin metal films, they form PSNRs, also called nano-antennas, showing strong 3D light concentration and rich resonance effects [206, 207]. Again, so far, the transmission

properties of slot nano-resonators have been studied under plane-wave excitation directed perpendicularly to the plane of the resonator [56, 57]. Planar 2D PNRs can also be coupled to planar waveguides and can be excited evanescently to control the transmission and reflection response [208, 209].

In Section 6.2, we study theoretically a strongly-coupled 3D *plasmonic slot nanoresonator* (PSNR) by embedding a slot nano-cavity in a plasmonic cylindrical waveguide formed by a thin-metal-film coated microfibre. Light is launched from one end of the microfibre and the various resonances can be identified simply monitoring the transmitted and reflected light. The optical properties for different dimensions and shapes of the PSNR have been analysed and the results can be used for the PSNR design and optimization. Section 6.2.1 presents the modelling of bow-tie and rectangular PSNRs embedded in cylindrical plasmonic waveguides and analyses the nature of the observed resonances, under orthogonal polarization excitation. Section 6.2.2 explores the resonance wavelength and intensity enhancement dependence on the geometry of the embedded PSNRs. Section 6.2.3 discusses the resonance characteristics and intensity enhancement in cascades of multiple bow-tie PSNRs.

In Section 6.3, for the first time, both theoretically and experimentally, the transverse excitation of a strongly-coupled 3D PSNR is investigated by embedding a rectangular slot nano-cavity in a plasmonic structure formed by a thin-metal-film coated optical fibre tip.

6.2 Numerical simulations of PSNR embedded in metal-coated optical microfibres

6.2.1 Modelling of PSNR embedded in cylindrical plasmonic waveguides

Theoretical analysis was carried out using a 3D finite element method by the commercial software COMSOL 4.1 Multiphysics. Figure 6-1 shows the structure used for the modelling. Firstly, a gold-coated plasmonic microfibre was simulated to provide a transmission and reflection reference. A cylindrical fused-silica waveguide with 1 μm diameter was coated with 30 nm layer of

gold. The dispersion of gold's real and imaginary parts of the refractive index is taken into account [115]. The waveguide was surrounded by air in a box sufficiently large to avoid reflections from the boundaries (Figure 6-1 (a)). The chosen boundary conditions were: port boundary at the input and output, scattering boundary condition for the exterior boundary and continuity boundary condition for the interior boundary (the definition of boundary conditions are introduced in Appendix A). Light was launched from the input using boundary mode analysis. In order to save memory and reduce the calculation time, half of the structure was calculated since the geometry is symmetric with respect to the *y*-*z* plane (Figure 6-1 (b)). The separatrix is set as a perfect electric boundary. In this case, the polarization of the launched light is along the *x* direction. Simulations were run with a controlled mesh size (80 nm in silica, 8 nm in gold coating and 100 nm in surrounding air) to make efficient use of computer memory.

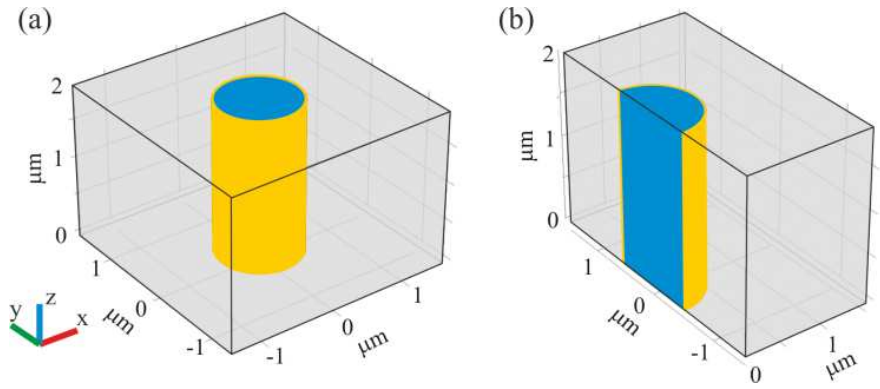

Figure 6-1 (a) Geometry of the modelled gold-coated plasmonic microfibre (the blue domain is silica, the yellow domain is gold and the grey domain is air); (b) half of the gold-coated plasmonic microfibre geometry.

Transmissivity and reflectivity were calculated using the *S*-parameter in COMSOL the same as used in Section 3.2.3. The transmissivity of the plasmonics microfibre in the wavelength range from 600 nm to 2200 nm is presented in Figure 6-2. At wavelength λ~700 nm, the transmissivity experiences a sudden drop because the hybrid second order mode is excited in the microfibre and experiences higher losses [195]. From λ~700 nm to λ~2000 nm, the lowest order hybrid plasmonic mode is guided in the gold-coated microfibre. When the wavelength is above 2000 nm, the lowest order hybrid plasmonic mode goes through the cut-off, the power leaks out and the

transmissivity decreases quickly [194, 196]. Therefore, for the rest of the investigation wavelengths in the range 800 nm-2000 nm are selected to ensure single mode operation and strong guidance.

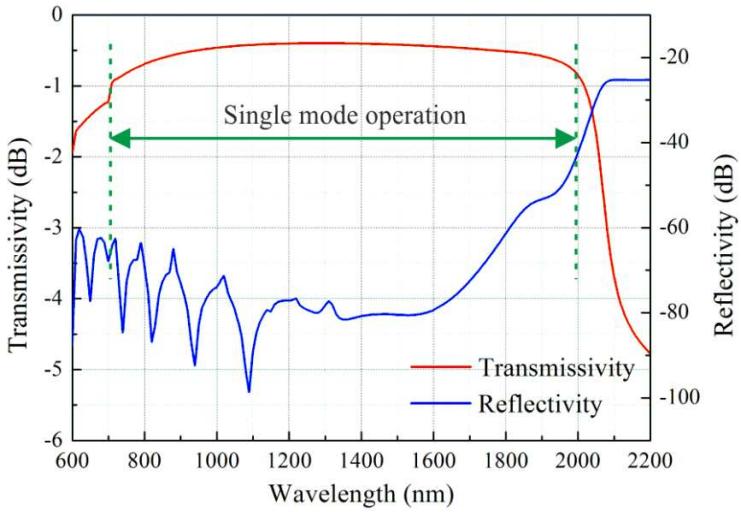

Figure 6-2 Transmissivity and reflectivity of the gold-coated plasmonic microfibre without PSNR. Microfibre diameter and gold film thickness are D=1 μm and t=30 nm, respectively.

Figure 6-3 (a) shows the x component of the electric field (E_x) distribution of the lowest order hybrid plasmonic mode when x-polarized light is launched at the input end at λ=1500 nm. As expected, the strongest plasmonic field localization is observed at point A (and its diametric opposite). The plasmonic mode shows an antisymmetric E_x distribution. Figure 6-3 (b) on the other hand shows the E_y field distribution of the lowest order hybrid plasmonic mode under y polarization initial excitation. In this case the plasmonic localization is observed in points B and C.

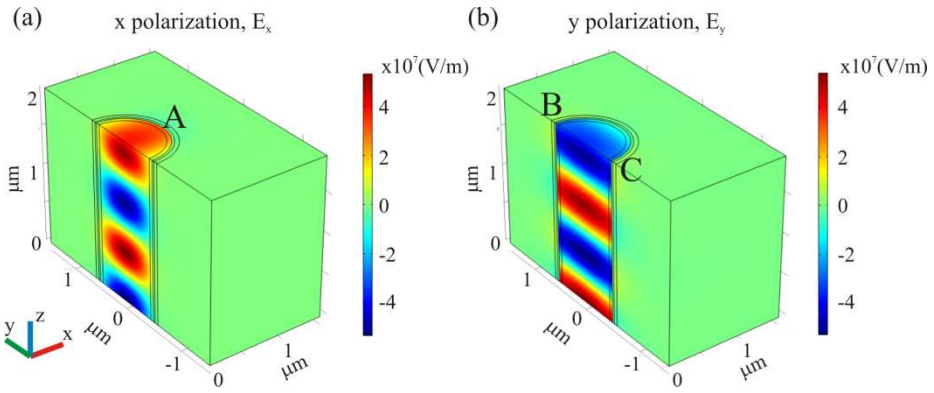

Figure 6-3 (a) x component of the electric field E_x when the launched light is along the x polarization; (b) y component of the electric field E_y when the launched light is along the y polarization. The wavelength is λ=1500 nm.

In order to investigate the resulting intensity enhancement, a plasmonic slot nano-cavity was embedded on the side of the cylindrical plasmonic waveguide (see Figure 6-4 (a)). Figure 6-4 (b) and (c) give the top-view of the two PSNRs considered in this study, namely a bow-tie nano-cavity with L_R length, D_R width and d_R waist width and a rectangular slot nanocavity with dimensions D_R and L_R. The depth of the slot nanocavities is equal to the thickness (t) of the plasmonic waveguide gold layer, which in all calculations was taken as t=30 nm.

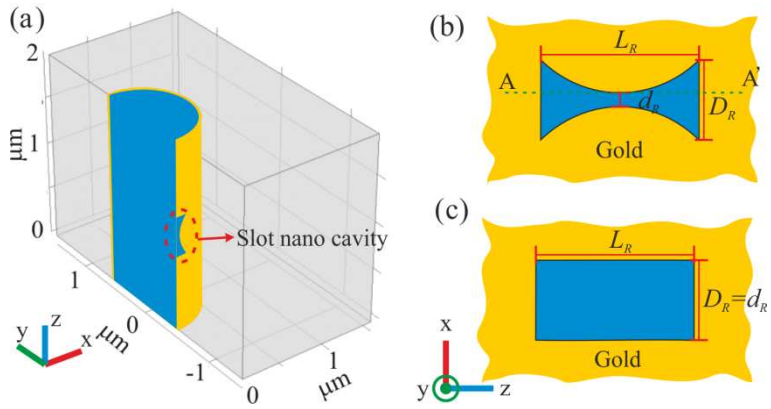

Figure 6-4 (a) Geometry of the PSNR embedded in the plasmonic microfibre; top-view of (b) the bow-tie and (c) the rectangular plasmonic slot nanocavities. L_R, D_R and d_R are the length, width and waist width of the nano-cavity, respectively.

6.2.1.1 Bow-Tie PSNR

Figure 6-5 shows the transmissivity and the reflectivity of the composite structure with the bow-tie PSNR geometry with L_R=400 nm, D_R=200 nm, and d_R=34.3 nm when x-polarized light is launched. There are several dips observed in the transmission spectrum and associated peaks in the reflection spectrum, corresponding to different type of resonances of the embedded PSNR. Three main resonances were identified, corresponding to the most prominent reflection peaks at λ=880 nm, 1524 nm and 2050 nm. The resonance at λ=880 nm corresponds to a second order resonance, with two intensity maxima along the length of the bow-tie PSNR (resonance II). The resonances at λ= 1524 nm (resonance IA) and λ= 2050 nm (resonance IB), on the other hand, correspond to first order PSNR resonances, with only one intensity maximum along the bow-tie length. As will be discussed further in Section 6.2.1.2, resonances IA and IB show different resonant behaviour in the

plane perpendicular to the propagation (z) axis, indicating that the observed resonances belong to the composite (plasmonic waveguide + resonator) structure. Resonance IB shows a stronger transmission dip and reflection peak because of the longer wavelength, which gives stronger plasmonic waveguide/resonator interaction. In addition, it corresponds to a wavelength closer to the plasmonic waveguide cut-off showing reduced group velocity and increased interaction.

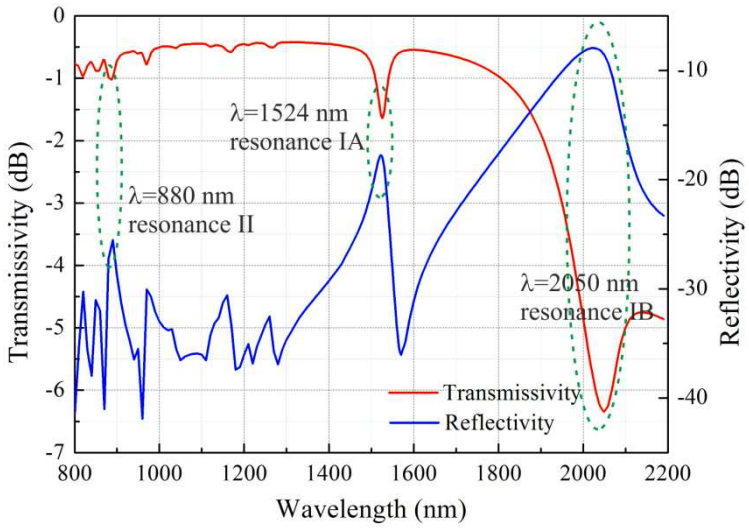

Figure 6-5 Transmissivity (red) and reflectivity (blue) of the bow-tie PSNR presented in Figure 6-4 (b) embedded in the plasmonics microfibre when x-polarized light is launched. Microfibre diameter, gold film thickness, bow-tie PSNR length, width and waist width are assumed to be D=1 μm, t=30 nm, L_R=400 nm, D_R=200 nm and d_R=34.3 nm, respectively.

Figure 6-6 shows the total electric field modulus ($|E|$) at several wavelengths corresponding to the major (λ=880 nm, 1524 nm and 2050 nm) resonances, as well as some minor (λ=820 nm, 970 nm, 1040 nm, 1170 nm and 1260 nm) resonances. The intensity is plotted on a plane tangential to the top resonator surface. At the major resonances, the electric field is highly localized and symmetric around centre at the bow-tie waist. At the minor resonances, the corresponding electric field distributions are gradually shifting off-centre and their peak values decrease.

Figure 6-7 shows the various electric field components and their modulus at resonances II and IA at the top-surface tangential x-z plane. Resonance IB shows similar characteristics to IA. The E_x and E_y field components, associated with the flow of surface currents, are about one order of magnitude larger than the perpendicular component E_z.

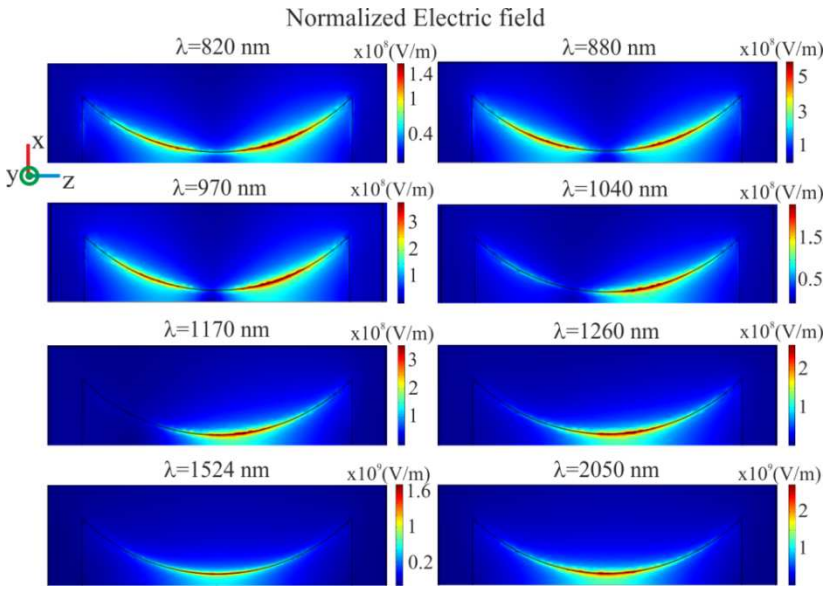

Figure 6-6 Normalized electric field on *x-z* plane for bow-tie PSNR at different wavelengths λ. Microfibre diameter D=1 μm, gold film thickness t=30 nm, bow-tie PSNR length L_R=400 nm, width D_R=200 nm, and waist width d_R=34.3 nm.

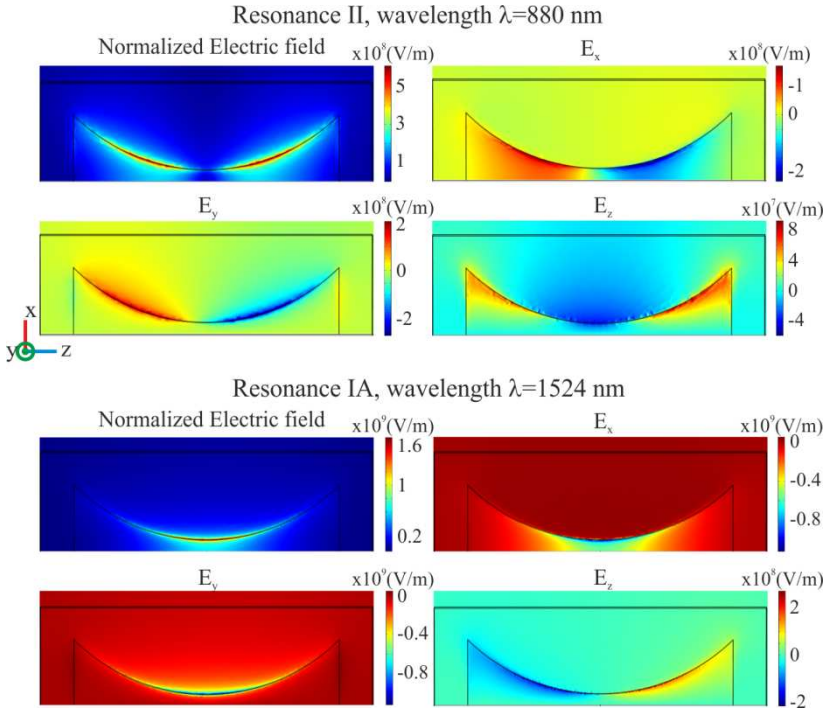

Figure 6-7 Electric field modulus and components for bow-tie PSNR on *x-z* plane at resonance II (λ=880 nm – top four images) and resonance IA (λ=1524 nm - bottom four images). Microfibre diameter D=1 μm, gold film thickness t=30 nm, bow-tie PSNR length L_R=400 nm, width D_R=200 nm, and waist width d_R=34.3 nm.

Figure 6-8 (b) shows the electric field modulus and corresponding field components over the *y-z* plane tangential to the bow-tie waist inner side (along

AA' in Figure 6-4 (b) and shown in Figure 6-8 (a) with green color plane), for resonances II and IA. In both cases, the electric field modulus peaks at the two thin gold-film interfaces, as expected in a plasmonic waveguide. The distribution of the E_y field component shows the characteristics of an antisymmetric-bound SPP [196].

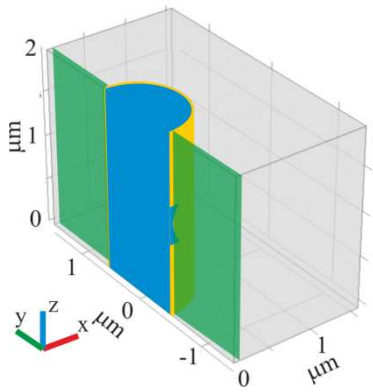

(a)

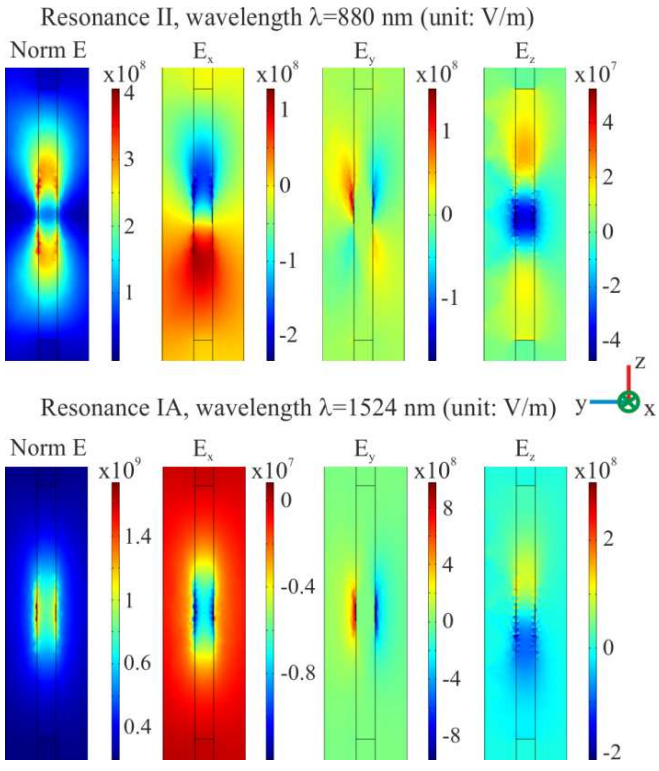

(b)

Figure 6-8 (a) Geometry of the bow-tie PSNR embedded in the plasmonic microfibre, in which the green plane presents the position of electric field in (b); (b) Normalized electric field modulus and its three components for bow-tie PSNR on *y*-*z* plane at λ=880 nm and λ=1524 nm. Microfibre diameter D=1 μm, gold film thickness t=30 nm, bow-tie PSNR length L_R=400 nm, width D_R=200 nm, and waist width d_R=34.3 nm.

Finally, Figure 6-9 shows the electric field modulus and corresponding field components over the *x*-*y* plane (shown in Figure 6-9 (b) with green color plane) at the edge of the bow-tie cavity, again for resonances II and IA. For both resonances, strong field localization is observed at the sharp edges of the bow-tie resonator.

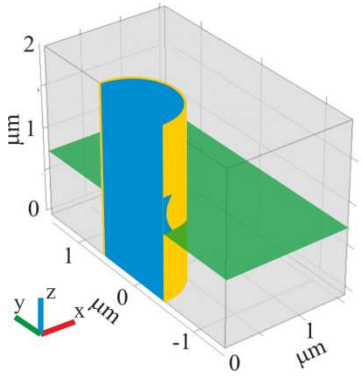

(a)

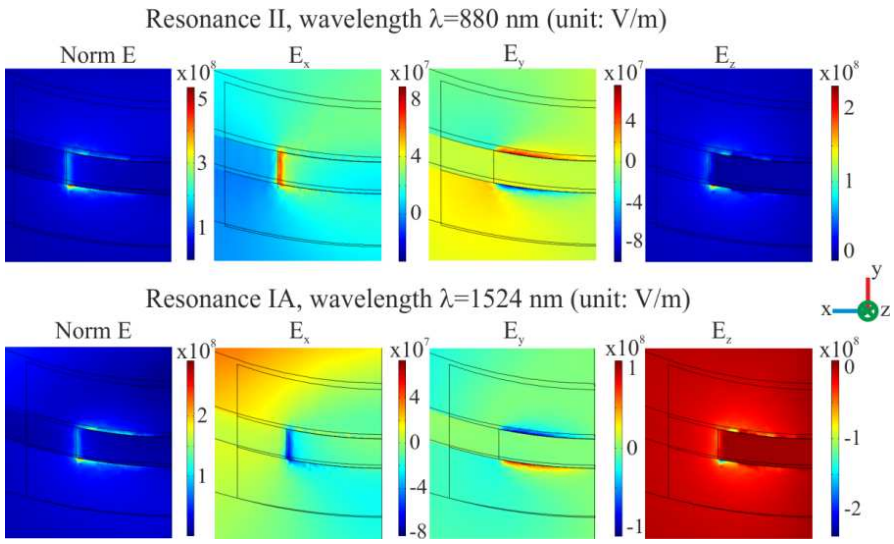

(b)

Figure 6-9 (a) Geometry of the bow-tie PSNR embedded in the plasmonic microfibre, in which the green plane presents the position of electric field in (b); (b) The normalized electric field modulus and its components for the bow-tie PSNR on the *x*-*y* plane at λ=880 nm (top four) and λ=1524 nm (bottom four).

The intensity enhancement factor, defined as the intensity I at the point of maximum field localization, in the presence of the PSNR, divided by the intensity I_0 at the same position without the PSNR, namely:

$$E_f = \frac{I}{I_0} = \frac{|E|^2}{|E_0|^2} \tag{6-1}$$

has been calculated at the major resonances IB, IA and II, and resulted to be 9.65×10^5, 2.5×10^5 and 4.7×10^4, respectively.

6.2.1.2 Rectangular PSNR

Figure 6-10 shows the transmissivity and reflectivity spectra for a rectangular resonator with L_R=400 nm and D_R=34.3 nm. The spectra show similar characteristics with the bow-tie resonator. Figure 6-11 shows the electric field modulus and the corresponding three components at resonance II, IA and IB at the top-surface tangential *x*-*z* plane. The field distribution characteristics are similar to those observed in the bow-tie case (Figure 6-7). Here resonance II takes place at λ= 900 nm and shows two-intensity maxima along the resonator length. Resonances IA and IB, on the other hand, occur at λ=1500 nm and 1780 nm, respectively, and show only one intensity maximum. Other features are also similar to those shown in Figure 6-8 and Figure 6-9.

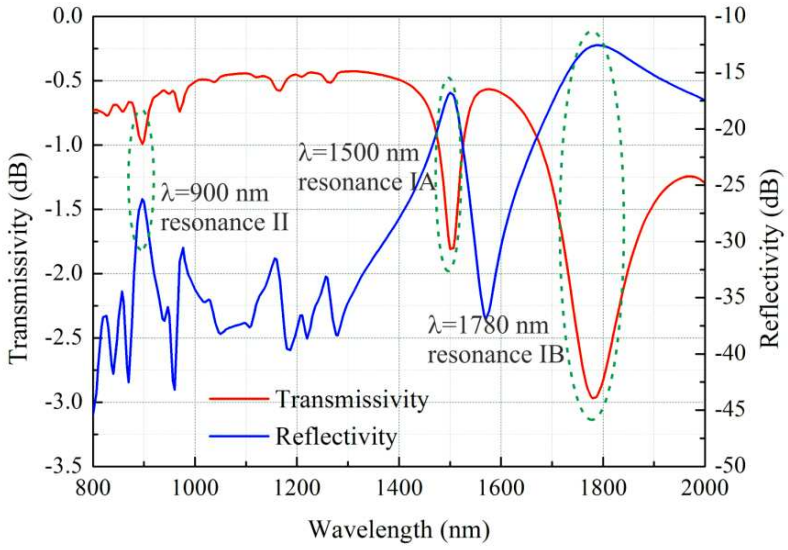

Figure 6-10 Transmissivity (red) and reflectivity (blue) of the rectangular PSNR shown in Figure 6-4 (c) embedded in the plasmonics microfibre. Microfibre diameter D=1 μm, gold film thickness t=30 nm, rectangular PSNR length L_R=400 nm, width D_R=34.3 nm.

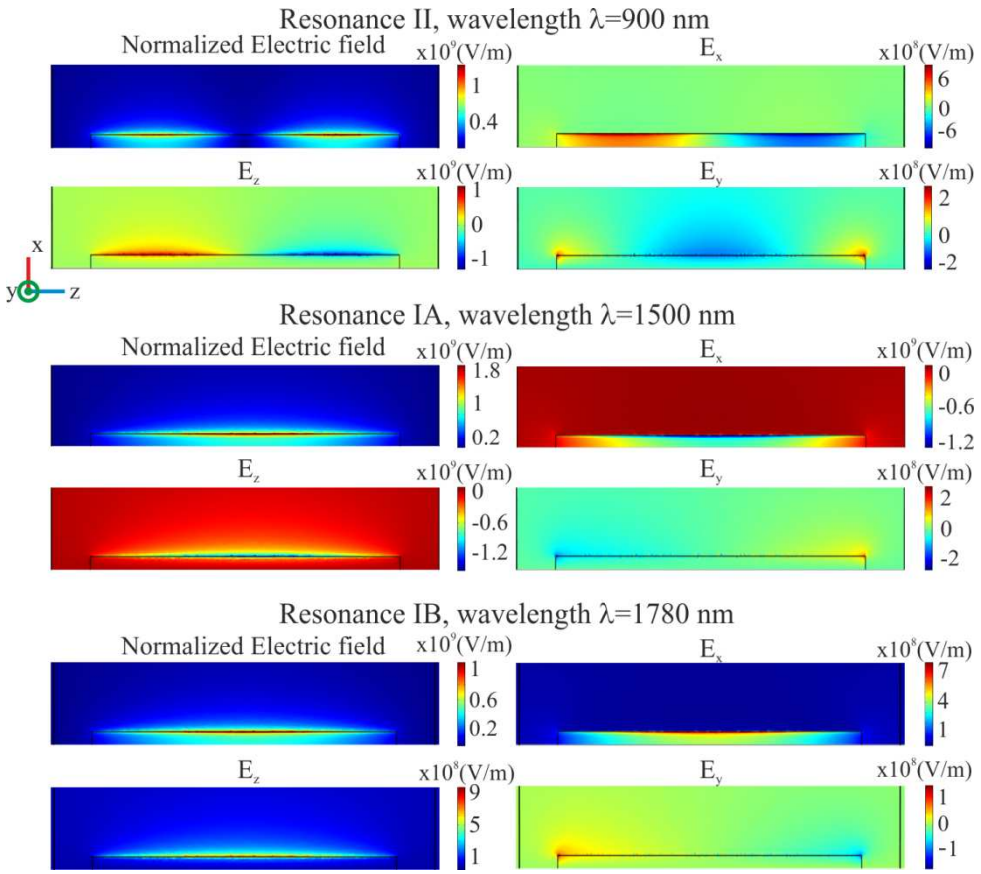

Figure 6-11 Electric field modulus and three components on the *x-z* plane for resonance II (λ=900 nm), resonance IA (λ=1500 nm) and resonance IB (λ=1780 nm), for the rectangular PSNR of Figure 6-4 (c) (L_R=400 nm and D_R=34.3 nm) engraved in the plasmonic microfibre.

Figure 6-12 shows 3D plots of the *x* component of the electric field (E_x) distribution (left) and over the *x-y* plane cross section through the resonator centre (right), for resonance II at λ=900 nm (top), resonance IA at λ=1500 nm (middle) and IB at λ=1780 nm (bottom). As already mentioned in the previous section, although resonances IA and IB show the same field distributions over the resonator top surface, they are characterized by different distributions in the transverse cross section over the nano-resonator area. Resonance IA shows a second order transverse resonance over the cylindrical waveguide cross section, while resonance IB is characterized by a first order resonance. In all resonance cases, the maximum intensity occurs in the resonator area. The E_x field distributions over the centre cross sections (Figure 6-12 – right column) show the characteristic dipole shapes associated with nano-antennas. It is this nano-antenna radiation that contributes to the transverse resonances and distorts the waveguide propagating fields shown in Figure 6-12 – left column.

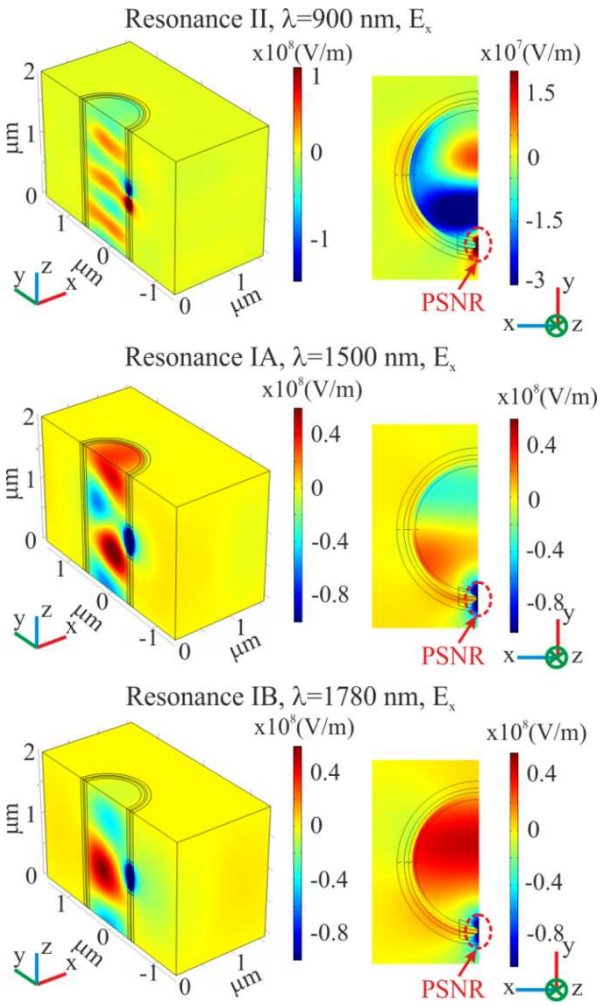

Figure 6-12 3D plots of the electric field *x* component (E_x) distribution (left column) and over the *x-y* plane cross section through the resonator centre (right column), for resonance II at λ=900 nm (top), resonance IA at λ=1500 nm (middle) and IB at λ=1780 nm (bottom). The rectangular PSNR has L_R=400 nm and D_R=34.3 nm.

Compared with the bow-tie PSNR, this rectangular geometry shows higher enhancement factor of E_f= 4.7×10^5 for resonance IA which is about two times bigger than that observed in the bow-tie PSNR (2.5×10^5). Hence, rectangular PSNR has better performance in this case. Also, experimentally, the rectangular PSNR is much easier to fabricate.

6.2.2 *Simulation results and analysis of single PSNR*

In this section, the two basic PSNR shapes presented above were further studied by varying their geometrical dimensions. The main resonant wavelength shifts and the associated intensity enhancement factors were calculated. Resonance and enhancement factors in multiple, concatenated bow-tie resonators have also been considered.

6.2.2.1 Bow-tie PSNRs with different waist and fixed edge width

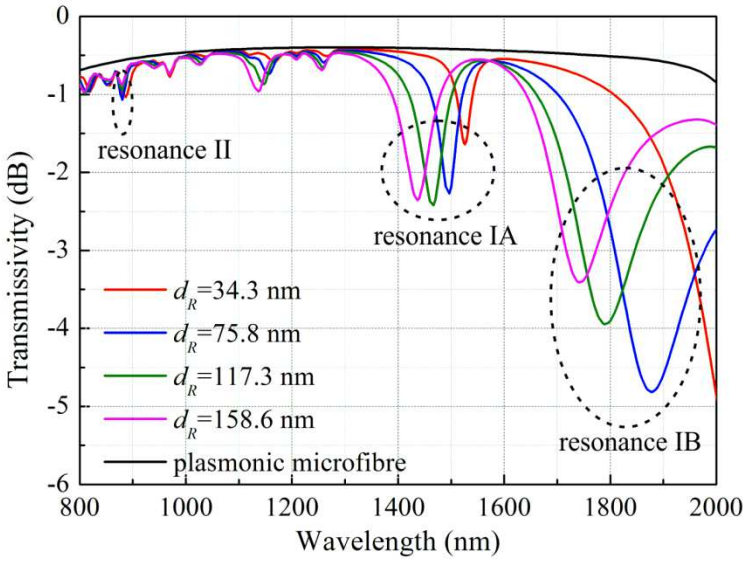

Figure 6-13 Transmissivity of the bow-tie PSNR for different waist-width d_R. D_R=200 nm and L_R=400 nm. The red, blue, green and pink lines represent different waist widths d_R=34.3 nm, 75.8 nm, 117.3 nm and 158.6 nm, respectively. The black line is the reference plasmonic microfibre.

The dependence of bow-tie PSNR's optical properties on the waist width (d_R) has been investigated for constant edge width D_R=200 nm, length L_R=400 nm and metal film thickness t=30 nm and varying waist widths. Figure 6-13 shows the resulting transmissivity for waist width d_R of 34.3 nm, 75.8 nm, 117.3 nm and 158.6 nm. The transmissivity of the plasmonic microfibre without the nano-cavity is also shown as a reference. As above, the first order resonances IA and IB lie in the wavelength regions of 1440-1524 nm and 1700-2050 nm, respectively, while the second order resonance II occurs at ~880 nm. When the waist width d_R increases, the resonance wavelengths for resonances IA and IB shift to shorter wavelengths. The enhancement factor E_f at d_R= 34.3 nm, 75.8 nm, 117.3 nm and 158.6 nm are 2.5×10^5, 2.15×10^5, 7.56×10^4, and 3.1×10^4 for resonances IA, and 9.65×10^5, 4.04×10^5, 9.15×10^4, and 3.15×10^4 for resonances IB. The corresponding intensity enhancement factors for resonances II are 4.7×10^4, 3.33×10^4, 1.26×10^4, and 5.2×10^3. In addition to intensity enhancement changes, the bow-tie waist width controls the position of the resonance IA and IB wavelengths. This can be beneficial if fine-tuning of the resonant wavelength is required. The wavelength of resonances II, on the other hand, seems to be relatively insensitive to bow-tie waist width changes.

6.2.2.2 Bow-tie PSNRs with fixed waist and different edge width

The resonance dependence on the PSNR width D_R is calculated and plotted in Figure 6-14 for constant waist width d_R=34.3 nm and length L_R=400 nm. The intensity enhancement factors for resonance II are 4.29×10^4, 4.70×10^4, 4.73×10^4 for D_R=100 nm, 200 nm and 300 nm, respectively. The corresponding factors for resonance IA are 3.31×10^5, 2.50×10^5, and 1.84×10^5. For resonance IB the intensity enhancement factor increases from 9.06×10^5 to 9.65×10^5 as D_R changes from 100 nm to 200 nm. Although changing D_R has negligible effect on resonance II and IA wavelengths, it has a more pronounced effect on the wavelength of resonance IB.

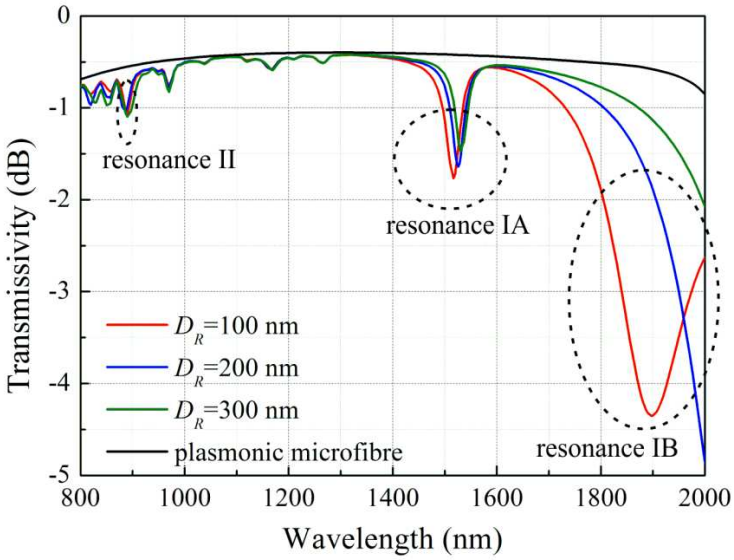

Figure 6-14 Transmissivity of the bow-tie PSNR for different edge-width D_R. d_R=34.3 nm and L_R=400 nm. The red, blue and green lines represent the PSNR width D_R=100 nm, 200 nm and 300 nm, respectively. The black line is the reference plasmonic microfibre.

6.2.2.3 Rectangular PSNRs with different edge width

We also considered the effect of edge width on the resonance characteristics of rectangular PSNRs. Figure 6-15 shows the calculated transmissivities with D_R = 34.3 nm, 100 nm, and 200 nm. The PSNR length L_R is 400 nm. The corresponding intensity enhancement factors for resonance II are 2.32×10^5, 1.94×10^4 and 2.72×10^3, respectively. The intensity enhancement factors for resonance IA and IB are 4.70×10^5, 9.88×10^4, 1.29×10^4 and 6.69×10^5, 9.04×10^4, 1.16×10^4, respectively. In contrast with bow-tie PSNRs, in this case increasing the edge width D_R shifts resonances IA and IB to shorter wavelengths.

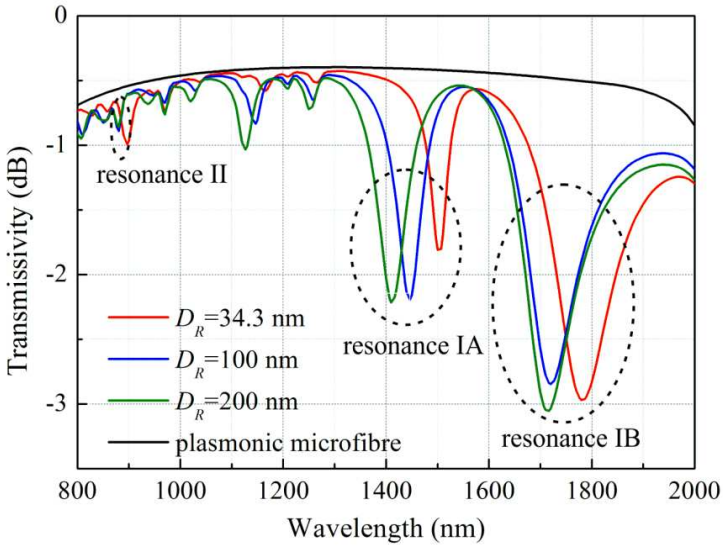

Figure 6-15 Transmissivity of the rectangular PSNR for different edge-width D_R and L_R=400 nm. The red, blue and green lines represent a PSNR with width D_R=34.3 nm, 100 nm and 200 nm, respectively. The black line is the reference plasmonic microfibre.

6.2.2.4 Resonance wavelength dependence on the PSNR perimeter

Simulation results so far have shown that the resonance wavelengths and intensity enhancement factor is affected by the PSNR geometrical dimensions. H. C. Guo et al [206] have reported that, under plane-wave excitation, bow-tie resonators show plasmonic resonance wavelengths that shift linearly with the resonator aperture perimeter.

Figure 6-16 (a) shows the resonance wavelength variation with the perimeter length for a bow-tie PSNR with different waist and fixed edge width (shown in Figure 6-13). When the waist width decreases, the perimeter of the bow-tie increases and both resonances IA and IB shift to longer wavelengths, albeit at different rates. Figure 6-16 (b) shows the resonance wavelength changes with the perimeter for the bow-tie PNSR with fixed waist and different edge width (shown in Figure 6-14). In this case, resonance IA shows almost no shift, while resonance IB shows a red shift with much larger slope. For the longest perimeter, resonance IB falls well within the plasmonic microfibre cut-off. Figure 6-16 (c) shows the resonance wavelength changes with the perimeter for the rectangular PNSR with varying edge width (shown in Figure 6-15). In this case, in contrast with the previous ones, both resonances IA and IB shift to shorter wavelengths as the perimeter is increased. These results suggest that the plasmonic resonances are related to the resonator perimeter

in a much more complex way than originally suggested in Ref. [206]. However, it is clearly demonstrated that the PSNR dimensions can be used to tune the various resonance wavelengths to desired spectral regions.

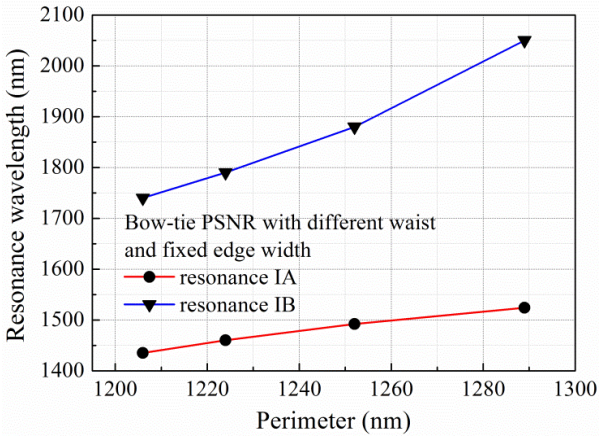

(a)

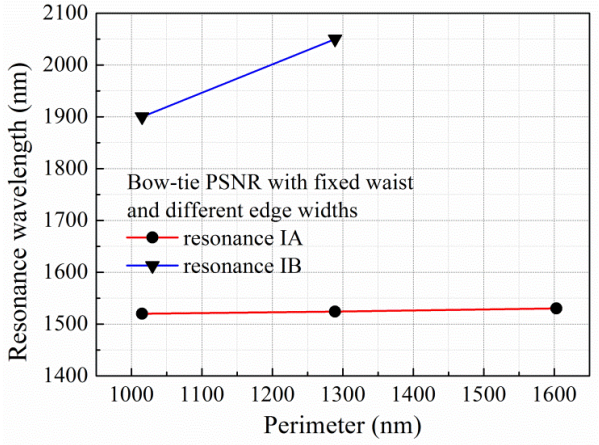

(b)

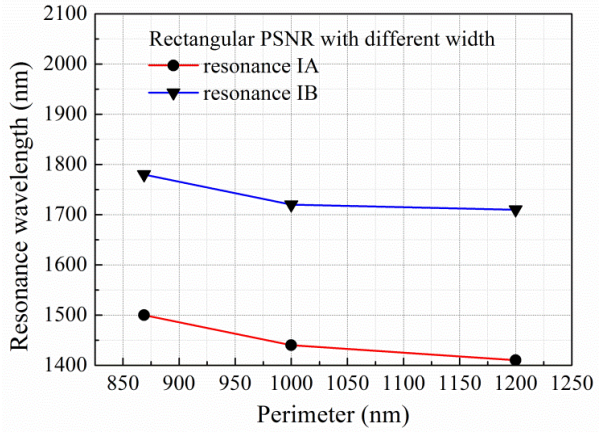

(c)

Figure 6-16 Resonance wavelength dependence on the perimeter length for (a) bow-tie PSNR with different waist and fixed edge widths; (b) bow-tie PSNR with fixed waist and different edge width; (c) rectangular PSNR with different edge width.

6.2.2.5 Intensity enhancement factor

The PSNR enhancement factor is possibly the most important feature for applications exploiting the strong field localization. The enhancement factors at the main resonance wavelengths discussed so far, for the different PSNRs, are summarized in Table 6-1.

Table 6-1 Intensity enhancement factor and associated resonance wavelength summary for the different type of PSNRs.

PSNR type	E_f (II)	E_f (IA)	E_f (IB)
Bow-tie D_R=200 nm, d_R=34.3 nm	4.7×10^4 λ=880 nm	2.5×10^5 λ=1524 nm	9.65×10^5 λ=2050 nm
Bow-tie D_R=200 nm, d_R=75.8 nm	3.33×10^4 λ=880 nm	2.16×10^5 λ=1500 nm	4.04×10^5 λ=1880 nm
Bow-tie D_R=200 nm, d_R=117.3 nm	1.26×10^4 λ=880 nm	7.54×10^4 λ=1460 nm	9.15×10^4 λ=1790 nm
Bow-tie D_R=200 nm, d_R=158.6 nm	5.20×10^3 λ=880 nm	3.11×10^4 λ=1440 nm	3.15×10^4 λ=1740 nm
Bow-tie D_R=100 nm, d_R=34.3 nm	4.29×10^4 λ=880 nm	3.31×10^5 λ=1520 nm	9.09×10^5 λ=1900 nm
Bow-tie D_R=300 nm, d_R=34.3 nm	4.73×10^4 λ=890 nm	1.84×10^5 λ=1530 nm	N/A
Rectangular D_R=34.3 nm	2.32×10^5 λ=900 nm	4.7×10^5 λ=1500 nm	6.69×10^5 λ=1780 nm
Rectangular D_R=100 nm	1.94×10^4 λ=880 nm	9.88×10^4 λ=1440 nm	9.04×10^4 λ=1710 nm
Rectangular D_R=200 nm	2.72×10^3 λ=880 nm	1.29×10^4 λ=1410 nm	1.16×10^4 λ=1720 nm

The table shows that the intensity enhancement factor is determined primarily by the PSNR waist and it is almost independent from the exact resonator shape and perimeter. It is also affected by the type of resonance. The smallest waist in this study was d_R=34.3 nm and for resonances IB gave

enhancement factors in excess of 9×10^5. This is an improvement comparing with the enhancement factor reported for the plasmoinc nano-resonator mostly in the order of 10^3 [205, 210-212]. It is worth stressing though that moving from rectangular to bow-tie shapes the resonance IB wavelength shifts from 1780 nm to 2050 nm. Therefore, bow-tie shapes are very effective in shifting resonance wavelengths and at the same time improving slightly the intensity enhancement factors.

6.2.3 *Multiple cascaded bow-tie PSNR*

Finally, the resonance characteristics of multiple, cascaded bow-tie PSNRs is considered. In this case, optical coupling between individual PSNRs is expected to result in more complex resonances and transmission spectra. Figure 6-17 shows the transmissivity (upper) and reflectivity (lower) in the case of two and three cascaded bow-tie PSNRs. The single PSNR as well as the plasmonic microfibre transmission spectra are included for comparison. The individual PSNR dimensions are the same as those of Figure 6-5.

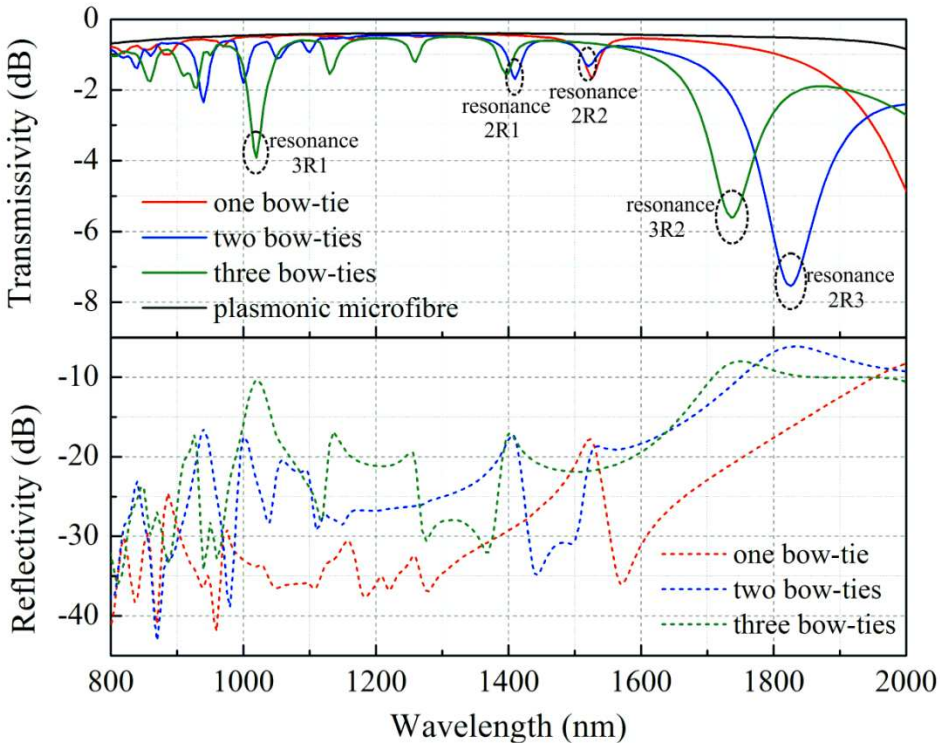

Figure 6-17 Transmissivity (upper) and reflectivity (lower) of the multiple cascaded bow-tie PSNRs. Red-solid (dashed), blue-solid (dashed) and green-solid (dashed) lines correspond to the transmissivity (reflectivity) of one, two and three PSNR cascades, respectively. The black-solid line corresponds to transmissivities for the plasmonic microfibre. Microfibre diameter D=1 μm,

gold film thickness t=30 nm, individual bow-tie PSNR length L_R=400 nm, width D_R=200 nm, and waist width d_R=34.3 nm.

In the case of the cascaded two PSNRs, in addition to the 1520 nm resonance, which corresponds to resonance IA of the single PSNR, two extra resonances appear on either side of it. Figure 6-18 shows the electric field modulus on the top surface x-z plane at the three aforementioned resonances (resonance 2R1 λ=1410 nm (top), resonance 2R2 λ=1520 nm (middle) and resonance 2R3 λ=1830 nm (bottom)), for the cascaded two bow-tie PSNRs. The field is localized in the centre of one PSNR at λ=1520 nm, while high localizations are shown in two PSNRs at λ=1410 nm and 1830 nm.

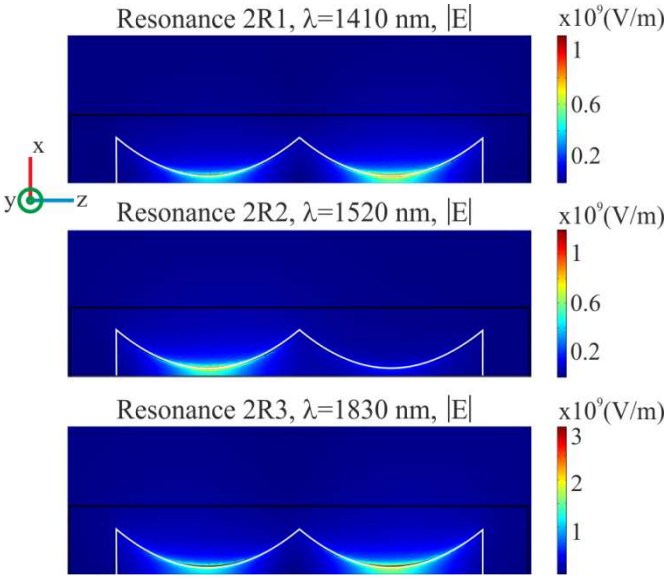

Figure 6-18 Electric field modulus on the top surface x-z plane at resonance 2R1 λ=1410 nm (top), resonance 2R2 λ=1520 nm (middle) and resonance 2R3 λ=1830 nm (bottom), for the two bow-tie PSNR cascade.

Figure 6-19 shows 3D plots of the x component of the electric field (E_x) distribution (left) and over the x-y plane cross section through the centre of each resonator (right), for resonances at λ=1410 nm (top), 1520 nm (middle) and λ=1830 nm (bottom). Resonances 2R1 and 2R3 are anti-symmetric combinations of the single bow-tie PSNR resonance IA. The field distributions over the two cross sections for resonances 2R1 and 2R3 correspond to predominantly second and first order transverse resonances. This behaviour is similar to the one discussed in Section 6.2.1.2 above in relation to a single rectangular PSNR. However, in this case, in the presence of two radiating dipole

antennas (see cross sections in Figure 6-19–right column), the propagating fields are perturbed in a more complex way. In the case of resonance 2R2, the corresponding field distributions show that only one bow-tie is resonant and affects the performance.

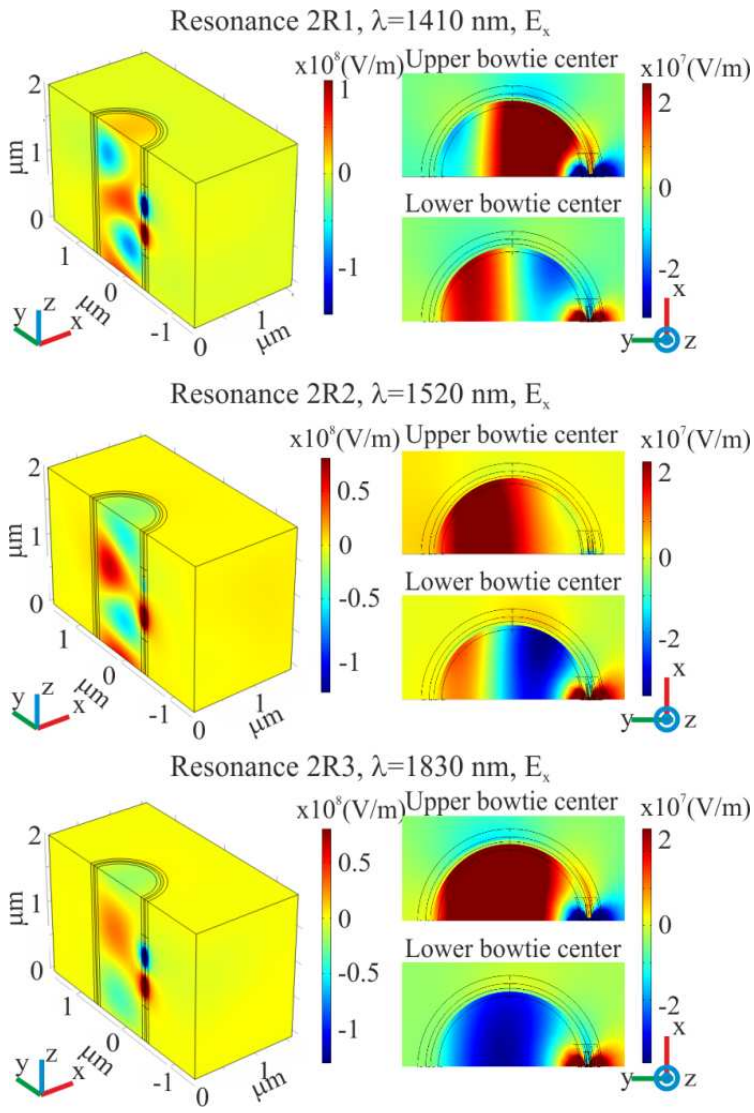

Figure 6-19 3D plots of the *x* component of the electric field (E_x) distribution (left) and over the *x*-*y* plane cross section through the centre of each resonator (right), for resonance 2R1 at λ=1410 nm (top), 2R2 at λ=1520 nm (middle) and 2R3 at λ=1830 nm (bottom).

In the case of three cascaded PSNRs a number of extra resonances appear in the spectrum, corresponding to the complex interference between the single bow-tie PSNR and the plasmonic waveguide. Figure 6-20 shows the electric field modulus over the top surface *x*-*z* plane at the two strongest resonances at λ=1020 nm (3R1 - top), and λ=1740 nm (3R2 - bottom), for the three cascaded

bow-tie PSNRs. Figure 6-21 shows 3D plots of the *x* component of the electric field (E_x) distribution for resonances 3R1 (left) and 3R2 (right).

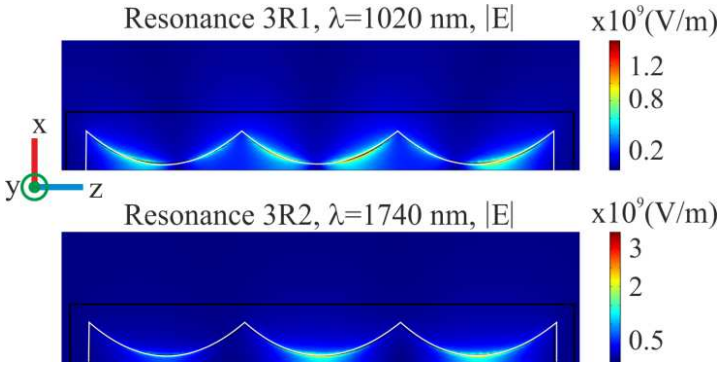

Figure 6-20 Electric field modulus on the top surface *x*-*z* plane at λ=1020 nm (top), and λ=1740 nm (bottom), for the three bow-tie PSNR cascade.

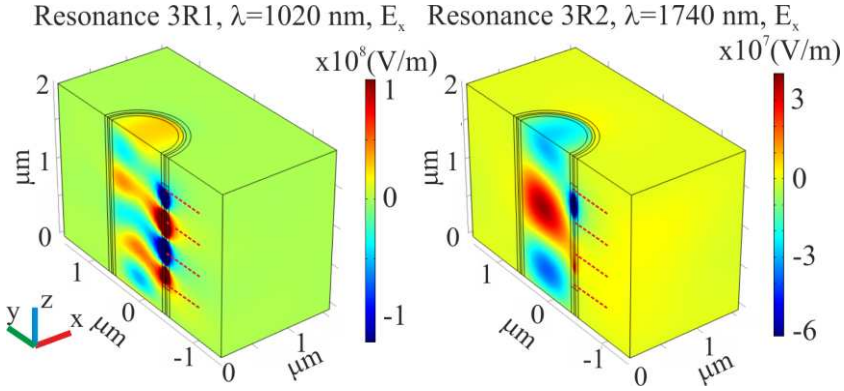

Figure 6-21 3D plots of the *x* component of the electric field (E_x) distribution for resonances 3R1 (left) and 3R2 (right).

Resonance 3R1 corresponds to a field distribution that matches closely the wavelength inside the plasmonic waveguide and "spills over" and crosses the boundaries of the individual PSNRs (marked with dotted lines). Resonance 3R2, on the other hand, shows a more complex field distribution as a result of a more involved interaction between the plasmonic cavities and the waveguide.

Table 6-2 summarizes the intensity enhancement factors associated with the strongest resonances discussed so far for the case of two- and three-PSNR cascades. It is shown that intensity enhancement factors in excess of 10^6 are achieved by cascading bow-tie PSNR. Again, the maximum enhancement is achieved with the longest-wavelength resonances. The enhancement is also observed in multiple spots, which can be advantageous in SERS and other sensor applications.

Table 6-2 Intensity enhancement factor at resonance wavelength for multiple cascaded bow-tie PSNR.

PSNR type	E_f (Different Resonances)		
Two bow-ties	1.35×10^5	1.81×10^5	1.24×10^6
	λ=1410 nm	λ=1520 nm	λ=1830 nm
Three bow-ties	2.83×10^5	1.51×10^6	
	λ=1020 nm	λ=1740 nm	

6.3 Numerical simulations of PSNR embedded in metal-coated optical fibre tips

In this section, the modelling of a rectangular PSNR embedded in optical fibre tips is discussed. Since the plasmonic waveguide is not cylindrical but conical, the behaviour of the device is different from that discussed in Section 6.2. Figure 6-22 (a) and (b) shows the structure used for modelling. Firstly, an optical fibre tip with 0.9667 μm minimum diameter, 1.47 μm maximum diameter and 5.33° taper angle was simulated to provide a reference. The waveguide was surrounded by air in a box sufficiently large and a *Perfectly Matched Layer* (PML) (see Appendix A) was added to avoid reflections from the boundaries (Figure 6-22 (a)). The chosen boundary conditions were: port boundary at the input and output, scattering boundary condition for the exterior boundary and continuity boundary condition for the interior boundary (the definition of boundary conditions are introduced in Appendix A). Light was launched from the input using boundary mode analysis. In order to save memory and reduce calculation time, half of the structure was calculated since the geometry is symmetric with respect to the *y*-*z* plane (Figure 6-22 (b)). The separatrix is set as a perfect electric boundary and the polarization of the launched light is along the *x* direction. Simulations were run with a controlled mesh size (80 nm in silica and 100 nm in surrounding air) to make efficient use of computer memory.

Reflectivity was calculated using the *S*-parameter in COMSOL, the same used in Section 3.2.3. Transmissivity was calculated by integrating the power

in the *x-y* plane placed 20 nm away from the output. The transmissivity and reflectivity of the fibre tip in the wavelength range from 1000 nm to 1600 nm is presented in Figure 6-22 (c) and used as a reference for the following analysis. Both spectra show very small variation and resonances at wavelengths λ=1100 nm and 1230 nm, corresponding to the interference between the input light and the reflected light from the tip.

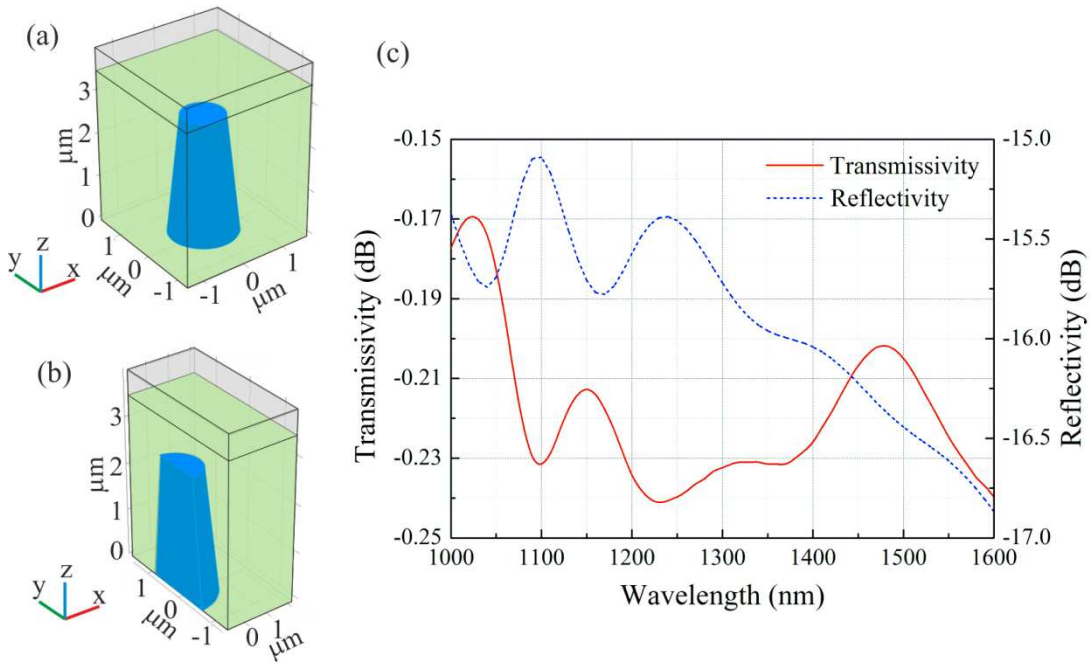

Figure 6-22 (a) Geometry of the modelled optical fibre tip (the blue, green and grey domains are silica, air and the PML which has the refractive index of air, respectively); (b) half of the fibre tip geometry; (c) transmissivity (red solid line) and reflectivity (blue dashed line) of the fibre tip. Fibre tip minimum diameter=0.9667 μm, maximum diameter=1.47 μm and taper angle =5.33°.

A 30 nm gold layer was then coated on the optical fibre tip (Figure 6-23 (a) and (b), the yellow domain is gold). The dispersion of both the real and the imaginary parts of the refractive index of gold was taken into account [115]. Since the thickness of gold is only 30 nm, composite SPPs can be excited over the thin gold film and the fibre tip. Figure 6-23 (c) shows the transmissivity and reflectivity of the gold-coated plasmonic fibre tip as a reference for the following analysis. Both spectra show resonances at wavelengths λ=1060 nm, 1140 nm, 1240 nm, 1340 nm and 1470 nm, corresponding to the interference between the input and the reflected lights from the gold layer.

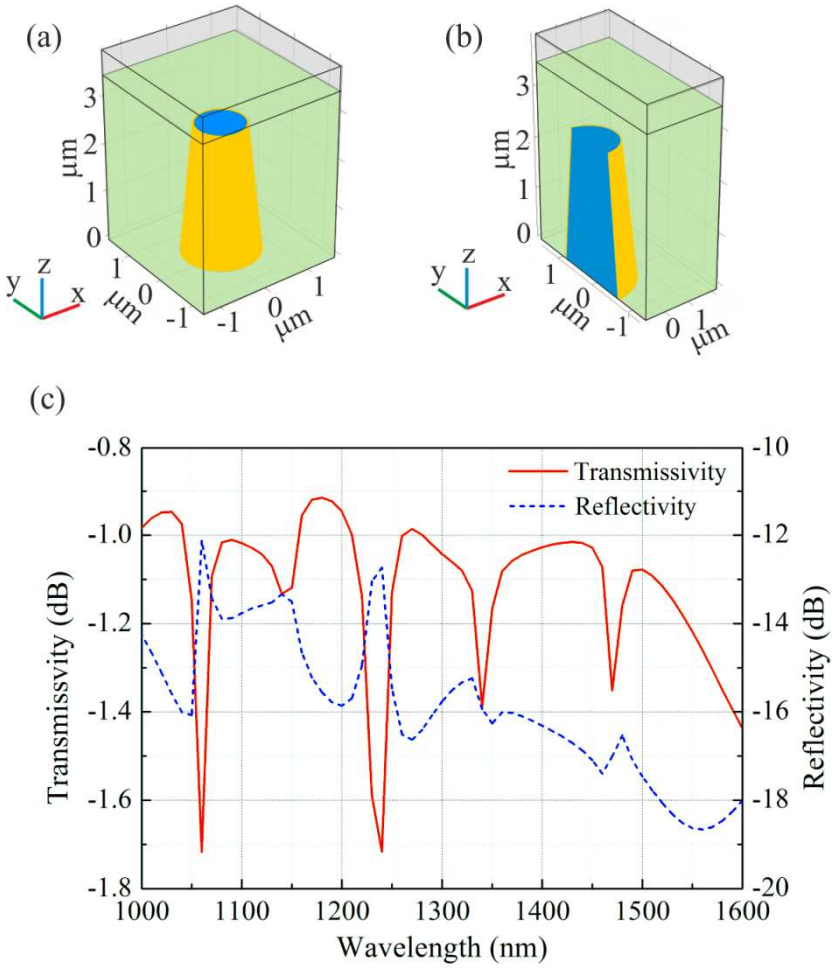

Figure 6-23 (a) Geometry of the modelled gold-coated plasmonic fibre tip (the blue, yellow, green and grey domains are silica, gold, air and the PML which has the refractive index of air, respectively); (b) half of the gold-coated plasmonic fibre tip geometry; (c) transmissivity (red solid line) and reflectivity (blue dashed line) of the gold-coated plasmonic fibre tip without PSNR. Fibre tip minimum diameter=0.9667 μm, maximum diameter=1.47 μm and taper angle =5.33°, gold film thickness t=30 nm.

Figure 6-24 (a-e) show the total electric field modulus ($|E|$) distribution of the plasmonic mode at the resonance wavelengths λ=1060 nm, 1140 nm, 1240 nm, 1340 nm and 1470 nm for launched x-polarized light. Since the fibre tip has a taper angle, the propagating light can be reflected by the gold layer; also, part of the light is reflected by the end face of the tip. Both reflected light components interfere with the input light leading to the interference pattern on the z direction. On the other hand, Figure 6-24 (f) shows the normalized electric field distribution of the plasmonic mode on the x-y plane at the end face of the tip at λ=1470 nm. The strongest plasmonic field localization is observed at point A (and its diametrically opposite). The field localization and intensity enhancement takes place inside the composite microtaper/thin metal

film structure and it is therefore inaccessible for sensing or other similar applications.

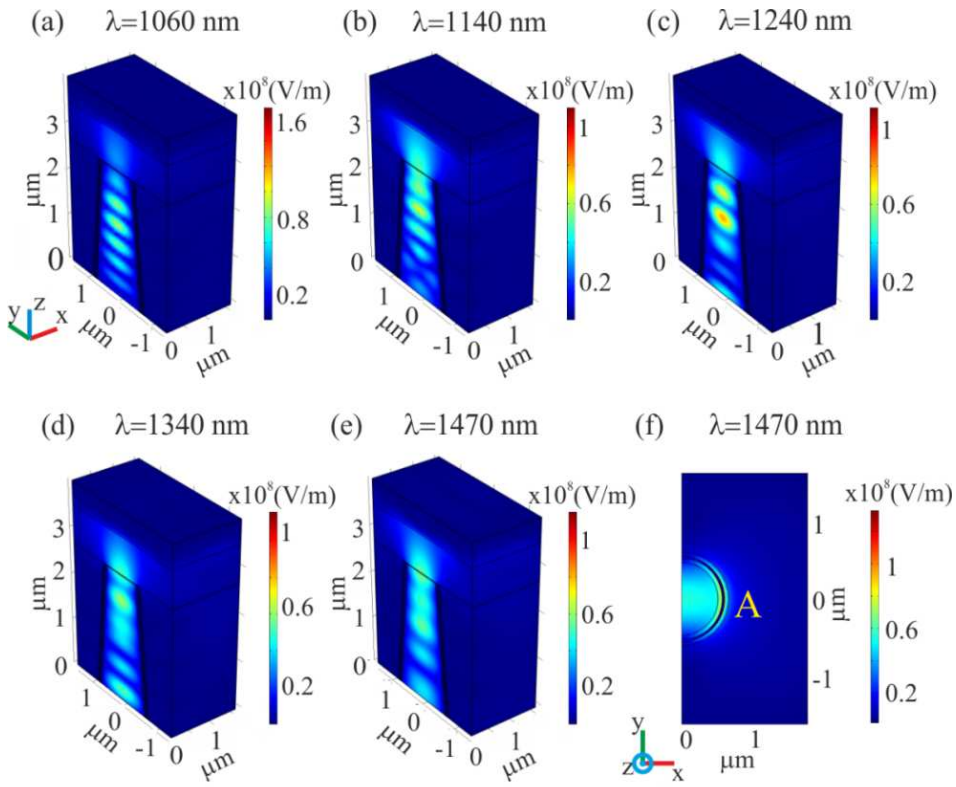

Figure 6-24 Normalized electric field when the launched light is polarized along the *x* direction at the wavelength λ= (a) 1060 nm, (b) 1140 nm, (c) 1240 nm, (d) 1340 nm and (e) 1470 nm; (f) normalized electric field distribution of the plasmonic mode on the *x*-*y* plane at the tip end face at λ=1470 nm.

In order to fully exploit and further enhance the resonant field enhancement in the tapered plasmonic structure, a plasmonic slot nano-cavity was then embedded on the side of the plasmonic fibre tip (Figure 6-25 (a)) at the position where the fibre tip diameter is 1.22 μm. It should be stressed that the introduction of the PSNR serves the dual purpose of further enhancing field localization and making it accessible. Figure 6-25 (b) gives the top-view of the PSNR with dimensions D_R width 400 nm and L_R length 200 nm. The depth of the slot nano-cavity is equal to the thickness (t) of the gold layer in the plasmonic fibre tip. In this calculation t=30 nm.

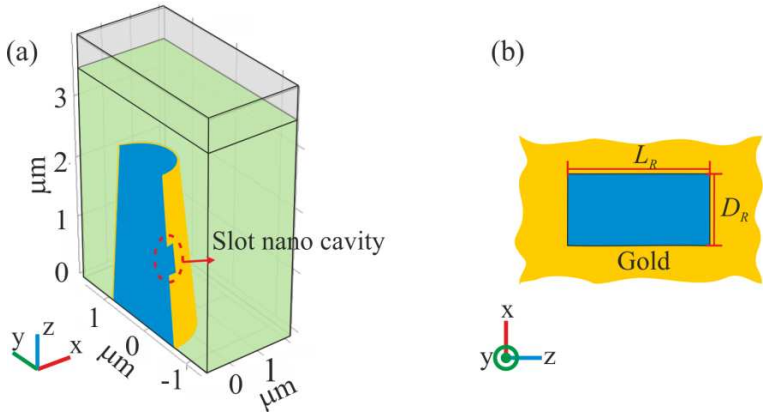

Figure 6-25 (a) Geometry of the PSNR embedded in the plasmonic fibre tip; (b) top-view of the rectangular plasmonic slot nano-cavity. L_R is the length and D_R is the width of the nano-cavity, respectively.

Figure 6-26 shows the transmissivity and the reflectivity of the composite structure with the rectangular PSNR when the input light is *x*-polarized. There are several dips observed in the transmission spectrum and associated peaks in the reflection spectrum, which correspond to different types of resonances of the embedded PSNR based on the plasmonic fibre tip. A comparison with Figure 6-23 (c) shows that several extra new peaks appear in the spectrum (e.g. λ=1270 nm, 1290 nm and 1450 nm), in which the new resonance at wavelength λ=1450 nm is the strongest.

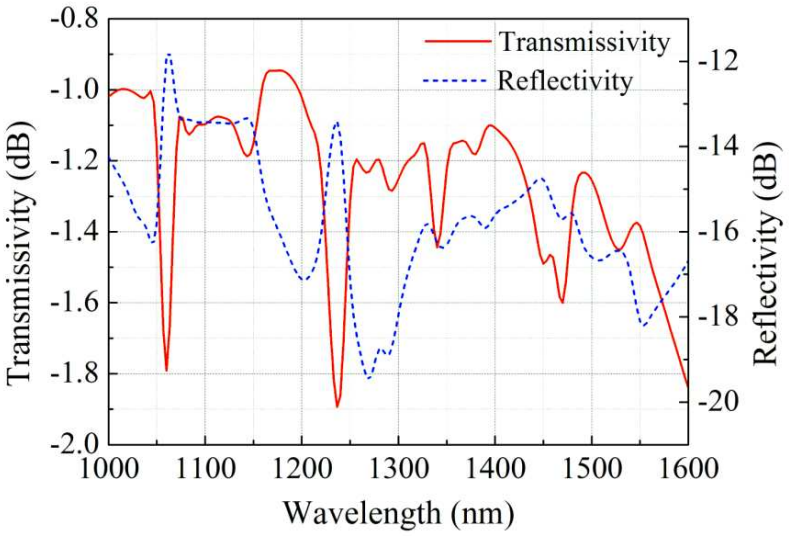

Figure 6-26 Transmissivity (red solid) and reflectivity (blue dashed) of the rectangular PSNR embedded in the plasmonic fibre tip for *x*-polarized light.

The total electric field modulus (|*E*|) on the *x*-*z* plane at the resonance wavelengths is presented in Figure 6-27. The intensity is plotted on a plane

tangential to the top resonator surface. At each major resonance (λ=1270 nm, 1290 nm, 1450 nm, and 1530 nm) the electric field is highly localized and it is close to centre on the rectangle. At minor resonances (λ=1080 nm, and 1380 nm), the electric field is observed gradually shifting off-centre and its strength decreases. Figure 6-27 (g) and (h) present the PSNR normalized electric field on the *x-y* and *y-z* planes at λ=1450 nm, which shows the 3D light localization in the PSNR.

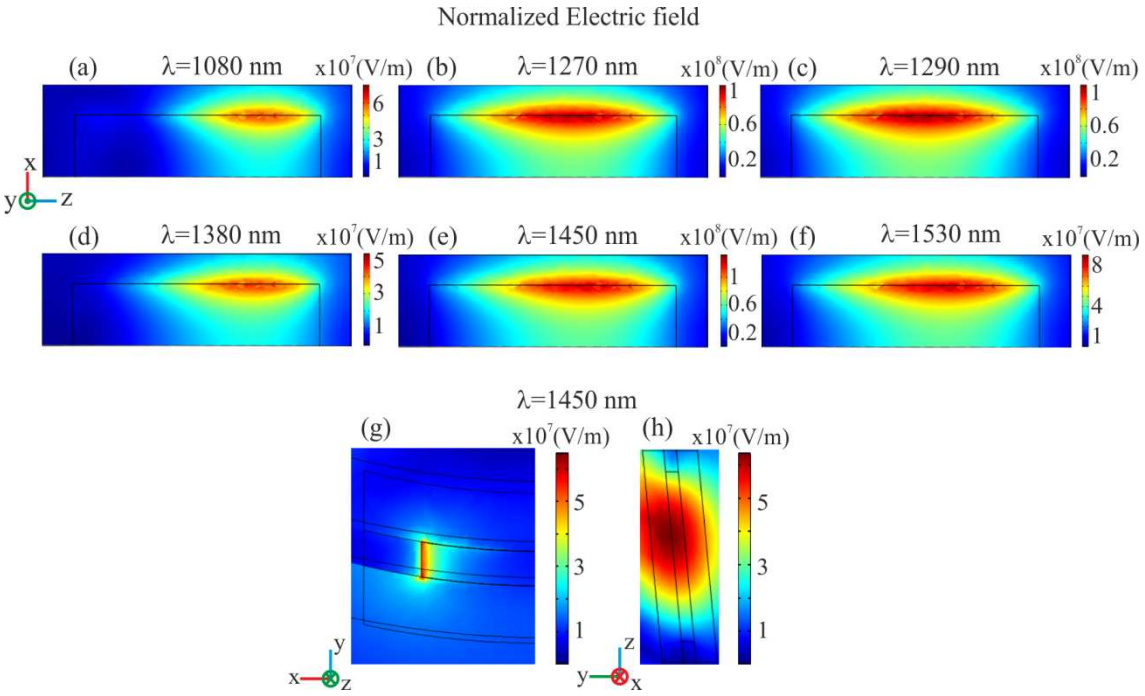

Figure 6-27 Normalized electric field on the *x-z* plane for rectangular PSNR at different resonance wavelength λ (a) 1080 nm, (b) 1270 nm, (c) 1290 nm, (d) 1380 nm, (e) 1450 nm, and (f) 1530 nm; (g) normalized electric field on the *x-y* plane at λ=1450 nm; (h) normalized electric field on the *y-z* plane at λ=1450 nm.

In order to investigate the effect of the nano-cavity on the transverse resonances of the plasmonic microfibre, the *x*-component of the electric field (E_x) distribution over the *x-y* plane cross section through the resonator centre at wavelengths λ=1240 nm, 1450 nm and 1470 nm without (upper row) and with (lower row) a nano-resonator is shown in Figure 6-28. At λ=1240 nm (Figure 6-28 (a) and (d)), which is one of the resonances in Figure 6-23, no significant distribution change is observed when the nano-cavity is embedded in the gold layer and the maximum intensity occurs in the interface of silica and gold 90 degrees away on either side of the nano-cavity position. The same

behaviour is observed at the other resonant wavelengths λ=1060 nm, 1140 nm, 1340 nm and 1470 nm. Thus, those resonances in Figure 6-26, which are common with the ones shown in Figure 6-23, are induced primarily by the back-reflection and modal beating from the gold layer and the tip. Insertion of the nano-cavity in this case does not alter significantly the intensity distribution. At the additional resonance at λ=1450 nm (Figure 6-28 (b) and (e)), on the other hand, the field is highly localized in the cavity and the maximum intensity occurs in the nano-resonator area. The characteristic dipole shapes in the nano-cavity are clearly observed, which are associated with a nano-antenna action. This nano-antenna radiation contributes to the transverse resonance and distorts the waveguide field distribution, as is shown in Figure 6-28 (b) and (e). Since the resonance at wavelength λ=1470 nm, which is one of the resonances in Figure 6-13, is very close to λ=1450 nm, it is also affected by the resonance at λ=1450 nm and shows high localization in nano-cavity and dipole shapes, although of smaller magnitude compared with λ=1450 nm. The resonance at λ=1450 nm is a purely nano-resonantor resonance and shows the largest field localization and intensity enhancement.

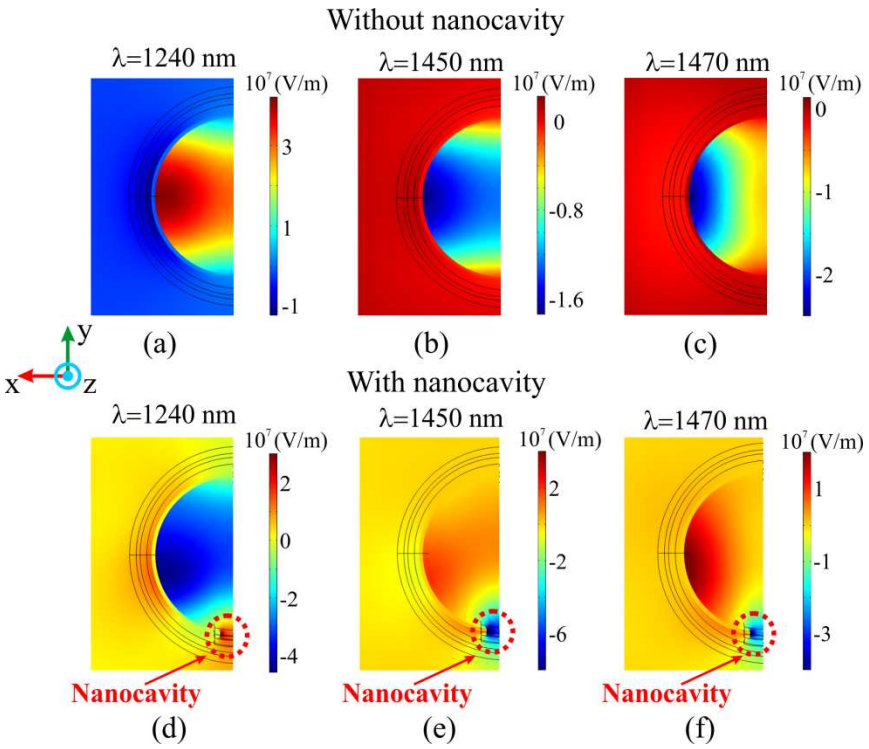

Figure 6-28 The *x* component of electric field distribution over the over the *x*-*y* plane cross section through the resonator centre at wavelength λ=1240 nm, 1450 nm and 1470 nm without ((a) (b) and (c)) and with ((d) (e) and (f)) nanocavity.

The enhancement factors at the main resonances of Figure 6-26 are summarized in Table 6-3. The intensity enhancement factor is determined by the resonance wavelength and is in excess of 10^3 at all resonances. The resonance wavelength 1450 nm with *x*-polarized light gave the biggest enhancement factor of 7.24×10^3, which is a few times larger than that at the other resonance wavelengths.

Table 6-3 Intensity enhancement factor at selected resonances for rectangular PSNR embedded in metal-coated optical fibre tips.

Resonance wavelength λ	E_f
1080 nm	1.55×10^3
1270 nm	2.72×10^3
1290 nm	2.95×10^3
1380 nm	1.10×10^3
1450 nm	7.24×10^3
1530 nm	2.30×10^3

6.4 Fabrication of PSNR embedded in metal-coated optical fibre tips

In order to verify the numerical analysis, experiments were carried out. Firstly, a rectangular plasmonic slot nanoresonator was fabricated on a gold-coated straight microfibre. However, no light was transmitted through the microfibre because of the gold absorption and bad gold deposition quality in the long taper region. Therefore, the plasmonic slot nanoresonator was inscribed on the surface of a gold-coated fibre tip. Since the fibre tip has a short taper region (~5 mm), the gold absorption can be small and light can be collected at the tip end. The fabrication process involved three main steps: manufacture of optical fibre tip, deposition of a thin gold layer and FIB nanopatterning.

The optical fibre tips were manufactured using the pipette puller already used for previous experiments. A 30 nm thickness layer of gold was then deposited on the tips using an E-beam evaporator to produce the plasmonic layer and to avoid charging during FIB processing.

The gold-coated plasmonic fibre tips were then nanostructured using a FIB milling system. The apex of the plasmonic fibre tips was flat cut at the diameter ~1 μm and a rectangular aperture with 400 nm length, 200 nm width and 30 nm depth as same as gold thickness was milled out on the tip side to form a PSNR at the position where the diameter is ~1.22 μm. The SEM image of the rectangular PSNR on a plasmonic fibre tip and its magnification image are shown in Figure 6-29 (a) (b). A clear rectangular PSNR is shown in the SEM images. However, the gold layer was slightly damaged by the re-deposition of silica removed during the aperture milling (Figure 6-29 (b)).

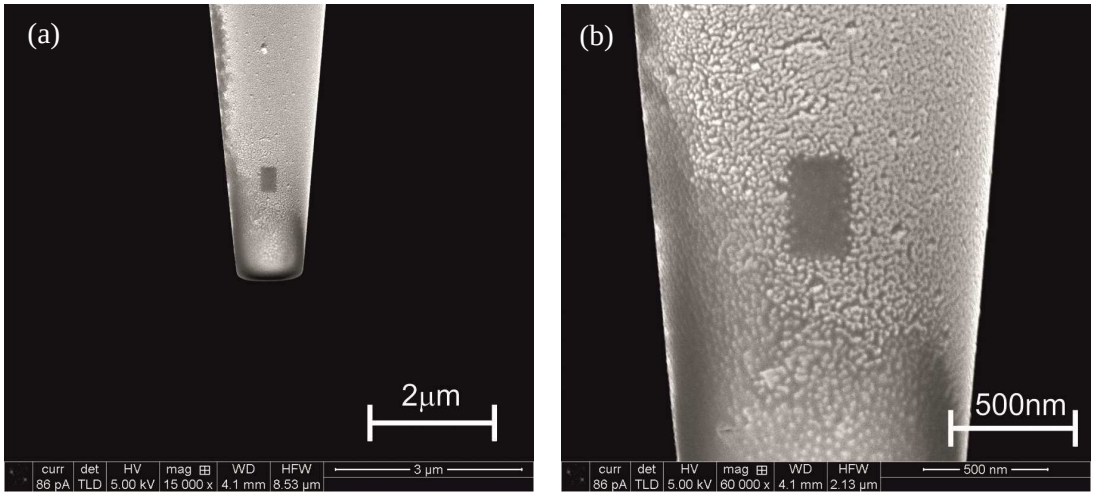

Figure 6-29 (a) SEM image of the plasmonic fibre tip with a rectangular PSNR; (b) magnified image of the cavity area.

6.5 Characterization of the PSNR embedded in the metal-coated optical fibre tips

The optical properties of the PSNR embedded in plasmonic fibre tips were characterized with the set-up shown in Figure 6-30 (a). A *Supercontinuum* (SC) source which is the same as used in Section 2.4 was used to inject light into the samples under test. A polarization rotator (OZ Optics, FPR-01 series) was

used to control the input beam state of polarization. Light from the polarization rotator was then launched into a bi-conical 2×2 microfibre coupler with an extremely wide, single mode operation bandwidth (400 nm-1700 nm) [152]. One of the output ports was connected to the sample and the other output port was immersed in the high refractive index liquid to avoid reflections from its end face. Only light reflected by the sample passed through the coupler and was recorded by an OSA (the same as used in Section 2.4). An XYZ stage was used to align the different fibre components.

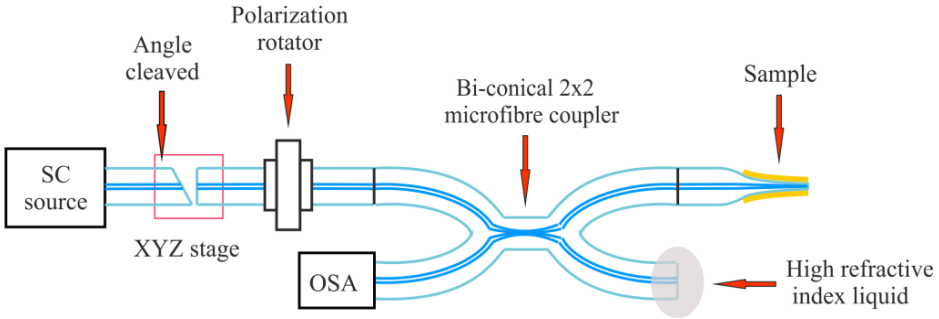

(a)

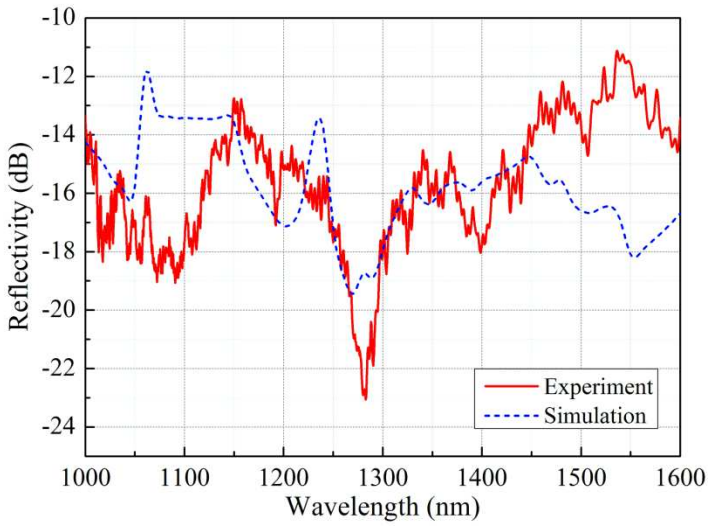

(b)

Figure 6-30 (a) Schematic of experimental set-up to characterize the PSNR spectral properties; (b) reflectivity spectrum of the sample in the experiment (the red solid curve) and in the simulation (the blue dashed curve).

Figure 6-30 (b) shows the reflectivity of the sample recorded at the polarization perpendicular to the PSNR. The red solid line shows the experimental results while the blue dashed line presents the theoretical prediction data modelled with the dimensions obtained from the SEM image in

Figure 6-29. The two graphs show a number of differences, like different resonance peak positions, slightly different reflection amplitudes and number of peaks. A possible explanation might be related to imperfect taper and gold layer surface and to particles attached to the gold layer surface. Particles induce plasmonic effects even when their size is small. Moreover, part of the gold layer was removed due to the re-deposition of material in the FIB processing and formed additional extremely small nano-cavities. This not only causes plasmonic cavities but also changes the interference condition in the plasmonic fibre tip. The increased device loss and its decreased amplitude ratio could be due to the imperfect gold layer thickness and surface smoothness. The polarization alignment error also can induce a significant difference in the experimental spectrum. Finally, the error on the sample geometry measurement contributed to the slight difference in the resonance wavelength between experiment and simulations.

6.6 Conclusions

In this chapter, PSNRs of different shapes embedded in thin-gold metal film coated plasmonic microfibres were firstly numerically investigated. The study included single bow-tie and rectangular PSNRs, as well as cascaded two and three bow-tie PSNRs.

The SPP mode supported by the cylindrical waveguide was anti-symmetric bound. The most important transmission and reflection resonances were associated with first and second order resonances along the PSNR length, for *x*-polarized light (perpendicular to the waist side-walls). It was also demonstrated that in order to fully understand the observed resonances in this strongly-coupled 3D resonator structure, in addition to the free-standing PSNR, the surrounding plasmonic waveguide has to be considered. This interaction is stronger and more complex in the case of multiple cascaded PSNRs.

The intensity enhancement factor and the resonance wavelength shift were calculated as a function of the PSNR dimensions. A single resonator shows enhancement factors in excess of 9×10^5, which are believed to be the biggest enhancement factors calculated in all types of nano-resonators so far. It is found that the resonance wavelength shifts in this strongly-coupled plasmonic

waveguide/nano-resonator structures are not defined entirely by one parameter, e.g. the nano-resonator perimeter, as it was found in the literature for free standing PSNRs. Instead, wavelength shift rates were found to be strongly dependent on the nature of the associated resonance and the plasmonic waveguide characteristics. It was observed that resonances lying closer to the plasmonic waveguide fundamental mode cut-off are much more sensitive to the PSNR dimensions. This is expected since approaching cut-off in plasmonic cylindrical waveguides, the hybrid anti-symmetric mode group velocity decreases and the interactions with adjacent resonators increase.

In addition to higher wavelength shift sensitivities, the longer wavelength resonances showed also the largest intensity enhancement factors.

The use of multiple cascaded PSNR structures results in even higher intensity enhancement factors (in excess of one million) in multiple spots. The combination of these features implies that designs that are based on longer wavelength resonances are the most promising candidates for advanced applications such as SERS, optical filtering, spectroscopy and bio-sensing.

This chapter also reported theoretically and experimentally the transversal excitation of a rectangular PSNR embedded in a thin gold film coated plasmonic fibre tip for the first time. When a PSNR was introduced in a gold-coated fibre tip supporting SPPs, the electric field was highly localized in the cavity centre. The strongest enhancement factor, 7.24×10^3, was achieved for the resonance at the wavelength λ~1450 nm recorded when light was polarized perpendicularly to the PSNR. FIB milling was used in the experiments to inscribe a PSNR on the gold-coated plasmonic fibre tip. The performance of the device can be improved by using fibre tips with smaller taper angle, improving the gold layer quality and working in a dust-free, clean room environment. This device can be used for SERS, spectroscopy and bio-sensing.

Chapter 7 Summary and future works

No matter where you are in life, there is always more journey ahead.

Nelson Mandela

7.1 Summary

In the past decade, optical fibre tapers have attracted much attention because of the unique properties that materials display on the nanoscale. In this thesis, nanostructuring has been used to extend even further the fibre taper confinement properties and investigate some related applications.

High transmission efficiency and high power are fundamental requirements for many applications, which include amongst others data recording, imaging and photolithography. An efficient sub-wavelength light confinement source capable of focusing focus relatively high powers has been proposed in Chapter 2. In order to optimize the fibre tips' design and obtain high transmission efficiencies, theoretical analysis was carried out using 3D finite element method to numerically solve Maxwell's equations in the frequency domain, so as to provide a reference for the device fabrication. Devices were manufactured using a P-2000 micropipette-puller, an evaporator, and a *Focused Ion Beam* (FIB) system to obtain the 2D light confinement. Device transmission spectra were measured with a supercontinuum source and transmission efficiencies of the order of a few percent were recorded. The optical fibre tips could survive powers as large as 1 W and thermal expansion measurements showed no

shape changes could be detected within the accuracy of the system (~2 nm) for 9 mW injected powers. Future optimizations will require the use of conical tips and near-field measurement to characterize the spot size. Effective confinements to 10 nm or smaller can be envisaged by decreasing the aperture size and slope angle.

3D light confinement was achieved in Chapter 3 by inscribing periodic air notches with a centred microcavity in an optical microfibre. As an intermediate step, the *Microfibre Bragg Grating* (MFBG) was demonstrated by inscribing air notches in the microfibre using FIB milling. Normally, in optical fibres, the small refractive index modulation in the grating implies that thousands of periods are needed to provide strong reflectivity; on the contrary, the large refractive index contrast between silica and air used in MFBGs requires only dozens of periods to achieve a strong grating. In addition, if a fibre with a high refractive index core was used to make the taper, the number of grating periods could be decreased even further: by using the large refractive index contrast at the interface between the microfibre material and air, gratings can be manufactured even with only a few periods. Both simulations and experiments showed a Bragg reflection peak in the spectrum considerably broader (~75 nm) than that observed in uniform *Fibre Bragg Grating* (FBGs) (~1 nm) written in conventional fibres. Strong reflection (-3 dB corresponds to 50% reflection) was observed with only 20 periods MFBG. This compact MFBG can find a wealth of applications and be widely used in sensing. In the sensor application field, the size of grating is a key issue. While the size of the conventional FBG is limited by Δn and fibre diameter, in a microfibre with only a few micrometres diameter, the grating size can be decreased drastically and the presence of a strong evanescent field can increase the sensor sensitivity to environmental properties. Based on MFBG, a Bragg grating with phase shift in the centre was demonstrated to obtain 3D light confinement. Since in optical microfibres light is radially confined by the cladding/air interface, for appropriate microfibre diameters the diffraction limit can be achieved. Longitudinally, confinement is provided by the phase shift in the centre of the *Microfibre Phase-Shifted Bragg Grating* (MPSBG): the distance along which confinement occurs is related to the refractive index contrast of the grating. Experimentally, MPSBGs were manufactured carving notches in microfibres,

thus achieving an index contrast of ~0.45 at the wavelength λ~1 μm. Experiments showed a resonance dip at λ~1180 nm, which corresponds to the cavity resonant wavelength, resulting in a cavity quality factor Q~60. 3D COMSOL simulations were used to verify the experimental results. This MPSBG can be used for a wide range of applications, from sensing to triggered single-photon sources.

Light confinement in microfibres was also used in Chapter 4 to demonstrate a fast-response high temperature sensor. Using a broadband *Microfibre Coupler Tip* (MFCT), temperatures up to 1511ºC were measured. Two methods were used to monitor the temperature: the first relies on the wavelength shift associated with the coupler sinusoidal output for increasing temperatures (this shift can be evaluated by recording the reflection spectrum using an optical spectrum analyser). The second method relies on the evaluation of the power change over a bandwidth of 1 nm at a fixed wavelength. A MFCT with 2.5 μm showed an average sensor responsivity R~11.96 pm/ºC in the temperature range ~247ºC to ~1283ºC, comparable to the value obtained for FBG thermometers at lower temperature, T. The sensor repeatability was determined to be good by measuring the temperature for increasing and decreasing values with an interval of one hour. 2D spatial resolution was also demonstrated by monitoring the temperature at a distance of ~250 μm from the Ni-Cr surface along the tangential direction. Because of the small coupler cross section, the theoretical device resolution is limited by the Raleigh criterion, meaning that measurements with resolutions smaller than 5 μm can be possible.

Response times as little as 16.6 ms were obtained with a 12.6 μm diameter MCFT. From the dynamic thermal behaviour theory, the response time is proportional to the MFCT radius. Since the MFCT radius can be very small, the response of MFCT to temperature could be very fast. While a MFCT with 12.6 μm diameter had a sensor resolution S~0.66ºC in the temperature interval ~85ºC to ~1511ºC, a better resolution S~0.10ºC but smaller dynamic range (from T~85ºC to T~1283ºC) was observed with the 4.8 μm diameter MFCT. The MFCT offers several advantages, including compactness, extremely high temperature measurement capabilities, fast response, easy connection with other fiberized optical components, simple fabrication and low cost. By setting a reference wavelength and measuring the intensity ratio between the two

wavelengths, the sensitivity can be further improved and the error associated with the source power drift/oscillations can be minimized.

Amongst the applications of optical fibre tapers, one of the most important is coupling with the resonator and exciting *Whispering Gallery Modes* (WGMs) with high-*Q* resonance. In this thesis, a method to excite selected WGMs in optical *Bottleneck Microresonators* (BMRs) by inscribing microgroove scars on their surface by FIB milling was demonstrated. In BMRs, the dense spectral characteristics are to be used as sensors, where a spectrum with features more easily identifiable and traceable over large wavelength ranges is desirable. The introduction of the localized damage ("scar") on the BMR surface preferentially attenuates a subset of modes and results in substantial reduction of the number of spectral resonances. Modes overlapping with the milled grooves experience high losses and disappear, while modes in the bottle central part can survive and resonate efficiently. Both experiments and theory have proved that a single high-*Q* mode was predominantly selected using two asymmetrical perpendicular scars. By placing the grooves closer to the BMR centre, only the modes with resonance in the bottle centre can be excited and truly single mode operation can be achieved. The performance of microstructured BMRs can be further improved by optimizing the scar shape, size and orientation. This technique can also be employed to clean-up spectra in other types of non-spherical micro-resonators.

Finally Chapter 6 studied the *Plasmonic Slot Nano-Resonators* (PSNRs) on optical fibre tapers. Different shapes of PSNRs, embedded in thin-gold metal film coated plasmonic microfibres, were numerically investigated. The study included single bow-tie and rectangular PSNRs, as well as cascades of two and three bow-tie PSNRs. The most important transmission and reflection resonances were associated with first and second order resonances along the PSNR length, for *x*-polarized light (perpendicular to the waist side-walls). It was also demonstrated that in order to fully understand the observed resonances in this strongly-coupled 3D resonator structure, in addition to the free-standing PSNR, the surrounding plasmonic waveguide has to be considered. This interaction is stronger and more complex in the case of multiple cascaded PSNRs. The intensity enhancement factor and resonance wavelength shifts were calculated as a function of the PSNR dimensions. A single resonator

shows enhancement factors in excess of 9×10^5. The resonance wavelength shifts in this strongly-coupled plasmonic waveguide/nano-resonator structures are not defined entirely by one parameter, e.g. the nano-resonator perimeter, as was found in the literature for free standing PSNRs. Instead, wavelength shift rates were found to be strongly dependent on the nature of the associated resonance and the plasmonic waveguide characteristics. It was observed that resonances lying closer to the plasmonic waveguide fundamental mode cut-off are much more sensitive to the PSNR dimensions. In addition to higher wavelength shift sensitivities, the longer wavelength resonances showed also the largest intensity enhancement factors. The use of multiple cascaded PSNR structures results in even higher intensity enhancement factors (in excess of one million) in multiple spots. The combination of these features implies that designs that are based on longer wavelength resonances are the most promising candidates for advanced applications such as *Surface-Enhanced Raman Scattering* (SERS), optical filtering, spectroscopy and bio-sensing.

The transversal excitation of a rectangular PSNR embedded in a thin gold film coated plasmonic microfibre tip was reported both theoretically and experimentally for the first time. When a PSNR was introduced in a gold-coated microfibre tip supporting SPPs, the electric field was highly localized in the cavity centre. The strongest enhancement factor, 7.24×10^3, was achieved for the resonance at the wavelength λ~1450 nm, recorded when light was polarized perpendicularly to the PSNR. The reflectivity in the experiment fits that in the simulations. The performance of the device can be improved by using microfibre tips with smaller taper angle, improving the gold layer quality and working in a dust-free, clean room environment.

7.2 Future work

Since both optical fibre tapers and nanostructuring are very hot and attractive topics, future work about nanostructured optical fibre tapers seem very promising. The following are just a few examples.

7.2.1 *Efficient light confinement with nanostructured optical fibre tips for next generation hard disk drivers*

Hard Disk Driver (HDD) became the most important storage device since it was introduced by IBM in 1956 and HDD has been widely used in the modern era of servers and PCs. While the tremendous increase in magnetic *Areal Density* (AD) and the associated decrease of cost per gigabyte has been largely responsible for the proliferation of HDD recording into new applications and markets, it was necessary to overcome the superparamagnetic effect which limited AD in perpendicular magnetic recording. By avoiding superparamagnetism, *Heat-Assisted Magnetic Recording* (HAMR) was introduced to extend the AD of magnetic data storage [116].

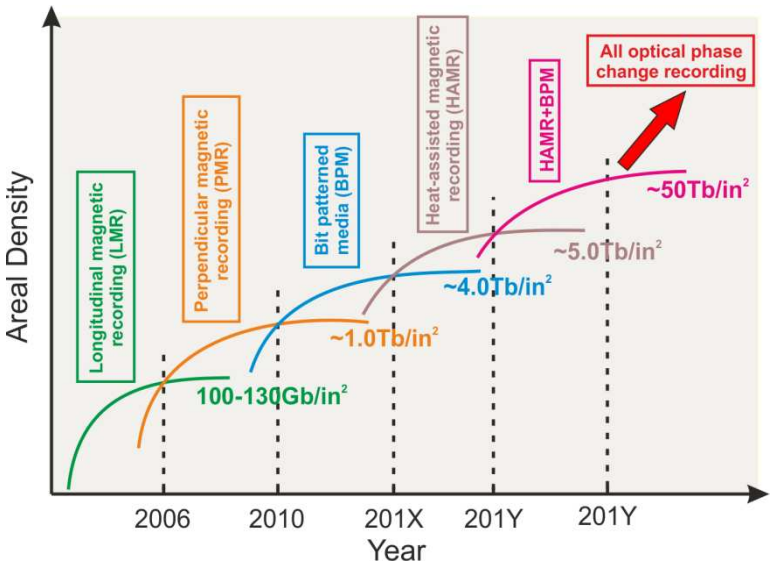

Figure 7-1 Growth of areal density for magnetic recording.

However, for storage densities greater than 1 Tb/in^2, HAMR requires optical spot sizes less than 30 nm. This is perhaps one of the most challenging aspects of HAMR head design. Unfortunately, the optical spot sizes that are obtainable by focusing light from the currently available technologies are much larger than the 30 nm spot size necessary for > Tb/in^2 storage densities in HAMR. Near-field optics was employed in a HAMR storage system to achieve optical spot sizes much smaller than the diffraction limit. However, the primary difficulty in HAMR is to deliver a significant fraction of the incident light power within this small spot to the sample.

In the meanwhile, *Phase Change Recording* (PCR) has advanced remarkably and also become a mature technology for rewritable data storage systems since it was initiated in the 1960s by Ovshinsky [213]. Many researchers argue that these materials will provide a universal memory technology that could replace both magnetic hard drive and dynamic random-access memory, and even mimic the human brain [214, 215]. If PCR can be used as the material in HDD, the AD could have a significant improvement when a light source with an extremely small spot size is applied.

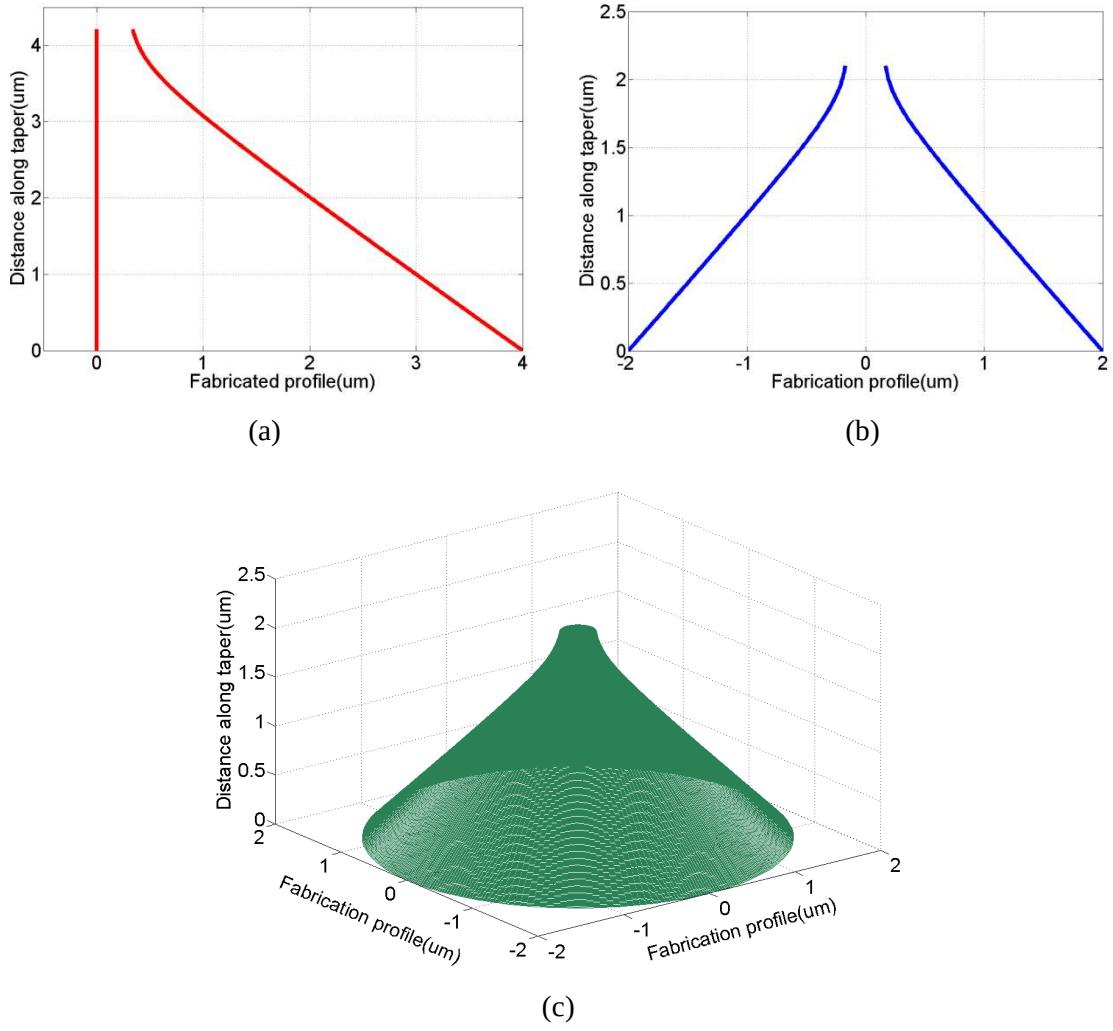

Figure 7-2 Enhanced fabrication profile. (a) Single cut version; (b) double cut version; (c) conical cut version.

From the sub-wavelength light confinement source proposed in Chapter 2, simulations with circularly polarized light input show that effective confinements to 10 nm or smaller with transmission efficiency 10^{-2} can be envisaged by optimizing the optical fibre tip design. Therefore, a sub-wavelength confinement light source could revolutionize the next generation

of HDDs. However, in order to use the device in the industrial application, there is still plenty of room for improvement.

(1) A better confinement needs to be investigated with a pyramidal or conical shape tip and such a precise structure can be obtained by FIB. Surface plasmon excitation should be optimized. If the light propagation constant changes instantly with fibre tip diameter, the resonance angle should be completely defined by the tip local diameter (Figure 7-2).
(2) Near-field characterization of the source needs to be performed, possibly using SNOM to characterize the real spot size of the device.
(3) The device needs to be included in the hard disk writer head and the whole system performance tested.

7.2.2 Optimization of 3D light confinement with microfibre phase-shifted Bragg grating and its application to lasers

Stronger confinement can be achieved by optimizing the dimensions of the structure for the MPSBG presented in Chapter 3. Further optimization of manufacturing parameters (such as the grating pitch number and period, notch width and length and the microfibre diameter) can provide a more compact device with improved performance. In analogy to the case of phase-shifted fibre Bragg gratings, the cavity response is related to the grating length and *Q*-factors in excess of 10^3 can be easily predicted for a larger number of notches.

Although the embedded polymer increased device sturdiness, the interface of air and polymer induces losses to the MPSBG. Electrostatic charges can be used to temporarily support the microfibre. By filling the cavity with emitting materials, e.g. polyfluorene, the MPSBG can emit light at specific wavelengths and obtain a laser with truly micrometres size. Figure 7-3 shows a MPSBG which has 20 periods on the two sides of the centre cavity: lasing emission at λ=560 nm is expected when polyfluorene is filled in the central cavity. Polyfluorene deposition could be done with the aid of high accuracy atom force microscopy.

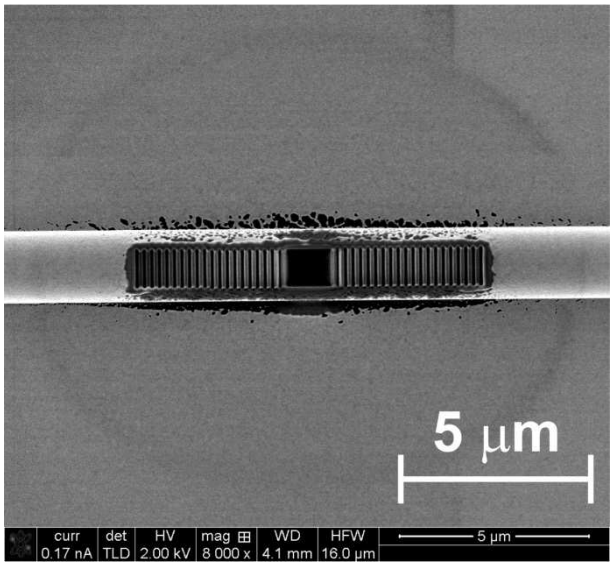

Figure 7-3 A MPSBG designed to work at λ=560 nm when polyfluorene is filled in the central cavity. The notch dimensions, taper diameter and grating periods are 100 nm×1000 nm, ~1.87 μm and 200 nm, respectively; the microcavity length is ~1.23 μm

7.2.3 *Packaged fast-response microfibre coupler tip temperature sensor*

Chapter 4 showed a compact temperature sensor which uses a MFCT for fast response, high temperature sensing with high 2D spatial resolution. Although this MFCT has advantages like compactness, extremely high temperature measurement capabilities and fast response, the tips are exposed to the air and any particle on the tips will affect the performance of the MFCT. To protect the MFCT and make it commercial, packaging it in a metal tube which can afford high temperature, like tantalum (melting point: 3017ºC) or platinum (melting point: 1768ºC), could be a solution. The MFCT properties after packaging in a metal tube needs to be characterized. Fixing the MFCT and stabilizing it in the tube are big challenges.

7.2.4 *Sensing with bottleneck microresonators*

Since the spectrum is very dense in a BMR, it is a serious hindrance if BMRs are to be used as sensors. By inscribing grooves in BMRs in the proper position, which has been introduced in Chapter 5, single mode operation can be achieved. The property of the BMRs can be chosen with different size and shape grooves. Figure 7-4 shows two designs of microgrooves in BMRs which can operate at a single mode. Only the mode whose intensity minima are on

the grooves can survive in Figure 7-4 (a) and the higher order mode can be cleaned up significantly with the design in Figure 7-4 (b). With these designs, BMRs can be used as sensors to measure a variety of parameters, including, amongst others, refractive index, force, and angle.

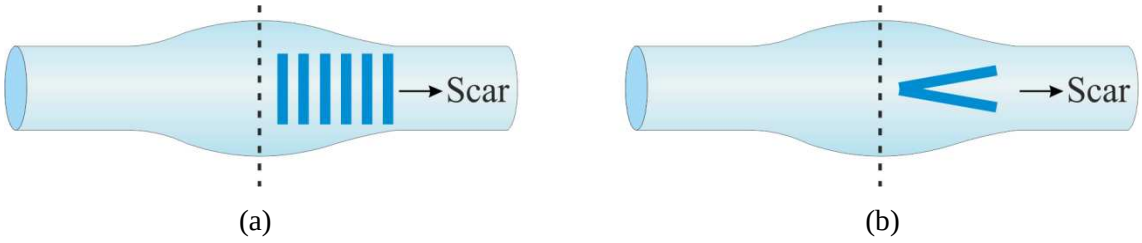

Figure 7-4 Schematic of two designs for single mode operation BMRs. (a) Multi-grooves on BMR; (b) V-groove on BMR.

This BMR could also be used as a polarizer if a layer of gold is coated on half of the bottle. The polarization dependence of the half coated BMR will need to be investigated.

7.2.5 Experimental realization of plasmonic slot nano-resonators in optical microfibre

In Chapter 6, differently shaped PSNRs, embedded in a thin-gold film coated plasmonic microfibre have been investigated numerically. Experimental implementation of the simulation can find a wide range of applications such as SERS, optical filtering, spectroscopy and bio-sensing.

In PSNRs embedded in gold-coated plasmonic fibre tips, resonances were observed in the gold-coated plasmonic fibre tip even when the nano-cavity was not embedded in the optical fibre tip because of the reflection interference. By introducing the nano-cavity, the original resonances were enhanced further and a few extra resonances were observed in the spectrum. Therefore, different nano-cavity positions will not only affect the original resonances differently, but also show extra resonances at different wavelengths. If the nano-cavity were to be embedded in the position which has the strongest field in the plasmonic fibre tip, a stronger enhancement could be obtained. By optimising the nano-cavity position the resonance wavelength could be tuned and the enhancement factor optimised for specific applications like sensing or filtering.

Appendix A Boundary conditions in COMSOL Multiphysics

Scattering Boundary Condition: Used when a boundary is wanted to be transparent for a scattered wave. This boundary condition is also transparent for an incoming plane wave. The boundary is only perfectly transparent for scattered (outgoing) waves of the selected type at normal incidence to the boundary.

Continuity Boundary: it is the natural boundary condition ensuring continuity of the tangential components of the electric and magnetic fields.

Perfect Electric Conductor: it is a special case of the electric field boundary condition that sets the tangential component of the electric field to zero.

Port Boundary: it is used to specify wave type ports according to the modelling.

Perfectly Matched Layers (PMLs): A PML is not, strictly speaking, a boundary condition but an additional domain that absorbs the incident radiation without producing reflections.

Bibliography

[1] A. W. Snyder and J. D. Love, *Optical Waveguide Theory*: Springer, 1984.

[2] G. Brambilla, V. Finazzi, and D. J. Richardson, "Ultra-low-loss optical fiber nanotapers," *Optics Express,* vol. 12, pp. 2258-2263, May 17 2004.

[3] V. I. Balykin, K. Hakuta, F. Le Kien, J. Q. Liang, and M. Morinaga, "Atom trapping and guiding with a subwavelength-diameter optical fiber," *Physical Review A,* vol. 70, p. 011401(R), Jul 2004.

[4] F. Le Kien, V. I. Balykin, and K. Hakuta, "Atom trap and waveguide using a two-color evanescent light field around a subwavelength-diameter optical fiber," *Physical Review A,* vol. 70, p. 063403, Dec 2004.

[5] E. Vetsch, S. T. Dawkins, R. Mitsch, D. Reitz, P. Schneeweiss, and A. Rauschenbeutel, "Nanofiber-Based Optical Trapping of Cold Neutral Atoms," *IEEE Journal of Selected Topics in Quantum Electronics,* vol. 18, pp. 1763-1770, Nov-Dec 2012.

[6] A. Goban, K. S. Choi, D. J. Alton, D. Ding, C. Lacroute, M. Pototschnig, T. Thiele, N. P. Stern, and H. J. Kimble, "Demonstration of a State-Insensitive, Compensated Nanofiber Trap," *Physical Review Letters,* vol. 109, p. 033603, Jul 19 2012.

[7] G. Brambilla, G. S. Murugan, J. S. Wilkinson, and D. J. Richardson, "Optical manipulation of microspheres along a subwavelength optical wire," *Optics Letters,* vol. 32, pp. 3041-3043, Oct 15 2007.

[8] G. S. Murugan, G. Brambilla, J. S. Wilkinson, and D. J. Richardson, "Optical propulsion of individual and clustered microspheres along sub-micron optical wires," *Japanese Journal of Applied Physics,* vol. 47, pp. 6716-6718, Aug 2008.

[9] G. Brambilla and F. Xu, "Adiabatic submicrometric tapers for optical tweezers," *Electronics Letters,* vol. 43, pp. 204-206, Feb 15 2007.

[10] J. Villatoro and D. Monzon-Hernandez, "Fast detection of hydrogen with nano fiber tapers coated with ultra thin palladium layers," *Optics Express,* vol. 13, pp. 5087-5092, Jun 27 2005.

[11] J. Y. Lou, L. M. Tong, and Z. Z. Ye, "Modeling of silica nanowires for optical sensing," *Optics Express,* vol. 13, pp. 2135-2140, Mar 21 2005.

[12] F. Xu, P. Horak, and G. Brambilla, "Optical microfiber coil resonator refractometric sensor," *Optics Express,* vol. 15, pp. 9385-9385, Jul 23 2007.

[13] F. Warken, E. Vetsch, D. Meschede, M. Sokolowski, and A. Rauschenbeutel, "Ultra-sensitive surface absorption spectroscopy using sub-wavelength diameter optical fibers," *Optics Express,* vol. 15, pp. 11952-11958, Sep 17 2007.

[14] F. Xu and G. Brambilla, "Demonstration of a refractometric sensor based on optical microfiber coil resonator," *Applied Physics Letters,* vol. 92, p. 101126 Mar 10 2008.

[15] F. Xu, V. Pruneri, V. Finazzi, and G. Brambilla, "An embedded optical nanowire loop resonator refractometric sensor," *Optics Express,* vol. 16, pp. 1062-1067, Jan 21 2008.

[16] F. X. Gu, L. Zhang, X. F. Yin, and L. M. Tong, "Polymer single-nanowire optical sensors," *Nano Letters,* vol. 8, pp. 2757-2761, Sep 2008.

[17] L. Zhang, F. X. Gu, J. Y. Lou, X. F. Yin, and L. M. Tong, "Fast detection of humidity with a subwavelength-diameter fiber taper coated with gelatin film," *Optics Express,* vol. 16, pp. 13349-13353, Aug 18 2008.

[18] M. Sumetsky, "Optical fiber microcoil resonator," *Optics Express,* vol. 12, pp. 2303-2316, May 17 2004.

[19] M. Sumetsky, Y. Dulashko, and A. Hale, "Fabrication and study of bent and coiled free silica nanowires: Self-coupling microloop optical interferometer," *Optics Express,* vol. 12, pp. 3521-3531, Jul 26 2004.

[20] M. Sumetsky, Y. Dulashko, J. M. Fini, and A. Hale, "Optical microfiber loop resonator," *Applied Physics Letters,* vol. 86, p. 161108, Apr 18 2005.

[21] M. Sumetsky, Y. Dulashko, J. M. Fini, A. Hale, and D. J. DiGiovanni, "The microfiber loop resonator: Theory, experiment, and application," *Journal of Lightwave Technology,* vol. 24, pp. 242-250, Jan 2006.

[22] X. S. Jiang, L. M. Tong, G. Vienne, X. Guo, A. Tsao, Q. Yang, and D. R. Yang, "Demonstration of optical microfiber knot resonators," *Applied Physics Letters,* vol. 88, p. 223501, May 29 2006.

[23] F. Xu, P. Horak, and G. Brambilla, "Conical and biconical ultra-high-Q optical-fiber nanowire microcoil resonator," *Applied Optics,* vol. 46, pp. 570-573, Feb 1 2007.

[24] F. Xu, P. Horak, and G. Brambilla, "Optimized design of microcoil resonators," *Journal of Lightwave Technology,* vol. 25, pp. 1561-1567, Jun 2007.

[25] F. Xu and G. Brambilla, "Embedding optical microfiber coil resonators in Teflon," *Optics Letters,* vol. 32, pp. 2164-2166, Aug 1 2007.

[26] L. M. Tong, R. R. Gattass, J. B. Ashcom, S. L. He, J. Y. Lou, M. Y. Shen, I. Maxwell, and E. Mazur, "Subwavelength-diameter silica wires for low-loss optical wave guiding," *Nature,* vol. 426, pp. 816-819, Dec 18 2003.

[27] S. G. Leon-Saval, T. A. Birks, W. J. Wadsworth, P. S. J. Russell, and M. W. Mason, "Supercontinuum generation in submicron fibre waveguides," *Optics Express,* vol. 12, pp. 2864-2869, Jun 28 2004.

[28] M. A. Foster and A. L. Gaeta, "Soliton-effect compression of supercontinuum to few-cycle durations in photonic nanowires," *Optics Express,* vol. 13, pp. 6848-6855, Sep 5 2005.

[29] M. A. Foster, J. M. Dudley, B. Kibler, Q. Cao, D. Lee, R. Trebino, and A. L. Gaeta, "Nonlinear pulse propagation and supercontinuum generation in photonic nanowires: experiment and simulation," *Applied Physics B-Lasers and Optics,* vol. 81, pp. 363-367, Jul 2005.

[30] D. I. Yeom, E. C. Maegi, M. R. E. Lamont, M. A. F. Roelens, L. B. Fu, and B. J. Eggleton, "Low-threshold supercontinuum generation in highly nonlinear chalcogenide nanowires," *Optics Letters,* vol. 33, pp. 660-662, Apr 1 2008.

[31] G. Brambilla, F. Koizumi, V. Finazzi, and D. J. Richardson, "Supercontinuum generation in tapered bismuth silicate fibres," *Electronics Letters,* vol. 41, pp. 795-797, Jul 7 2005.

[32] L. M. Tong, J. Y. Lou, R. R. Gattass, S. L. He, X. W. Chen, L. Liu, and E. Mazur, "Assembly of silica nanowires on silica aerogels for microphotonic devices," *Nano Letters,* vol. 5, pp. 259-262, Feb 2005.

[33] G. Brambilla and D. N. Payne, "The ultimate strength of glass silica nanowires," *Nano Letters,* vol. 9, pp. 831-835, Feb 2009.

[34] J. M. Corres, I. R. Matias, J. Bravo, and F. J. Arregui, "Tapered optical fiber biosensor for the detection of anti-gliadin antibodies," *Sensors and Actuators B-Chemical,* vol. 135, pp. 166-171, Dec 10 2008.

[35] G. Brambilla, F. Xu, P. Horak, Y. Jung, F. Koizumi, N. P. Sessions, E. Koukharenko, X. Feng, G. S. Murugan, J. S. Wilkinson, and D. J. Richardson, "Optical fiber nanowires and microwires: fabrication and applications," *Advances in Optics and Photonics,* vol. 1, pp. 107-161, Jan 1 2009.

[36] K. Okamoto, *Fundamentals of Optical Waveguides*: Academic Press, 2006.

[37] J. D. Love, W. M. Henry, W. J. Stewart, R. J. Black, S. Lacroix, and F. Gonthier, "Tapered single-mode fibers and devices .1. adiabaticity criteria," *IEE Proceedings-J Optoelectronics,* vol. 138, pp. 343-354, Oct 1991.

[38] J. Bures and R. Ghosh, "Power density of the evanescent field in the vicinity of a tapered fiber," *Journal of the Optical Society of America A-Optics Image Science and Vision,* vol. 16, pp. 1992-1996, Aug 1999.

[39] B. A. F. Puygranier and P. Dawson, "Chemical etching of optical fibre tips - experiment and model," *Ultramicroscopy,* vol. 85, pp. 235-248, Dec 2000.

[40] N. D. Herrera, O. Esteban, M. C. Navarrete, A. Gonzalez-Cano, E. Benito-Pena, and G. Orellana, "Improved performance of SPR sensors by a chemical etching of tapered optical fibers," *Optics and Lasers in Engineering,* vol. 49, pp. 1065-1068, Aug 2011.

[41] T. A. Birks and Y. W. Li, "The shape of fiber tapers," *IEEE Journal of Lightwave Technology,* vol. 10, pp. 432-438, Apr 1992.

[42] http://www.bath.ac.uk/physics/groups/cppm/tapers.php.

[43] Y. Xia, J. A. Rogers, K. E. Paul, and G. M. Whitesides, "Unconventional methods for fabricating and patterning nanostructures," *Chemical Reviews,* vol. 99, pp. 1823-1848, Jul 14 1999.

[44] W. B. Glendinning and J. N. Helbert, *Handbook of VLSI microlithography: principles, technology, and applications (Second Edition)*: William Andrew, 2001.

[45] R. F. W. Pease, "Nanolithography and its prospects as a manufacturing technology," *Journal of Vacuum Science & Technology B,* vol. 10, pp. 278-285, Jan 1992.

[46] M. Born and E. Wolf, *Principle of Optics*. New York: Springer, 1999.

[47] K. J. Vahala, "Optical microcavities," *Nature,* vol. 424, pp. 839-846, Aug 14 2003.

[48] J. L. Kou, J. Feng, L. Ye, F. Xu, and Y. Q. Lu, "Miniaturized fiber taper reflective interferometer for high temperature measurement," *Optics Express,* vol. 18, pp. 14245-14250, Jun 21 2010.

[49] Y. J. Rao, "In-fibre Bragg grating sensors," *Measurement Science & Technology,* vol. 8, pp. 355-375, Apr 1997.

[50] G. Coviello, V. Finazzi, J. Villatoro, and V. Pruneri, "Thermally stabilized PCF-based sensor for temperature measurements up to 1000 °C," *Optics Express,* vol. 17, pp. 21551-21559, Nov 23 2009.

[51] D. Grobnic, S. J. Mihailov, C. W. Smelser, and H. M. Ding, "Sapphire fiber Bragg grating sensor made using femtosecond laser radiation for ultrahigh temperature applications," *IEEE Photonics Technology Letters,* vol. 16, pp. 2505-2507, Nov 2004.

[52] J. Canning, M. Stevenson, S. Bandyopadhyay, and K. Cook, "Extreme silica optical fibre gratings," *Sensors,* vol. 8, pp. 6448-6452, Oct 2008.

[53] K. O. Hill and G. Meltz, "Fiber Bragg grating technology fundamentals and overview," *Journal of Lightwave Technology,* vol. 15, pp. 1263-1276, Aug 1997.

[54] A. D. Kersey, M. A. Davis, H. J. Patrick, M. LeBlanc, K. P. Koo, C. G. Askins, M. A. Putnam, and E. J. Friebele, "Fiber grating sensors," *Journal of Lightwave Technology,* vol. 15, pp. 1442-1463, Aug 1997.

[55] M. Sumetsky and J. M. Fini, "Surface nanoscale axial photonics," *Optics Express,* vol. 19, pp. 26470-26485, Dec 19 2011.

[56] S. Sederberg and A. Y. Elezzabi, "Nanoscale plasmonic contour bowtie antenna operating in the mid-infrared," *Optics Express,* vol. 19, pp. 15532-15537, Aug 1 2011.

[57] E. X. Jin and X. F. Xu, "Enhanced optical near field from a bowtie aperture," *Applied Physics Letters,* vol. 88, p. 153110, Apr 10 2006.

[58] S. G. Lipson, H. Lipson, and D. S. Tannhauser, *Optical Physics*: Cambridge Univerisity Press, 2005.

[59] N. Fang, H. Lee, C. Sun, and X. Zhang, "Sub-diffraction-limited optical imaging with a silver superlens," *Science,* vol. 308, pp. 534-537, Apr 22 2005.

[60] A. Salandrino and N. Engheta, "Far-field subdiffraction optical microscopy using metamaterial crystals: Theory and simulations," *Physical Review B,* vol. 74, p. 075103, Aug 2006.

[61] V. M. Shalaev, "Optical negative-index metamaterials," *Nature Photonics,* vol. 1, pp. 41-48, Jan 2007.

[62] Z. W. Liu, H. Lee, Y. Xiong, C. Sun, and X. Zhang, "Far-field optical hyperlens magnifying sub-diffraction-limited objects," *Science,* vol. 315, p. 1686, Mar 23 2007.

[63] X. Zhang and Z. W. Liu, "Superlenses to overcome the diffraction limit," *Nature Materials,* vol. 7, pp. 435-441, Jun 2008.

[64] Q. F. Xu, V. R. Almeida, R. R. Panepucci, and M. Lipson, "Experimental demonstration of guiding and confining light in nanometer-size low-refractive-index material," *Optics Letters,* vol. 29, pp. 1626-1628, Jul 15 2004.

[65] G. S. Wiederhecker, C. M. B. Cordeiro, F. Couny, F. Benabid, S. A. Maier, J. C. Knight, C. H. B. Cruz, and H. L. Fragnito, "Field enhancement within an optical fibre with a subwavelength air core," *Nature Photonics,* vol. 1, pp. 115-118, Feb 2007.

[66] X. Wang, J. Fu, X. Liu, and L. M. Tong, "Subwavelength focusing by a micro/nanofiber array," *Journal of the Optical Society of America A-Optics Image Science and Vision,* vol. 26, pp. 1827-1833, Aug 2009.

[67] J. A. Fu, H. T. Dong, and W. Fang, "Subwavelength focusing of light by a tapered microtube," *Applied Physics Letters,* vol. 97, p. 041114, Jul 26 2010.

[68] E. Betzig and J. K. Trautman, "Near-field optics - microscopy, spectroscopy, and surface modification beyond the diffraction limit," *Science,* vol. 257, pp. 189-195, Jul 10 1992.

[69] H. Heinzelmann and D. W. Pohl, "Scanning near-field optical microscopy," *Applied Physics A-Materials Science & Processing,* vol. 59, pp. 89-101, Aug 1994.

[70] L. Novotny, D. W. Pohl, and B. Hecht, "Light confinement in scanning near-field optical microscopy," *Ultramicroscopy,* vol. 61, pp. 1-9, Dec 1995.

[71] S. A. Maier, P. G. Kik, H. A. Atwater, S. Meltzer, E. Harel, B. E. Koel, and A. A. G. Requicha, "Local detection of electromagnetic energy transport below the

diffraction limit in metal nanoparticle plasmon waveguides," *Nature Materials,* vol. 2, pp. 229-232, Apr 2003.

[72] W. L. Barnes, A. Dereux, and T. W. Ebbesen, "Surface plasmon subwavelength optics," *Nature,* vol. 424, pp. 824-830, Aug 14 2003.

[73] R. Zia, M. D. Selker, P. B. Catrysse, and M. L. Brongersma, "Geometries and materials for subwavelength surface plasmon modes," *Journal of the Optical Society of America A-Optics Image Science and Vision,* vol. 21, pp. 2442-2446, Dec 2004.

[74] F. Festy, A. Demming, and D. Richards, "Resonant excitation of tip plasmons for tip-enhanced Raman SNOM," *Ultramicroscopy,* vol. 100, pp. 437-441, Aug 2004.

[75] V. Veselago, "Electrodynamics of substance with simultaneously negative electrical and magnetical permeabilites," *Soviet Physics Uspekhi,* vol. 10, pp. 509-514, 1968.

[76] J. B. Pendry, "Negative refraction makes a perfect lens," *Physical Review Letters,* vol. 85, pp. 3966-3969, Oct 30 2000.

[77] M. Bayindir, K. Aydin, E. Ozbay, P. Markos, and C. M. Soukoulis, "Transmission properties of composite metamaterials in free space," *Applied Physics Letters,* vol. 81, pp. 120-122, Jul 1 2002.

[78] E. H. Synge, "A suggested model for extending microscopic resolution into ultra-microscopic region," *Philosophical Magazine,* vol. 6, pp. 356-362, 1928.

[79] B. Hecht, B. Sick, U. P. Wild, V. Deckert, R. Zenobi, O. J. F. Martin, and D. W. Pohl, "Scanning near-field optical microscopy with aperture probes: Fundamentals and applications," *Journal of Chemical Physics,* vol. 112, pp. 7761-7774, May 8 2000.

[80] D. Courjon and C. Bainier, "Near-field microscopy and near-field optics," *Reports on Progress in Physics,* vol. 57, pp. 989-1028, Oct 1994.

[81] D. Zeisel, S. Nettesheim, B. Dutoit, and R. Zenobi, "Pulsed laser-induced desorption and optical imaging on a nanometer scale with scanning near-field microscopy using chemically etched fiber tips," *Applied Physics Letters,* vol. 68, pp. 2491-2492, Apr 29 1996.

[82] R. Stevenson, R. Riehn, R. G. Milner, D. Richards, E. Moons, D. J. Kang, M. Blamire, J. Morgado, and F. Cacialli, "Ultraviolet-visible near-field microscopy of phase-separated blends of polyfluorene-based conjugated semiconductors," *Applied Physics Letters,* vol. 79, pp. 833-835, Sep 17 2001.

[83] D. Credgington, O. Fenwick, A. Charas, J. Morgado, K. Suhling, and F. Cacialli, "High-resolution scanning near-field optical lithography of conjugated polymers," *Advanced Functional Materials,* vol. 20, pp. 2842-2847, Sep 9 2010.

[84] W. Ding, S. R. Andrews, and S. A. Maier, "Internal excitation and superfocusing of surface plasmon polaritons on a silver-coated optical fiber tip," *Physical Review A,* vol. 75, p. 063822, Jun 2007.

[85] T. J. Antosiewicz, P. Wrobel, and T. Szoplik, "Superfocusing on a dielectric-metal-dielectric apertureless scanning near-field optical microscope probe," *ICTON: 2009 11th International Conference on Transparent Optical Networks,* pp. 1-4, 2009.

[86] L. Novotny, D. W. Pohl, and B. Hecht, "Scanning near-field optical probe with ultrasmall spot size," *Optics Letters,* vol. 20, pp. 970-972, May 1 1995.

[87] J. A. Veerman, A. M. Otter, L. Kuipers, and N. F. van Hulst, "High definition aperture probes for near-field optical microscopy fabricated by focused ion beam milling," *Applied Physics Letters,* vol. 72, pp. 3115-3117, Jun 15 1998.

[88] L. Novotny, D. W. Pohl, and P. Regli, "Light propagation through nanometer-sized structures - the two-dimensional-aperture scanning near-field optical microscope," *Journal of the Optical Society of America A,* vol. 11, pp. 1768-1779, Jun 1994.

[89] R. Riehn, A. Charas, J. Morgado, and F. Cacialli, "Near-field optical lithography of a conjugated polymer," *Applied Physics Letters,* vol. 82, pp. 526-528, Jan 27 2003.

[90] F. Renna, D. Cox, and G. Brambilla, "Efficient sub-wavelength light confinement using surface plasmon polaritons in tapered fibers," *Optics Express,* vol. 17, pp. 7658-7663, Apr 27 2009.

[91] F. Renna, G. Brambilla, and D. C. Cox, "Light confinement in optical fibers using surface plasmon polaritons," *IEEE Photonics Technology Letters,* vol. 21, pp. 1508-1510, Oct 15 2009.

[92] D. A. Parthenopoulos and P. M. Rentzepis, "Three-dimensional optical storage memory," *Science,* vol. 245, pp. 843-845, Aug 25 1989.

[93] E. N. Glezer, M. Milosavljevic, L. Huang, R. J. Finlay, T. H. Her, J. P. Callan, and E. Mazur, "Three-dimensional optical storage inside transparent materials," *Optics Letters,* vol. 21, pp. 2023-2025, Dec 15 1996.

[94] J. F. Heanue, M. C. Bashaw, and L. Hesselink, "Volume Holographic Storage and Retrieval of Digital Data," *Science,* vol. 265, pp. 749-752, Aug 5 1994.

[95] D. Psaltis and G. W. Burr, "Holographic data storage," *IEEE Computer,* vol. 31, pp. 52-60, Feb 1998.

[96] T. Roy, E. T. F. Rogers, and N. I. Zheludev, "Sub-wavelength focusing meta-lens," *Optics Express,* vol. 21, pp. 7577-7582, 2013.

[97] L. P. Pitaevskii, "Electric forces in a transparent dispersive medium," *Soviet Physics Jetp-Ussr,* vol. 12, pp. 1008-1031, 1961.

[98] J. P. v. d. Ziel, P. S. Pershan, and L. D. Malmstrom, "Optically-induced magnetization resulting from the inverse Faraday effect," *Physical Review Letters,* vol. 15, pp. 190-193, Aug 2 1965.

[99] A. V. Kimel, A. Kirilyuk, P. A. Usachev, R. V. Pisarev, A. M. Balbashov, and T. Rasing, "Ultrafast non-thermal control of magnetization by instantaneous photomagnetic pulses," *Nature,* vol. 435, pp. 655-657, Jun 2 2005.

[100] C. D. Stanciu, F. Hansteen, A. V. Kimel, A. Tsukamoto, A. Itoh, A. Kirilyuk, and T. Rasing, "Ultrafast interaction of the angular momentum of photons with spins in the metallic amorphous alloy GdFeCo," *Physical Review Letters,* vol. 98, p. 207401, May 18 2007.

[101] F. Hansteen, A. Kimel, A. Kirilyuk, and T. Rasing, "Femtosecond photomagnetic switching of spins in ferrimagnetic garnet films," *Physical Review Letters,* vol. 95, p. 047402, Jul 22 2005.

[102] A. V. Kimel, A. Kirilyuk, F. Hansteen, R. V. Pisarev, and T. Rasing, "Nonthermal optical control of magnetism and ultrafast laser-induced spin dynamics in solids," *Journal of Physics-Condensed Matter,* vol. 19, p. 043201, Jan 31 2007.

[103] P. Moar, F. Ladouceur, and L. Cahill, "Numerical analysis of the transmission efficiency of heat-drawn and chemically etched scanning near-field optical microscopes," *Applied Optics,* vol. 39, pp. 1966-1972, Apr 20 2000.

[104] P. Hoffmann, B. Dutoit, and R. P. Salathe, "Comparison of mechanically drawn and protection layer chemically etched optical fiber tips," *Ultramicroscopy,* vol. 61, pp. 165-170, Dec 1995.

[105] C. Lehrer, L. Frey, S. Petersen, T. Sulzbach, O. Ohlsson, T. Dziomba, H. U. Danzebrink, and H. Ryssel, "Fabrication of silicon aperture probes for scanning near-field optical microscopy by focused ion beam nano machining," *Microelectronic Engineering,* vol. 57-8, pp. 721-728, Sep 2001.

[106] S. Nagai, K. Takehisa, T. Enami, T. Nishisaka, J. Fujimoto, O. Wakabayashi, H. Mizoguchi, and A. Takahashi, "Development of a 2 kHz F_2 laser for 157 nm lithography," *Japanese Journal of Applied Physics* vol. 38, pp. 7013-7016, Dec 1999.

[107] J. E. Bjorkholm, "EUV lithography- the successor to optical lithography?," *Intel Technology Journal,* vol. Q3'98, pp. 1-8, 1998.

[108] P. A. Zimmerman, C. van Peski, B. Rice, J. Byers, N. J. Turro, X. Lei, J. L. Gejo, V. Liberman, S. Palmacci, M. Rothschild, A. Whittaker, I. Blakey, L. Chen, B. Dargaville, and H. P. Liu, "Status of high-index materials for Generation-three 193nm immersion lithography," *Journal of Photopolymer Science and Technology,* vol. 20, pp. 643-650, 2007.

[109] Y. Lin, M. H. Hong, W. J. Wang, Y. Z. Law, and T. C. Chong, "Sub-30 nm lithography with near-field scanning optical microscope combined with femtosecond laser," *Applied Physics A,* vol. 80, pp. 461-465, Feb 2005.

[110] B. Q. Wu, "Next-generation lithography for 22 and 16 nm technology nodes and beyond," *Science China,* vol. 54, pp. 959-979, May 2011.

[111] R. Ghaida and P. Zarkesh-Ha, "A layout sensitivity model for estimating electromigration-vulnerable narrow interconnects," *Journal of Electronic Testing,* vol. 25, pp. 67-77, Feb 2009.

[112] Y. Kim, J. Masson, and K. S. Booksh, "Single-crystal sapphire-fiber optic sensors based on surface plasmon resonance spectroscopy for in situ monitoring," *Talanta,* vol. 67, pp. 908-917, Oct 31 2005.

[113] G. Vienne, K. Eason, Z. X. Xie, Y. T. Lim, and J. M. Li, "Magnetic field induced by various input beam polarizations in all-optical magnetic recording," *Japanese Journal of Applied Physics,* vol. 50, p. 09MD03, Sep 2011.

[114] A. V. Kimel, A. Kirilyuk, and T. Rasing, "Femtosecond opto-magnetism: ultrafast laser manipulation of magnetic materials," *Laser & Photonics Reviews,* vol. 1, pp. 275-287, Nov 2007.

[115] S. Maier, *Plasmonics: Fundamentals and Applications*. New York: Springer, 2007.

[116] W. A. Challener, C. B. Peng, A. V. Itagi, D. Karns, W. Peng, Y. G. Peng, X. M. Yang, X. B. Zhu, N. J. Gokemeijer, Y. T. Hsia, G. Ju, R. E. Rottmayer, M. A. Seigler, and E. C. Gage, "Heat-assisted magnetic recording by a near-field transducer with efficient optical energy transfer," *Nature Photonics,* vol. 3, pp. 220-224, May 2009.

[117] A. W. Wark, H. J. Lee, and R. M. Corn, "Long-range surface plasmon resonance imaging for bioaffinity sensors," *Analytical Chemistry,* vol. 77, pp. 3904-3907, Jul 1 2005.

[118] J. Ctyroky, J. Homola, P. V. Lambeck, S. Musa, H. J. W. M. Hoekstra, R. D. Harris, J. S. Wilkinson, B. Usievich, and N. M. Lyndin, "Theory and modelling of optical waveguide sensors utilising surface plasmon resonance," *Sensors and Actuators B-Chemical,* vol. 54, pp. 66-73, Jan 25 1999.

[119] P. Westphal and A. Bornmann, "Biornolecular detection by surface plasmon enhanced ellipsometry," *Sensors and Actuators B-Chemical,* vol. 84, pp. 278-282, May 15 2002.

[120] N. A. Issa and R. Guckenberger, "Optical nanofocusing on tapered metallic waveguides," *Plasmonics,* vol. 2, pp. 31-37, Mar 2007.

[121] J. M. McMahon, S. K. Gray, and G. C. Schatz, "Optical properties of nanowire dimers with a spatially nonlocal dielectric function," *Nano Letters,* vol. 10, pp. 3473-3481, Sep 2010.

[122] F. J. G. de Abajo, "Nonlocal Effects in the Plasmons of Strongly Interacting Nanoparticles, Dimers, and Waveguides," *Journal of Physical Chemistry C,* vol. 112, pp. 17983-17987, Nov 20 2008.

[123] Y. M. Jung, G. Brambilla, and D. J. Richardson, "Broadband single-mode operation of standard optical fibers by using a sub-wavelength optical wire filter," *Optics Express,* vol. 16, pp. 14661-14667, Sep 15 2008.

[124] M. N. Zervas and I. P. Giles, "Optical-Fibre Surface-Plasmon-Wave Polarizers with Enhanced Performance," *Electronics Letters,* vol. 25, pp. 321-323, Mar 2 1989.

[125] A. Ambrosio, O. Fenwick, F. Cacialli, R. Micheletto, Y. Kawakami, P. G. Gucciardi, D. J. Kang, and M. Allegrini, "Shape dependent thermal effects in apertured fiber probes for scanning near-field optical microscopy," *Journal of Applied Physics,* vol. 99, p. 084303, Apr 15 2006.

[126] A. M. Vengsarkar, J. R. Pedrazzani, J. B. Judkins, P. J. Lemaire, N. S. Bergano, and C. R. Davidson, "Long-period fiber-grating-based gain equalizers," *Optics Letters,* vol. 21, pp. 336-338, Mar 1 1996.

[127] B. J. Eggleton, P. S. Westbrook, C. A. White, C. Kerbage, R. S. Windeler, and G. L. Burdge, "Cladding-mode-resonances in air-silica microstructure optical fibers," *Journal of Lightwave Technology,* vol. 18, pp. 1084-1100, Aug 2000.

[128] Y. P. Wang, D. N. Wang, W. Jin, Y. J. Rao, and G. D. Peng, "Asymmetric long period fiber gratings fabricated by use of CO_2 laser to carve periodic grooves on the optical fiber," *Applied Physics Letters,* vol. 89, p. 151105, Oct 9 2006.

[129] J. S. Petrovic, H. Dobb, V. K. Mezentsev, K. Kalli, D. J. Webb, and I. Bennion, "Sensitivity of LPGs in PCFs fabricated by an electric arc to temperature, strain, and external refractive index," *Journal of Lightwave Technology,* vol. 25, pp. 1306-1312, May 2007.

[130] Y. Kondo, K. Nouchi, T. Mitsuyu, M. Watanabe, P. G. Kazansky, and K. Hirao, "Fabrication of long-period fiber gratings by focused irradiation of infrared femtosecond laser pulses," *Optics Letters,* vol. 24, pp. 646-648, May 15 1999.

[131] S. Savin, M. J. F. Digonnet, G. S. Kino, and H. J. Shaw, "Tunable mechanically induced long-period fiber gratings," *Optics Letters,* vol. 25, pp. 710-712, May 15 2000.

[132] C. Y. Lin and L. A. Wang, "Loss-tunable long period fibre grating made from etched corrugation structure," *Electronics Letters,* vol. 35, pp. 1872-1873, Oct 14 1999.

[133] G. Meltz, W. W. Morey, and W. H. Glenn, "Formation of Bragg gratings in optical fibers by a transverse holographic method," *Optics Letters,* vol. 14, pp. 823-825, Aug 1 1989.

[134] K. O. Hill, B. Malo, F. Bilodeau, D. C. Johnson, and J. Albert, "Bragg gratings fabricated in monomode photosensitive optical-fiber by UV exposure through a phase mask," *Applied Physics Letters,* vol. 63, pp. 1035-1037, Jul 19 1993.

[135] G. Pakulski, R. Moore, C. Maritan, F. Shepherd, M. Fallahi, I. Templeton, and G. Champion, "Fused-silica masks for printing uniform and phase adjusted gratings for distributed feedback lasers," *Applied Physics Letters,* vol. 62, pp. 222-224, Jan 18 1993.

[136] M. J. Cole, W. H. Loh, R. I. Laming, M. N. Zervas, and S. Barcelos, "Moving fibre/phase mask-scanning beam technique for enhanced flexibility in

producing fiber gratings with uniform phase mask," *Electronics Letters,* vol. 31, pp. 1488-1490, Aug 17 1995.

[137] D. C. Johnson, F. Bilodeau, B. Malo, K. O. Hill, P. G. J. Wigley, and G. I. Stegeman, "Long-length, long-period rocking filters fabricated from conventional monomode telecommunications optical fiber," *Optics Letters,* vol. 17, pp. 1635-1637, Nov 15 1992.

[138] R. Kashyap, *Fiber Bragg Grating*: Academic Press, 2010.

[139] K. O. Hill, Y. Fujii, D. C. Johnson, and B. S. Kawasaki, "Photosensitivity in optical fiber waveguides - application to reflection filter fabrication," *Applied Physics Letters,* vol. 32, pp. 647-649, May 15 1978.

[140] B. S. Kawasaki, K. O. Hill, D. C. Johnson, and Y. Fujii, "Narrow-band Bragg reflectors in optical fibers," *Optics Letters,* vol. 3, pp. 66-68, Aug 1 1978.

[141] C. W. Smelser, S. J. Mihailov, and D. Grobnic, "Hydrogen loading for fiber grating writing with a femtosecond laser and a phase mask," *Optics Letters,* vol. 29, pp. 2127-2129, Sep 15 2004.

[142] A. Dragomir, D. N. Nikogosyan, K. A. Zagorulko, P. G. Kryukov, and E. M. Dianov, "Inscription of fiber Bragg gratings by ultraviolet femtosecond radiation," *Optics Letters,* vol. 28, pp. 2171-2173, Nov 15 2003.

[143] H. F. Xuan, W. Jin, and S. J. Liu, "Long-period gratings in wavelength-scale microfibers," *Optics Letters,* vol. 35, pp. 85-87, Jan 1 2010.

[144] R. Kashyap, P. F. Mckee, and D. Armes, "UV written reflection grating structures in photosensitive optical fibers using phase-shifted phase masks," *Electronics Letters,* vol. 30, pp. 1977-1978, Nov 10 1994.

[145] D. K. Armani, T. J. Kippenberg, S. M. Spillane, and K. J. Vahala, "Ultra-high-Q toroid microcavity on a chip," *Nature,* vol. 421, pp. 925-928, Feb 27 2003.

[146] M. L. Gorodetsky, A. A. Savchenkov, and V. S. Ilchenko, "On the ultimate Q of optical microsphere resonators," *Optics Letters,* vol. 21, pp. 453-455, Apr 1 1996.

[147] B. Gayral, J. M. Gerard, A. Lemaitre, C. Dupuis, L. Manin, and J. L. Pelouard, "High-Q wet-etched GaAs microdisks containing InAs quantum boxes," *Applied Physics Letters,* vol. 75, pp. 1908-1910, Sep 27 1999.

[148] O. Painter, R. K. Lee, A. Scherer, A. Yariv, J. D. O'Brien, P. D. Dapkus, and I. Kim, "Two-dimensional photonic band-gap defect mode laser," *Science,* vol. 284, pp. 1819-1821, Jun 11 1999.

[149] J. M. Gerard, D. Barrier, J. Y. Marzin, R. Kuszelewicz, L. Manin, E. Costard, V. ThierryMieg, and T. Rivera, "Quantum boxes as active probes for photonic microstructures: The pillar microcavity case," *Applied Physics Letters,* vol. 69, pp. 449-451, Jul 22 1996.

[150] G. P. Agrawal and S. Radic, "Phase-shifted fiber Bragg gratings and their application for wavelength demultiplexing," *IEEE Photonics Technology Letters,* vol. 6, pp. 995-997, Aug 1994.

[151] T. A. Birks and Y. W. Li, "The shape of fiber tapers," *Journal of Lightwave Technology,* vol. 10, pp. 432-438, Apr 1992.

[152] Y. M. Jung, G. Brambilla, and D. J. Richardson, "Optical microfiber coupler for broadband single-mode operation," *Optics Express,* vol. 17, pp. 5273-5278, Mar 30 2009.

[153] R. Feced and M. N. Zervas, "Effects of random phase and amplitude errors in optical fiber Bragg gratings," *Journal of Lightwave Technology,* vol. 18, pp. 90-101, Jan 2000.

[154] G. Brambilla, F. Xu, and X. Feng, "Fabrication of optical fibre nanowires and their optical and mechanical characterisation," *Electronics Letters,* vol. 42, pp. 517-519, Apr 27 2006.

[155] N. Lou, R. Jha, J. L. Dominguez-Juarez, V. Finazzi, J. Villatoro, G. Badenes, and V. Pruneri, "Embedded optical micro/nano-fibers for stable devices," *Optics Letters,* vol. 35, pp. 571-573, Feb 15 2010.

[156] F. Xu and G. Brambilla, "Preservation of micro-optical fibers by embedding," *Japanese Journal of Applied Physics,* vol. 47, pp. 6675-6677, Aug 2008.

[157] J. Wilson and J. Hawkes, *Optoelectronics: An Introduction*. Essex: Prentice Hall 1998.

[158] R. Zengerle and O. Leminger, "Phase-shifted Bragg-Grating filters with improved transmission characteristics," *Journal of Lightwave Technology,* vol. 13, pp. 2354-2358, Dec 1995.

[159] J. M. Gerard, B. Sermage, B. Gayral, B. Legrand, E. Costard, and V. Thierry-Mieg, "Enhanced spontaneous emission by quantum boxes in a monolithic optical microcavity," *Physical Review Letters,* vol. 81, pp. 1110-1113, Aug 3 1998.

[160] J. Feng, M. Ding, J. L. Kou, F. Xu, and Y. Q. Lu, "An optical fiber tip micrograting thermometer," *IEEE Photonics Journal,* vol. 3, pp. 810-814, Oct 2011.

[161] J. L. Kou, S. J. Qiu, F. Xu, and Y. Q. Lu, "Demonstration of a compact temperature sensor based on first-order Bragg grating in a tapered fiber probe," *Optics Express,* vol. 19, pp. 18452-18457, Sep 12 2011.

[162] V. de Oliveira, M. Muller, and H. J. Kalinowski, "Bragg gratings in standard nonhydrogenated fibers for high-temperature sensing," *Applied Optics,* vol. 50, pp. E55-E58, Sep 1 2011.

[163] D. Barrera, V. Finazzi, J. Villatoro, S. Sales, and V. Pruneri, "Packaged optical sensors based on regenerated fiber Bragg gratings for high temperature applications," *IEEE Sensors Journal,* vol. 12, pp. 107-112, Jan 2012.

[164] H. R. Guo, F. F. Pang, X. L. Zeng, N. Chen, Z. Y. Chen, and T. Y. Wang, "Temperature sensor using an optical fiber coupler with a thin film," *Applied Optics,* vol. 47, pp. 3530-3534, Jul 1 2008.

[165] F. Hamer and J. Hamer, *The Potter's Dictionary of Materials and Techniques, Fifth Edition*. Philadelphia: University of Pennsylvania Press, 2004.

[166] F. P. Payne, C. D. Hussey, and M. S. Yataki, "Polarization analysis of strongly fused and weakly fused tapered couplers," *Electronics Letters,* vol. 21, pp. 561-563, Jun 20 1985.

[167] J. H. Wray and J. T. Neu, "Refractive index of several glasses as a function of wavelength and temperature," *Journal of the Optical Society of America,* vol. 59, pp. 774-776, Jun 1 1969.

[168] D. B. Leviton and B. J. Frey, "Temperature-dependent absolute refractive index measurements of synthetic fused silica - art. no. 62732K," *Optomechanical Technologies for Astronomy, Pts 1 and 2,* vol. 6273, pp. K2732-K2732, 2006.

[169] C. Rodenburg, X. Liu, M. A. E. Jepson, S. A. Boden, and G. Brambilla, "Surface morphology of silica nanowires at the nanometer scale," *Journal of Non-Crystalline Solids,* vol. 357, pp. 3042-3045, Jul 15 2011.

[170] F. P. Incorpera, D. P. DeWitt, T. L. Bergman, and A. S. Lavine, *Fundamentals of Heat and Mass Transfer* John Wiley & Sons, 2007.

[171] A. J. C. Grellier, N. K. Zayer, and C. N. Pannell, "Heat transfer modelling in CO_2 laser processing of optical fibres," *Optics Communications,* vol. 152, pp. 324-328, Jul 1 1998.

[172] M. Ding, P. F. Wang, and G. Brambilla, "A microfiber coupler tip thermometer," *Optics Express,* vol. 20, pp. 5402-5408, Feb 27 2012.

[173] C. Jesus, P. Caldas, O. Frazao, J. L. Santos, P. A. S. Jorge, and J. M. Baptista, "Simultaneous measurement of refractive index and temperature using a hybrid fiber Bragg grating/long-period fiber frating configuration," *Fiber and Integrated Optics,* vol. 28, pp. 440-449, 2009.

[174] V. S. Ilchenko and A. B. Matsko, "Optical resonators with whispering-gallery modes - Part II: Applications," *IEEE Journal of Selected Topics in Quantum Electronics,* vol. 12, pp. 15-32, Jan-Feb 2006.

[175] D. W. Vernooy, V. S. Ilchenko, H. Mabuchi, E. W. Streed, and H. J. Kimble, "High-Q measurements of fused-silica microspheres in the near infrared," *Optics Letters,* vol. 23, pp. 247-249, Feb 15 1998.

[176] M. Sumetsky, "Whispering-gallery-bottle microcavities: the three-dimensional etalon," *Optics Letters,* vol. 29, pp. 8-10, Jan 1 2004.

[177] M. N. Zervas, G. S. Murugan, and J. S. Wilkinson, "Demonstration of novel high-Q fibre WGM "bottle" microresonators," *ICTON 2008: Proceedings of 2008 10th Anniversary International Conference on Transparent Optical Networks,* vol. 4, pp. 58-60, Jun 2008.

[178] G. S. Murugan, J. S. Wilkinson, and M. N. Zervas, "Experimental demonstration of a bottle microresonator," *2009 Conference on Lasers and Electro-Optics and Quantum Electronics and Laser Science Conference (CLEO/QELS 2009),* pp. 2925-2926, Jun 2009.

[179] G. S. Murugan, J. S. Wilkinson, and M. N. Zervas, "Selective excitation of whispering gallery modes in a novel bottle microresonator," *Optics Express,* vol. 17, pp. 11916-11925, Jul 6 2009.

[180] M. Pollinger, D. O'Shea, F. Warken, and A. Rauschenbeutel, "Ultrahigh-Q tunable whispering-gallery-mode microresonator," *Physical Review Letters,* vol. 103, p. 053901, Jul 31 2009.

[181] G. S. Murugan, J. S. Wilkinson, and M. N. Zervas, "Optical excitation and probing of whispering gallery modes in bottle microresonators: potential for all-fiber add-drop filters," *Optics Letters,* vol. 35, pp. 1893-1895, Jun 1 2010.

[182] J. M. Ward, D. G. O'Shea, B. J. Shortt, M. J. Morrissey, K. Deasy, and S. G. N. Chormaic, "Heat-and-pull rig for fiber taper fabrication," *Review of Scientific Instruments,* vol. 77, p. 083105, Aug 2006.

[183] G. S. Murugan, M. N. Petrovich, Y. Jung, J. S. Wilkinson, and M. N. Zervas, "Hollow-bottle optical microresonators," *Optics Express,* vol. 19, pp. 20773-20784, Oct 10 2011.

[184] A. A. Savchenkov, A. B. Matsko, D. Strekalov, V. S. Ilchenko, and L. Maleki, "Mode filtering in optical whispering gallery resonators," *Electronics Letters,* vol. 41, pp. 495-497, Apr 14 2005.

[185] Y. Louyer, D. Meschede, and A. Rauschenbeutel, "Tunable whispering-gallery-mode resonators for cavity quantum electrodynamics," *Physical Review A,* vol. 72, p. 031801, Sep 2005.

[186] D. Gloge, "Weakly Guiding Fibers," *Applied Optics,* vol. 10, pp. 2252-2258, Oct 1 1971.

[187] S. Schiller and R. L. Byer, "High-resolution spectroscopy of whispering gallery modes in large dielectric spheres," *Optics Letters,* vol. 16, pp. 1138-1140, Aug 1 1991.

[188] C. C. Lam, P. T. Leung, and K. Young, "Explicit asymptotic formulas for the positions, widths, and strengths of resonances in Mie scattering," *Journal of the Optical Society of America B,* vol. 9, pp. 1585-1592, Sep 1992.

[189] H. Raether, *Surface Plasmons* vol. 111. New York: Springer-Verlag, 1988.

[190] J. J. Burke, G. I. Stegeman, and T. Tamir, "Surface-polariton-like waves guided by thin, lossy metal-films," *Physical Review B,* vol. 33, pp. 5186-5201, Apr 15 1986.

[191] M. N. Zervas, "Surface-plasmon polariton waves guided by thin metal-films," *Optics Letters,* vol. 16, pp. 720-722, May 15 1991.

[192] E. N. Economou, "Surface plasmons in thin films," *Physical Review* vol. 182, pp. 539-554, Jun 1969.

[193] P. Berini, "Long-range surface plasmon polaritons," *Advances in Optics and Photonics,* vol. 1, pp. 484-588, Nov 1 2009.

[194] C. L. Lee, "Spectral analysis of waveguide tapered microfiber with an ultrathin metal coating," *Optics Express,* vol. 18, pp. 14768-14777, Jul. 2010.

[195] S. J. Albader and M. Imtaar, "Azimuthally uniform surface-plasma modes in thin metallic cylindrical-shells," *IEEE Journal of Quantum Electronics,* vol. 28, pp. 525-533, Feb 1992.

[196] S. J. Albader and M. Imtaar, "TM-polarized surface-plasma modes on metal-coated dielectric cylinders," *Journal of Lightwave Technology,* vol. 10, pp. 865-872, Jul 1992.

[197] J. Takahara, S. Yamagishi, H. Taki, A. Morimoto, and T. Kobayashi, "Guiding of a one-dimensional optical beam with nanometer diameter," *Optics Letters,* vol. 22, pp. 475-477, Apr 1 1997.

[198] S. A. Maier, M. L. Brongersma, P. G. Kik, S. Meltzer, A. A. G. Requicha, and H. A. Atwater, "Plasmonics - A route to nanoscale optical devices," *Advanced Materials,* vol. 13, pp. 1501-1505, Oct 2 2001.

[199] M. Mansuripur, A. R. Zakharian, A. Lesuffleur, S. H. Oh, R. J. Jones, N. C. Lindquist, H. Im, A. Kobyakov, and J. V. Moloney, "Plasmonic nano-structures for optical data storage," *Optics Express,* vol. 17, pp. 14001-14014, Aug 3 2009.

[200] J. A. Schuller, E. S. Barnard, W. S. Cai, Y. C. Jun, J. S. White, and M. L. Brongersma, "Plasmonics for extreme light concentration and manipulation," *Nature Materials,* vol. 9, pp. 193-204, Mar 2010.

[201] J. Villatoro, D. Monzon-Hernandez, and E. Mejia, "Fabrication and modeling of uniform-waist single-mode tapered optical fiber sensors," *Applied Optics,* vol. 42, pp. 2278-2283, May 1 2003.

[202] A. Diez, M. V. Andres, and J. L. Cruz, "In-line fiber-optic sensors based on the excitation of surface plasma modes in metal-coated tapered fibers," *Sensors and Actuators B: Chemical,* vol. 73, pp. 95-99, Mar 10 2001.

[203] N. A. Janunts, K. S. Baghdasaryan, K. V. Nerkararyan, and B. Hecht, "Excitation and superfocusing of surface plasmon polaritons on a silver-coated optical fiber tip," *Optics Communications,* vol. 253, pp. 118-124, Sep 1 2005.

[204] D. F. P. Pile and D. K. Gramotnev, "Adiabatic and nonadiabatic nanofocusing of plasmons by tapered gap plasmon waveguides," *Applied Physics Letters,* vol. 89, p. 041111, Jul 24 2006.

[205] B. Lee, I. M. Lee, S. Kim, D. H. Oh, and L. Hesselink, "Review on subwavelength confinement of light with plasmonics," *Journal of Modern Optics,* vol. 57, pp. 1479-1497, 2010.

[206] H. C. Guo, T. P. Meyrath, T. Zentgraf, N. Liu, L. W. Fu, H. Schweizer, and H. Giessen, "Optical resonances of bowtie slot antennas and their geometry and material dependence," *Optics Express,* vol. 16, pp. 7756-7766, May 26 2008.

[207] F. J. Garcia-Vidal, E. Moreno, J. A. Porto, and L. Martin-Moreno, "Transmission of light through a single rectangular hole," *Physical Review Letters,* vol. 95, p. 103901, Sep 2 2005.

[208] R. D. Kekatpure, E. S. Barnard, W. S. Cai, and M. L. Brongersma, "Phase-coupled plasmon-induced transparency," *Physical Review Letters,* vol. 104, p. 243902, Jun 17 2010.

[209] Z. F. Yu, G. Veronis, S. H. Fan, and M. L. Brongersma, "Gain-induced switching in metal-dielectric-metal plasmonic waveguides," *Applied Physics Letters,* vol. 92, p. 041117, Jan 28 2008.

[210] X. L. Shi and L. Hesselink, "Design of a C aperture to achieve lambda/10 resolution and resonant transmission," *Journal of the Optical Society of America B-Optical Physics,* vol. 21, pp. 1305-1317, Jul 2004.

[211] D. K. Gramotnev and S. I. Bozhevolnyi, "Plasmonics beyond the diffraction limit," *Nature Photonics,* vol. 4, pp. 83-91, Feb 2010.

[212] K. R. Li, M. I. Stockman, and D. J. Bergman, "Self-similar chain of metal nanospheres as an efficient nanolens," *Physical Review Letters,* vol. 91, p. 227402, Nov 28 2003.

[213] S. R. Ovshinsky, "Reversible electrical switching phenomena in disordered structures," *Physical Review Letters,* vol. 21, pp. 1450-1453, 1968.

[214] D. Lencer, M. Salinga, and M. Wuttig, "Design Rules for Phase-Change Materials in Data Storage Applications," *Advanced Materials,* vol. 23, pp. 2030-2058, May 10 2011.

[215] D. Hewak and B. Gholipour, "Primed to Remember," *Science,* vol. 336, pp. 1515-1516, Jun 22 2012.

List of Publications

Journal articles:

1. **M. Ding**, M. N. Zervas, and G. Brambilla, "Transverse excitation of plasmonic slot nano-resonators embedded in metal-coated microfiber tips," *Appl. Phys. Lett.* **102**, 141110 (2013).

2. **M. Ding**, G. Brambilla, and M. N. Zervas, "Plasmonic slot nano-resonators embedded in metal-coated plasmonic microfibres," was submitted to *J. Lightwave. Technol.*.

3. P. Wang*, **M. Ding***, T. Lee*, G. Senthil Murugan*, L. Bo, Y. Semenova, Q. Wu, D. Hewak, G. Brambilla, and G. Farrell, "Packaged chalcogenide microsphere resonator with high Q-factor," *Appl. Phys. Lett.* 102, 131110 (2013). (*contributed equally)

4. **M. Ding**, O. Fenwick, F. Di Stasio, J.-Y. Ou, N. Sessions, Y. Jung, F. Cacialli, and G. Brambilla, "Efficient light confinement with nanostructured optical microfibre tips," *Opt. Commun.* 285, 4688-4697 (2012).

5. **M. Ding**, P. Wang, and G. Brambilla, "Fast-response high-temperature microfibre coupler Tip thermometer," *IEEE Photonics Tech. Lett.* 24, 1209-1211 (2012).

6. **M. Ding**, P. Wang, and G. Brambilla, "A microfibre coupler tip thermometer," *Opt. Express* 20, 5402-5408 (2012).

7. **M. Ding**, G. S. Murugan, G. Brambilla, and M. N. Zervas, "Whispering gallery mode selection in optical bottle microresonators," *Appl. Phys. Lett.* 100, 081108 (2012).

8. **M. Ding**, M. N. Zervas, and G. Brambilla, "A compact broadband microfibre Bragg grating," *Opt. Express* 19, 15621-15626 (2011).

9. **M. Ding**, P. Wang, T. Lee, and G. Brambilla, "A microfibre cavity with minimal-volume confinement," *Appl. Phys. Lett.* 99, 051105 (2011).

10. **M. Ding**, M. Belal, G. Chen, R. Ismaeel, T. Lee, Y. Jung, P.i Wang, X. Zhang, Z. Song, F. Xu, R. Lorenzi, T. Newson, and G. Brambilla, "Optical microfibre passive devices and sensors," *Proc. SPIE* 8307, 83070Y (2011).

11. G. Y. Chen, **M. Ding**, T. P. Newson and G. Brambilla, "A review of microfibre and nanofiber based optical sensors," has been accepted by *the Open Optics Journal*

12. P. Wang, G. Brambilla, **M. Ding**, T. Lee, L. Bo, Y. Semenova, Q. Wu, G.

Farell, "Enhanced refractometer based on periodically tapered small core singlemode fiber," *IEEE Sensors J.* 13, 180-185 (2013)

13. P. Wang, **M. Ding**, L. Bo, Y. Semenova, Q. Wu, G. Farrell, "A silica single-mode fibre-chalcogenide multimode fibre-silica singlemode fibre structure," *Photonics Lett. of Poland* 4, 143-145, (2012).

14. C. Grivas, C. Li, P. Andreakou, P. Wang, **M. Ding**, G. Brambilla, L. Manna, and P. Lagoudakis, "Single-mode, single-exciton, tunable laser emission from colloidal nanocrystals," was submitted to *Nat. Commun.*.

15. R. M. N. Ismaeel, T. Lee, **M. Ding**, N. G. R. Broderick, G. Brambilla, "Nonlinear microfibre loop resonators for resonantly enhanced third harmonic generation," *Opt. Lett.* 37, 5121-5123 (2012)

16. R. Ismaeel, T. Lee, **M. Ding**, M. Belal, and G. Brambilla, "Optical microfibre passive components", *Laser & Photonics. Rev.* 2012 Wiley Online Library

17. J. L .Kou, **M. Ding**, J. Feng, Y.-Q. Lu, F. Xu, and G. Brambilla, "Microfibre-based Bragg gratings for sensing applications: a review," *Sensors **2012*** **12**, 8861-8876 (2012).

18. P. Wang, G. S. Murugan, T. Lee, **M. Ding**, G. Brambilla, Y. Semenova, Q. Wu, F. Koizumi, and G. Farrell, "High-Q bismuth silicate nonlinear glass microsphere resonators," *IEEE Photonics J.*4, 1013-1020 (2012).

19. P. Wang, G .S. Murugan, G. Brambilla, **M. Ding**, Y. Semenova, Q. Wu, and G. Farrell, "Chalcogenide microsphere fabricated from fiber tapers using contact with a high temperature ceramic surface," *IEEE Photonics. Tech. Lett.* 24, 1103-1105 (2012).

20. T. Lee, Y. Jung, C. A. Codemard, **M. Ding**, N. G. R. Broderick, and G. Brambilla, "Broadband third harmonic generation in tapered silica fibres," *Opt. Express* 20, 8503-8511 (2012).

21. P. Wang, T. Lee, **M. Ding**, A. Dhar, T. Hawkins, P. Foy, Y. Semenova, Q. Wu, J. Sahu, G. Farrell, J. Ballato, and G. Brambilla, "Germanium microsphere high-Q resonator," *Opt. Lett.* 37, 728-730 (2012).

22. P. Wang, G. Brambilla, **M. Ding**, Y. Semenova, Q. Wu, and G. Farrell, "The use of a fiber comb filter fabricated by a CO_2 laser irradiation to improve the resolution of a ratiometric wavelength measurement system," *J. Lightwave. Technol.* 30, 1143-1149 (2012).

23. P. Wang, **M. Ding**, G. Brambilla, Y. Semenova, Q. Wu, and G. Farrell, "High temperature performance of an optical microfibre coupler and its potential use as a sensor," *Electron. Lett.* 48, 283-284 (2012).

24. J. Feng, **M. Ding**, J.-L. Kou, F. Xu, and Y. Q. Lu, "An optical fiber tip micrograting thermometer," *IEEE Photonics J.* 3, 810-814 (2011).

25. P. Wang, G. Brambilla, **M. Ding**, Y. Semenova, Q. Wu, and G. Farrell, "High-sensitivity, evanescent field refractometric sensor based on a tapered, multimode fiber interference," *Opt. Lett.* 36, 2233-2235 (2011).

26. P. Wang, G. Brambilla, **M. Ding**, Y. Semenova, Q. Wu, and G. Farrell, "Investigation of single-mode-multimode-single-mode and single-mode-tapered-multimode-single-mode fiber structures and their applications for refractive index sensing," *JOSA B* 28, 1180-1186 (2011).

27. Y. Wang, D. J. Richardson, G. Brambilla, X. Feng, M. N. Petrovich, **M. Ding**, and Z. Song, "Intensity-measurement bend sensors based on periodically-tapered soft glass fibers," *Opt. Lett.* 36, 558-560 (2011).

Conferences:

1. **M. Ding**, M. N. Zervas, and G. Brambilla, "Transverse excitation of plasmonic slot nano-resonators embedded in gold-coated microfiber tips," *CLEO Europe*, Munich, 12-16 May 2013

2. **M. Ding**, G. Brambilla, and M. N. Zervas, "Plasmonic slot nano-resonators in gold-coated microfibers," *CLEO Europe*, Munich, 12-16 May 2013.

3. **M. Ding**, P. Wang, and G. Brambilla, "A fast response microfibre tip high temperature sensor," *22st International Conference on Optical Fiber Sensors (OFS 22)*, Beijing, 15-19 Oct 2012.

4. **M. Ding**, P. Wang, and G. Brambilla, "A compact temperature sensor based on micrometric optical fiber coupler tip," *Optical Sensors,* Monterey CA, 25 June 2012.

5. **M. Ding**, P. Wang, and G. Brambilla, "A high-T high-Resolution thermometer based on a microfibre coupler tip," *CLEO/QELS 2012,* San Jose, 6-11 May 2012.

6. **M. Ding**, G. S. Murugan, G .Brambilla, J. S. Wilkinson, and M. N. Zervas, "Robust mode-selection in optical bottle microresonators," *CLEO/QELS 2012,* San Jose, 6-11 May 2012.

7. **M. Ding** and G. Brambilla, "Optical fibre nanowire sensors and applications," *NanoSciTech 2012*, Chandigarh, 15-18 Feb 2012 (**Invited**).

8. **M. Ding** and G. Brambilla, "Nanostructuring of glass micro-nanowires," *IUPAC 7th Int Conf on Novem Materials and Synthesis (NMS-VII) & (FCFP-XXI)*, Shanghai, 16-21 Oct 2011 (**Invited**).

9. **M. Ding**, P. Wang, T. Lee, and G. Brambilla, "Focused ion beam engraved phase-shifted Bragg grating microcavity resonator," *Conference MediNano4*, Rome, 24-25 Oct 2011 (**Invited**).

10. **M. Ding** and G. Brambilla, "Nanostructured optical fibre tapers,"

Conference MediNano4, Rome, 24-25 Oct 2011 (**Postdeadline**).

11. **M. Ding**, F. Renna, and G. Brambilla, "Sub-wavelength light confinement in optical fibres and tapers using surface plasmons," *Photon 10*, Southampton, 23-26 Aug 2010. (**Best paper award**)

12. **M. Ding**, J. Y. Ou, N. P. Sessions, Y. Jung, and G. Brambilla, "Efficient light confinement to λ/10 spot sizes in optical fibre," *10th International Conference on Optical Communications and Networks (ICOCN)*, Nanjing, 24-27 Oct 2010.

13. **M. Ding**, F. Renna, and G. Brambilla, "Efficient light confinement in optical fibre tapers using plasmonics," *Plasmonics UK IoP*, London, 10 May 2010.

14. J.-C. Tinguely, P. Brox, B. S. Ahluwalia, **M. Ding**, G. Brambilla, A. Hohenau, J. R. Krenn, O. G. Hellesø, "Nanostructured glass fibres for optical trapping of nanoparticles" *2nd EOS Conference on Optofluidics*, Munich, 13-15 May 2013.

15. M. N. M. Nasir, **M. Ding**, G. S. Murugan, and M. N. Zervas, "Microtaper fiber excitation effects in bottle microresonators," *Photonic west*, San Francisco, 2-7 Feb 2013.

16. G. S. Murugan, M. N. M. Nasir, **M. Ding**, M. N. Petrovich, J. S. Wilkinson, M. N. Zervas, "Resonance spectroscopy of novel bottle microresonators and their applications in sensing," *Indo-US International Workshop on Spectroscopy: Application to National Security*, Varanasi, 18-20 Jan 2013 (**Invited**).

17. P. Wang, G. Brambilla, **M. Ding**, L. Bo, Y. Semenova, Q. Wu, and G. Farrell, "Refractive index sensing measurement based on periodically tapered small core singlemode fibre," *22st International Conference on Optical Fiber Sensors (OFS 22)*, Beijing, 15-19 Oct 2012.

18. G. Brambilla, **M. Ding**, J. -Y. Ou, N. Sessions, Y. Jung, O. Fenwick, F. Di Stasio, F. Cacialli, J. -L. Kou, F. Xu, "Sub-wavelength focusing of high intensities in microfibre tips," *ICP 2012*, Penang, 1-3 Oct 2012.

19. C. Grivas, P. Andreakou, P. Wang, **M. Ding**, G. Brambilla, L. Manna, P. G. Lagoudakis, "Single-mode tuneable laser operation of hybrid microcavities based on CdSe/CdS core/shell colloidal nanorods on silica microspheres," *EPS-QEOD Europhoton*, Stockholm 26-31 Aug 2012.

20. T. Lee, Y .Jung, C. A. Codemard, **M. Ding**, N. G. R. Broderick, and G. Brambilla, "Silica microfibres for broadband third harmonic generation," *CLEO/QELS 2012*, San Jose, 6-11 May 2012.

21. C. Grivas, P. Andreakou, P. Wang, **M. Ding**, G. Brambilla, L. Manna, and P. G. Lagoudakis, "Hybrid lasers based on CdSe/CdS core/shell colloidal quantum rods on silica microspheres," *CLEO/QELS 2012,* San Jose 6-11 May

2012.

22. P. Wang, **M. Ding**, G. Brambilla, Y. Semenova, G. Wu, and G. Farrell, "Resolution improvement of a ratiometric wavelength measurement system by using an optical microfibre coupler," *SOPO 12,* Shanghai, 21-23 May 2012.

23. C. Grivas, P. Andreakou, P. Wang, **M. Ding**, G. Brambilla, L. Manna, and P. G. Lagoudakis "Single-Mode Laser Operation of CdSe/CdS Core/Shell Colloidal Quantum Rods on Silica Microspheres," *E-MRS 2012 Spring Meeting*, 14-18 May 2012.

24. P. Wang, G. Brambilla, **M. Ding**, Y. Semenova, Q. Wu, and G. Farrell, "An SMS fiber structure based on a chalcogenide multimode fiber," *SPIE Photonics Europe,* Brussels, 16-19 April 2012.

25. P. Wang, G. Brambilla, **M. Ding**, Y. Wang, Y. Semenova, Q. Wu, L. Bo, and G. Farrell, "An improved ratiometric wavelength measurement system incorporating fibre comb filters fabricated by CO2 laser irradiation," *21st International Conference on Optical Fiber Sensors (OFS 21)*, Ottawa, 15-19 May 2011.

26. Y. Wang, D. J. Richardson, G. Brambilla, X. Feng, M. N. Petrovich, **M. Ding**, and Z. Song, "Bend sensors based on periodically-tapered soft glass fibers," *21st International Conference on Optical Fiber Sensors (OFS 21)*, Ottawa, 15-19 May 2011.